ABSTRACT

MACNAMARA, MARKUS RUDI. Groundwater ^{14}C Age and Tracer-Based Transit Time Distributions in the High Plains Aquifer, Nebraska. (Under the direction of Dr. David P. Genereux)

This study estimates the $^{14}C_{DIC}$ age of groundwater samples discharging from the High Plains Aquifer into the Middle Loup River and a large tributary, in the Nebraska Sand Hills. Groundwater samples were collected from beneath the riverbed at 16 cross-channel transects in 5 sampling areas located 6, 13, 20, 40 and 99 km downstream of a point near the center of Gudmundsen Sand Hills Laboratory. All samples were analyzed for temperature, pH, specific conductance, dissolved inorganic carbon (DIC), $\delta^{13}C_{DIC}$, and $^{14}C_{DIC}$, and a subset were also analyzed for major ions. These data were used as input in an ensemble of geochemical/isotopic models for estimating groundwater $^{14}C_{DIC}$ age. Models were constrained using published C isotope values for carbonate and soil organic matter in the Nebraska Sand Hills and the greater High Plains. Each groundwater age was weighted by the rate of groundwater seepage through the streambed, which was measured at each groundwater sampling point at the time of groundwater sampling, by collaborators at the University of Utah. These flow-weighted groundwater ages were used to construct a best estimate of the cumulative groundwater transit time distribution (TTD) for the samples.

Results indicate that groundwater discharge ranged in age from 0 – 8,200 yr. Approximately 80% of groundwater discharging from the aquifer was old enough to date using $^{14}C_{DIC}$, while about 20% was too young for this method. There is a strong west to east trend of increasing groundwater age across the study area, indicating that downstream sampling areas receive water from relatively longer and/or deeper flowpaths than those upstream. Groundwater age and mean transit time (MTT) each increased as distance downstream increased. The age range of discharging groundwater at each sampling area also increased as distance downstream increased. While most samples collected from the 6, 13, and 20 km sampling areas were too young to be dated with $^{14}C_{DIC}$, those collected at 40 and 99 km were all sufficiently old to be dated using $^{14}C_{DIC}$. Samples from the 40 and 99 km sampling areas contributed 75% of total groundwater discharge, all of which were greater than 600 yr old. The lack of young groundwater samples from the 40 and 99 km sampling areas might be explained by shorter groundwater flowpaths near these sites terminating in the gullies and near streambank areas that flank the main channel of the river. Flow weighted MTT values at the 40 and 99 km sampling areas were 1,944 yr and 5,029 yr, respectively. The MTT for all samples across the basin that could be dated using $^{14}C_{DIC}$ was 4,494 yr. Particularly at distances further downstream, younger groundwater discharges closer to the banks of the river, while the oldest samples discharge closer to the center of the channel. The distribution of ages across the channel may be influenced by stream sinuosity.

The shape of the observed TTD, inclusive of all samples collected from below the streambed, is approximately exponential, which suggests that generalized lumped parameter models (such as the exponential model) may be suitable for modeling TTDs in large unconfined aquifers like the High Plains Aquifer. This study demonstrates that the TTD of a large aquifer can be reconstructed using field-based multi-isotope groundwater sampling at the point of discharge in a streambed or riverbed. This study also demonstrates the importance of including tracers capable of dating groundwater up to tens of thousands of years old in field studies characterizing groundwater transit time distributions for aquifers.

Groundwater ^{14}C Age and Tracer-Based Transit Time Distributions in the High Plains Aquifer, Nebraska.

by
Markus Rudi MacNamara

A thesis submitted to the Graduate Faculty of
North Carolina State University
in partial fulfillment of the requirements for the degree of
Master of Science

Marine, Earth, and Atmospheric Sciences

Raleigh, North Carolina

2022

APPROVED BY:

_____	_____
Dr. David Genereux Committee Chair	Dr. Troy Gilmore

_____
Dr. Karl Wegmann

DEDICATION

To my friends and family; and to my loving wife Emily. Thirty thousand words aren't enough to express your importance to me.

BIOGRAPHY

Markus MacNamara was born and raised in Carlisle Pennsylvania. He earned a B.S. in geology from Guilford College in May 2014.

ACKNOWLEDGMENT

I extend my sincere gratitude to Professor David Genereux for his mentorship, advice, and commitment to excellence in scholarship. I thank Professor Troy Gilmore for his expertise in the hydrogeology of the Nebraska Sand Hills, and for his willingness to share information and generate intellectual discussion among our collaborators. I also thank Professor Karl Wegmann for his careful review, and for his insights regarding intersections of hydrogeology and geomorphology. I thank our collaborators, D. Kip Solomon, Aaron Mittelstet, Vitaly Zlotnik, Caner Zeyrek, Eric Humphrey, and Craig Jensen for their technical and intellectual support, as well as for their patience. Financial support for this project came from the National Science Foundation.

TABLE OF CONTENTS

LIST OF TABLES ix
LIST OF FIGURES x
1. Introduction 1
2. Study Site 2
2.1. Overview 2
2.2. Hydrologic/Hydrogeologic Setting 4
2.3. Field Site and Study Rivers 5
2.4. Carbon Isotopic Signatures of Subsurface Carbon Sources 8
3. Sampling Design 14
4. Methods 16
4.1. Analytical Methods 16
4.2.Estimation of Groundwater Age 16
4.2.1. Overview 16
4.2.2. Single Sample Models 17
4.2.3. NETPATH 21
4.3. Estimating the Groundwater Transit Time Distribution 22
5. Results 22
5.1. Water Chemistry: Streambed, Well, and Surface Water Samples 22
5.2. Tritium 28
5.3. Carbon isotopes: $^{14}C_{DIC}$ and δ^{13}_{DIC} 32
5.3.1 Overview 32
5.3.2. C isotope regressions 35
5.4. Groundwater Age Results 37
5.4.1. Determining reasonable $^{14}C_{REF}$ values 37
5.4.2. NETPATH Modeling Results 40
5.4.3. Groundwater Age Results 44
5.4.4. Flow Weighted Mean Transit Times and Groundwater Transit Time Distributions 47
6. Discussion 52
6.1. Uncertainty in Groundwater Ages 52
6.2. Spatial distribution of the age of groundwater storage and discharge 56
6.2.1. Longitudinal Distribution of Age for Groundwater Discharging Through the Riverbed 56
6.2.1. Groundwater flowpath length and potential recharge zones 58

6.2.3 Vertical gradients in age and $^{14}C_{DIC}$ 61
6.2.4. Variation of Groundwater Age and Seepage Across Sampling Transects..... 63
7. Conclusions 65
Works Cited..... 67

LIST OF TABLES

Table 1. Summary of $\delta^{13}C$ values measured in SOM and carbonates throughout the Great Plains. 13

Table 2. Summary statistics for $\delta^{13}C$ values. All $\delta^{13}C$ values of SOM come from samples collected in Nebraska (NE) 14

Table 3. Riverbed groundwater sampling summary. Transect ID is the distance downstream from the zero point 14

Table 4. Groundwater monitoring wells sampled for C isotopes and major ions. 15

Table 5. Description of variables used in the single sample models and NETPATH 19

Table 6. Physical and chemical data for streambed groundwater samples analyzed for major ions from the 6, 13, and 20 km sampling areas 24

Table 7. Physical and chemical data for streambed groundwater samples analyzed for major ions from the 40 and 99 km sampling areas 25

Table 8. Physical and chemical data for groundwater sampled from wells and analyzed for major ions. 25

Table 9. Physical and chemical data for surface water samples 26

Table 10. Average contribution of dissolved ions to groundwater charge balance 27

Table 11. C isotope and ^{3}H data for groundwater samples collected from below the riverbed at the 6, 13, and 20 km sampling areas 30

Table 12. C isotope and ^{3}H data for groundwater samples collected from below the riverbed at the 40 and 99 km sampling areas 31

Table 13. C isotope data for groundwater samples collected from wells across the study area. 34

Table 14. C isotope and ^{3}H data for surface water samples collected in the study stream 34

Table 15. C isotope values of DIC sources used in groundwater age modeling. 35

Table 16. Minimum $^{14}C_{REF}$ value required to produce all positive ages at each transect 37

Table 17. The 39 modeling scenarios considered. 39

Table 18. Models not rejected using the criteria described in the text 39

Table 19. Phases and stoichiometric coefficients of elements as they are added to (positive) or removed from (negative) a solution through dissolution or precipitation of each phase respectively in NETPATH 41

Table 20. Mass balance calculations performed with NETPATH for all samples dated using $^{14}C_{DIC}$. 43

Table 21. Average unadjusted age and average modeled age for the 17 accepted modeling scenarios 44

Table 22. ^{14}C age results for riverbed groundwater samples from the 40 and 99 km sampling areas. 45

Table 23. ^{14}C age results for riverbed groundwater samples thought to be older than 75 yr, based on $^{3}H/^{3}He$ age dating, from the 6, 13, and 20 km sampling areas. 46

Table 24. Estimated age (yr) of NETPATH "initial water" 47

Table 25. Groundwater seepage rate, average age, and standard deviation (SD) in age for samples dated using $^{14}C_{DIC}$. 48

Table 26. Mean transit times, seepage fractions, and geodesic distance east of the study zero point 56

Table 27. Well depth, elevation, and age data for groundwater samples from wells in this study. 61

LIST OF FIGURES

Figure 1. Location of the Nebraska Sand Hills and sampling areas associated with this study..... 3

Figure 2. Map of the study site including the zero point..... 4

Figure 3. Detail of sampling transect locations at the 6, 13, 20, 40, and 99 km sampling areas. 7

Figure 4. Sampling locations of studies reporting δ13C of SOM (green squares) or carbonate mineral solids (likely calcite, blue triangles) throughout Nebraska 11

Figure 5. Variation of $\delta^{13}C_{SOM}$ (left) and $\delta^{13}Cs$ (right) with depth as reported by sources listed in Table 1..... 12

Figure 6. Regression of calcium concentration vs. specific conductance in groundwater samples..... 21

Figure 7. Piper diagram of groundwater samples collected in May 2019, and August or September 2020 23

Figure 8. Ion balance for average streambed groundwater, well water, and surface water samples..... 27

Figure 9. Ca vs DIC concentration in groundwater samples collected below the streambed and from wells. 28

Figure 10. $^{14}C_{DIC}$ vs. $\delta^{13}C_{DIC}$ for groundwater samples collected below the riverbed..... 32

Figure 12. $^{14}C_{DIC}$ vs. SpC (top) and $^{14}C_{DIC}$ vs. DIC for groundwater and surface water (SW) samples. 6 surface water samples were analyzed for both SpC and $^{14}C_{DIC}$, while 22 were analyzed for both $^{14}C_{DIC}$ and [DIC]. 38

Figure 13. Cumulative TTDs for the 40 km (top), 99 km (center), and combined sampling areas. 49

Figure 14. Selected cumulative TTDs resulting from modeling scenarios..... 50

Figure 15. Cumulative TTD for all riverbed groundwater samples..... 51

Figure 16. Exponential and gamma distributions fit to the TTDs based on average 14C ages 51

Figure 17. The effect on groundwater age of varying the estimate of the C isotopic composition of a C source..... 54

Figure 18. Change in average age for the 40 km and 99 km groundwater samples (n = 41) between successive simulations in experiments 1, 2, and..... 55

Figure 19. Variation in MTT with distance downstream 57

Figure 20. Variation in average q with distance downstream..... 57

Figure 21. Potential recharge areas for samples collected at the 40 and 99 km sampling areas. 60

Figure 22. Groundwater age and depth for well samples from the study 62

Figure 23. Estimated depth of penetration below the water table for groundwater samples from the 40 and 99 km sampling areas..... 63

Figure 24. Variation in age of groundwater across riverbed transects 64

Figure 25. Effects of stream channel sinuosity on the geometry of the groundwater flow lines in a vertical cross-section beneath a uniformly sinuous gaining stream..... 65

1. Introduction

Determining the age of groundwater in an aquifer provides critical information about the movement of water through the subsurface. This information in turn can enable informed decisions regarding the preservation and sustainable use of critical groundwater resources (Clark and Fritz 1997; Kalin 2000). In addition to groundwater that recharged relatively recently, aquifers that are large enough to provide economically significant quantities of water usually contain groundwater that recharged hundreds to tens of thousands of years ago (Fontes 1992, Han and Plummer 2016, Cartwright et al. 2020). Since the 1960s the radiocarbon (^{14}C) signal of the dissolved inorganic carbon (DIC) in groundwater ($^{14}C_{DIC}$) has been used to determine the ages of groundwater samples (e.g., Ingerson and Pearson 1964; Pearson 1965; Tamers 1967; Gallagher 2000; Kennedy and Genereux 2007; Cartwright 2009; McCallum et al. 2018). The ubiquity of DIC in water, along with the availability of high-quality ^{14}C and stable carbon isotope ($\delta^{13}C$) analysis has led to $^{14}C_{DIC}$ dating becoming one of the most commonly used methods in hydrogeology (Fontes 1992, Han and Plummer 2016, Cartwright 2020).

One complication in $^{14}C_{DIC}$ age dating of groundwater is that groundwater DIC is a mixture of C from sources with different C isotopic compositions. In the decades since the development of the earliest $^{14}C_{DIC}$ age dating methods, a variety of models aimed at disentangling the contribution of the many C sources to DIC have been developed. In this study I use several of these models, in tandem with geochemical and isotopic analysis, to determine the ages of groundwater samples collected from the High Plains Aquifer at a study site in the Nebraska Sand Hills.

Groundwater samples used in $^{14}C_{DIC}$ age dating studies are traditionally collected from wells distributed across a study area at a variety of depths and locations. While some samples from this study were collected in this way (n=13), the majority (n=100) were collected from below the streambed using a steel sampling probe. This sampling approach exploits the discharge characteristic of gaining streams, specifically, that each point on the stream represents a point of discharge (the end of a flowline) for groundwater exiting the aquifer through the streambed. A consequence of this feature of gaining streams is that the age of a sample collected just before exiting the aquifer through the streambed is equivalent to the travel time of the sample along its flowpath through the aquifer from recharge to discharge (i.e., its transit time).

This method circumvents the economic barriers associated with the installation of monitoring wells, and when paired with measurements of groundwater seepage flux (specific discharge) through the streambed it allows for direct estimation of the groundwater transit time distribution (TTD) of the aquifer (Kennedy et al. 2009; Gilmore et al. 2016). The TTD contains information regarding the storage, transport pathways, and age of water within an aquifer. The TTD can be used to predict the rates at which contaminants are flushed through a groundwater system and the timescale and magnitude of surface water's susceptibility to contamination by groundwater-delivered contaminants (McGuire and McDonnell 2006).

Previous studies that coupled streambed groundwater sampling with seepage flux measurement (Browne and Guldan 2005; Kennedy et al. 2009; Gilmore et al. 2016) did not use a tracer like ^{14}C capable of determining the age of old groundwater. The goal of this study was to use $^{14}C_{DIC}$ to test for the presence of old groundwater discharging into the Middle Loup River in western Nebraska, and where possible calculate the ^{14}C age of the old groundwater. Age results were used with seepage flux data from collaborators at the University of Utah to estimate the groundwater TTD for a catchment of approximately 5,400 km^2.

2. Study Site

2.1. Overview

The Nebraska Sand Hills are a grass-stabilized aeolian dune field covering approximately 50,000 km^2 of central and western Nebraska, as well as parts of Kansas and South Dakota (Figure 1) (Mason et al. 2020). Primarily composed of quartz sand, with lesser amounts of plagioclase and potassium feldspar (Muhs 2017), these Quaternary dunes can rise to more than 100 m above the local valleys (though most reach a height of about 50 m) and are oriented generally east to west across the central Sand Hills (Mason et al. 2020), which is the area of focus for this research.

Though the dunes are currently stabilized by perennial grasses, periods of instability and dune migration haver occurred the past 15 thousand years have seen periods of dune instability and migration, most associated with periods of intense drought (Stokes and Swinehart 1997; Loope and Swinehart 2000; Nicholson and Swinehart 2005; Mason et al. 2011; Mason et al. 2020). Paleoclimate studies have identified periods of dune stability or migration in the Sand Hills, using radiocarbon dating of soil organic matter (SOM) preserved in paleosols, and optically stimulated luminescence (OSL) dating of sand deposits above and below paleosols (Goble et al. 2004; Miao et al. 2007a; Miao et al. 2007b). Often these techniques are used in tandem to better constrain periods of migration and stability.

Other studies document shifts in climate and the composition of plant communities using analysis of stable C isotopes in paleosols and pedogenic carbonates (Fox and Koch 2003; Fox and Koch 2004; Tecsa et al. 2020; Layzell and Mandel 2020). Swinehart and Diffendal (1989) report one uncalibrated radiocarbon age of 13,160 ± 450 ^{14}C yr BP from a peat deposit underlying 46.3 m of dune sands at the eastern boundary of an interdunal wetland at Gudmundsen Sandhills Laboratory (GSL), indicating some Quaternary dune migration at the study site. Stokes and Swinehart (1997) noted the presence of horizontally laminated “carbonaceous and diatomaceous silts and sands” in the unsaturated zone in a cutbank of the South Branch Middle Loup River between the 13 and 20 km sampling areas (Figure 2). Stokes and Swinehart (1997) interpret these deposits, which underlay several paleosols, to be fluvio-lacustrine in nature. They note that “root penetration and post-depositional disturbance is pervasive throughout the limited exposures of fluvio-lacustrine sediments (p. 264).” Radiocarbon dating on organic matter from both the laminated sediments themselves and overlaying paleosols yield ages ranging from 9,610 ± 80 (fluvio-lacustrine sediments) to 270 ± 70 ^{14}C yr BP (youngest paleosol). The ages of the above mentioned paleosols and deposits suggest that in the intervening time between the deposition of the fluvio-lacustrine sediments and the present, there have been at least three episodes of dune mobilization at this site and that bed of the river likely incised from the elevation of the exposed deposits (about 1.5 m above the current channel) to its current elevation.

The current climate in the Sand Hills is semi-arid. The region experiences hot summers, and cold winters typical of the North American mid-continent (Hobza and Schepers 2018). Average annual temperature is about 9^{o}C (McMahon et al. 2007). Between 1939 and 2005 precipitation averaged 43.18 cm/yr in the western Sand Hills, increasing to 68.58 cm/yr in the eastern Sand Hills (Hobza et al. 2012). Most precipitation falls during the late spring and summer months when seasonal southeasterly winds transport moisture rich air from the Gulf of Mexico into the central and northern Great Plains (Mason et al. 2020; McMahon et al. 2007). Evapotranspiration is also greatest during this time. As a result, the majority of recharge into the aquifer occurs during winter months when primary productivity is at its lowest (Hobza and Schepers 2018). Average evapotranspiration in the Sand Hills ranges from 40 cm/yr in the west to 48.26 cm/yr in the east. Mean annual precipitation and groundwater recharge across the Sand Hills are 53.3 cm and 7.3 cm respectively (Szilagyi and Jozsa 2012).

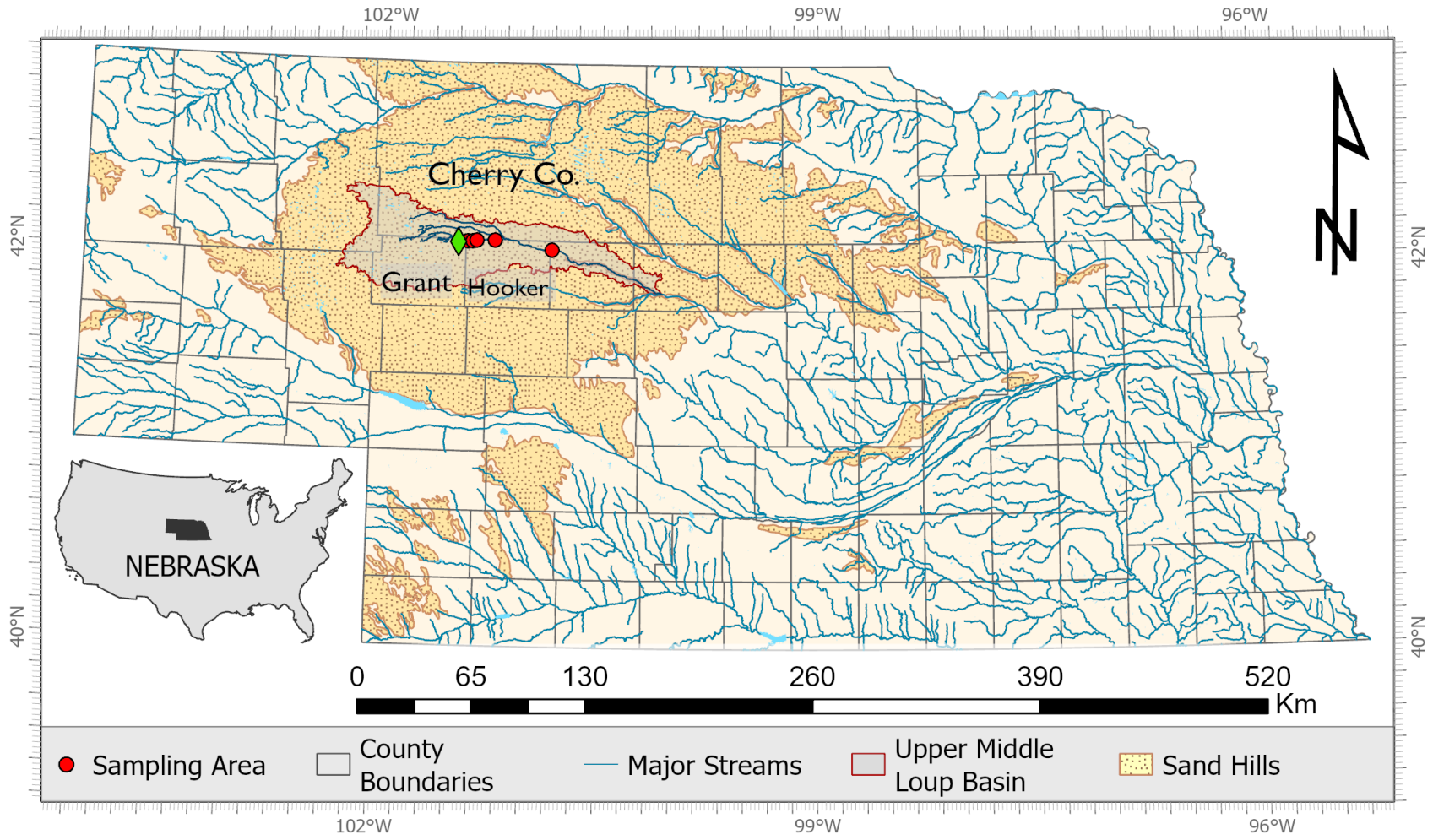

Figure 1. Location of the Nebraska Sand Hills and sampling areas associated with this study. Primary streams of Nebraska are shown in blue. Sampling areas are indicated by red circles. The Upper Middle Loup basin (HUC 10210001) is shown as grey area with red border. County boundaries are shown as grey lines and county names are shown in black text.

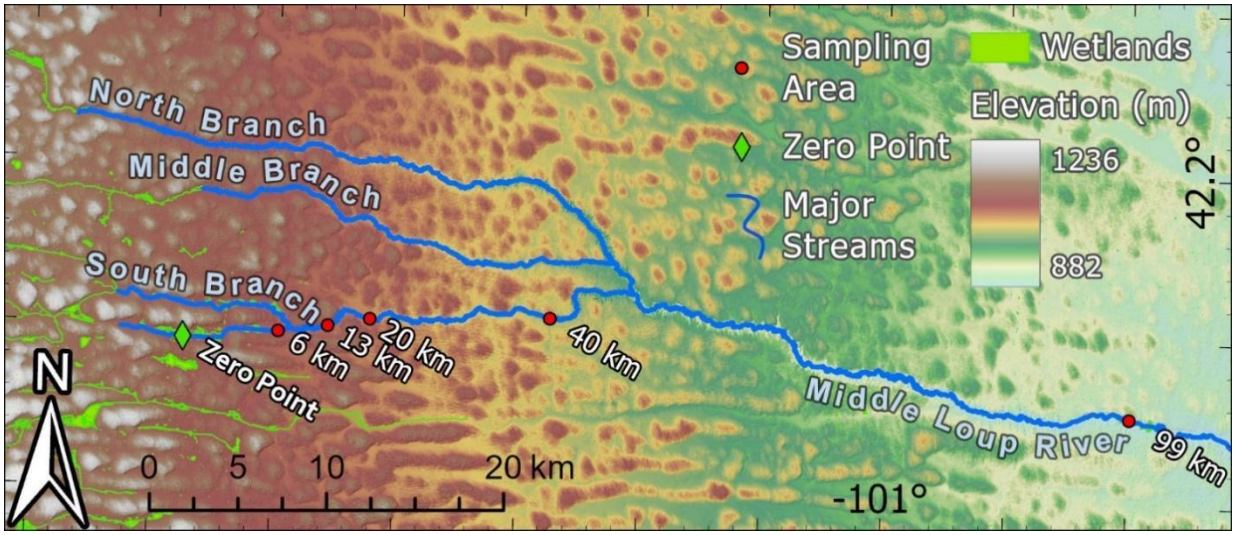

Figure 2. Map of the study site including the zero point (the starting point for measuring distances along the channel), sampling areas (named by their distances downstream of the zero point, as measured along the channel), wetlands, and rivers contributing to the Middle Loup River.

2.2. Hydrologic/Hydrogeologic Setting

The dunes of the Sand Hills comprise the uppermost unit of the High Plains Aquifer, the regional unconfined aquifer that is the principal source of irrigation water for cereal grain production and industrial agriculture in the Midwest United States (Hobza et al. 2012). The High Plains Aquifer extends from central Texas to South Dakota, covering 450,000 km^2 in total (Sophocleous 2010). In Nebraska, hydrostratigraphic units of the High Plains Aquifer include hydrologically connected Tertiary to Quaternary stratigraphic units. The thickest and most productive of these are the Miocene fluvial gravels and sands of the Ogallala Group, which reach a thickness of 240 m in the western Sand Hills (Hobza et al., 2012). Spatially discontinuous Pliocene to Pleistocene aged alluvial gravels known as the Broadwater and Long Pine Formations overlay the Ogallala unconformably in parts of the central and western sand hills. Quaternary aeolian sands and loess cap the HPA throughout central and western Nebraska (Hobza et al. 2012).

Typically 45 to 90 m in thickness (maximum thickness of 210 m), the Quaternary aeolian deposits (dunes) of the Sand Hills can produce up to 63 L/s of groundwater when agricultural irrigation wells in the unit are pumped (Hobza et al. 2012). The thickness of these sands, which cover the entire study area, ranges from 33.8 to 210 m. The thickness of the Pliocene/Pleistocene gravels ranges from 0 to 40 m, the thickest deposits occurring in northwestern Hooker County approximately 15 km south of the South Branch Middle Loup River. Thickness of the Ogallala Formation ranges from 140 to 270 m in the study area, and the top of the formation can be found at depths as shallow as 7.5 m directly north of the South Branch Middle Loup River in south central Cherry County (Hobza et al. 2012).

In the Sand Hills, dune surfaces generally act as recharge zones to the High Plains Aquifer, and wetlands, lakes, and rivers serve as groundwater discharge zones. The regional water table slopes from west to east (Gilmore et al. 2019). Baseflow-dominated rivers with gradients ranging from 0.0276 to 0.0910 flow west to east, mirroring the slope of the regional water table system (Gilmore et al. 2019). Groundwater not leaving the aquifer through discharge into rivers and lakes contributes to the replenishment of the High Plains Aquifer (McMahon et al. 2007). As such, the Sand Hills are a critical component of the water budget on which much of American agriculture depends. Understanding the

distribution of groundwater transit times in the High Plains Aquifer can provide insight on best management practices for groundwater resources in the Midwest United States.

The western Sand Hills exhibit a high spatial density of freshwater to alkaline lakes, most of which are hydrologically connected to the underlying aquifer and adjacent waterbodies (Winter 1986; Winter et al. 2003; Bennett et al. 2007). Seasonal changes in evapotranspiration and water table configuration drive fluctuations in these lakes, often leading to the precipitation of evaporite minerals (Gosselin et al. 1994; Gosselin 1997; Zlotnik et al. 2012). Deposits of gypsum ($CaSO_4 \cdot 2H_2O$), aphthitalite ($K_3Na(SO_4)_2$) , mirabilite ($Na_2SO_4 \cdot 10H_2O$), thernardite (Na_2SO_4), trona ($Na_3H(CO_3)_2 \cdot 2H_2O$), and thermonatrite ($Na_2CO_3 \cdot H_2O$) have been documented in the closed basins of the western Sand Hills (Gosselin et al. 1994; Jacobs et al. 2007; Zlotnik et al. 2012). When lake levels drop, these evaporites are subject to aeolian transport through deflation as particulate dust (Zlotnik et al. 2012). Zlotnik et al. (2012) estimated that a single lake/playa system in the western Sand Hills generates up to 120 $tons \cdot km^{-2} \cdot yr^{-1}$ of particulate evaporite dust. Strong northwesterly autumnal winds (Mason et al. 2020) may serve as a transport mechanism for deposition of these minerals across the Sand Hills.

In the central and western Sand Hills, interactions between dune morphology and water table depth have resulted in the development of stable localized groundwater flow systems. These systems tend to develop in valleys between barchan dune ridges where interdunal wetlands (referred to locally as "wet meadows") serve as discharge zones (Gosselin et al. 2006; Chen and Hu 2004). The topographic relief of the ridges drives infiltrating precipitation from dune crests downgradient into the subsurface below interdunes (Gosselin et al. 2006; Harvey et al. 2007). Interdunal wetlands receive groundwater discharge throughout the year and are often used for hay production and cattle grazing. A consequence of plant growth due to stable groundwater discharge is that interdunal wetlands accumulate peat and organic matter deposits (up to 7 m thick) and are thus large carbon pools. One interdunal wetland located in Cherry County, NE, approximately 35 km north of Gudmundsen Sandhills Laboratory (GSL) exhibited a nearly continuous 15,000 yr record of peat accumulation, suggesting the long-term stability of some of these groundwater discharge zones (Nicholson and Swinehart 2005).

2.3. Field Site and Study Rivers

Field work for this project was conducted on the Middle Loup River, the South Branch Middle Loup River (SBMLR), and an unnamed headwater tributary flowing into the SBMLR (Figure 2). An arbitrary zero point for the study river was established where the unnamed tributary crosses a road culvert on the ranch that served as our field base, Gudmundsen Sandhills Laboratory (GSL), a rangeland laboratory and working cattle ranch owned and operated by the University of Nebraska – Lincoln (UNL). Five main groundwater sampling areas were named by their distances downstream from the zero point, as measured along the river channel: 6 km, 13 km, 20 km, 40 km, and 99 km (Figures 2 and 3). Within each sampling area, groundwater samples were collected beneath the riverbed on transects across the channel.

Contributing groundwater flow areas upgradient of the sampling locations at 6 km and 99 km were about 13 and 3900 km^2, respectively. Groundwater flow areas were defined by collaborators at UNL using potentiometric head contours measured by the Conservation and Survey Division (CSD) of the University of Nebraska in 1995 (Summerside et al. 2001; personal communication, July 24, 2020, Caner Zeyrek).

The unnamed tributary begins as an agricultural ditch that drains the interdunal wetland at GSL. West to east trending barchan ridges border the wetland to the north and south, rising about 68 m above the meadow (Gosselin et al. 2006). The work of Gosselin et al. (1999), Gosselin et al. (2006), and Chen and Hu (2004) suggests that the interdunal wetland at GSL is a groundwater discharge area. Infiltration through the dune sands causes the water table to be higher beneath the dunes.

Downstream from the straightened and deepened ditch in the wet meadow at GSL, the unnamed tributary and SBMLR flow generally eastward through the Sand Hills; natural meanders begin about 5 km downstream of the zero point on the tributary. At the 6 km sampling area the river's floodplain occupies the width of the interdunal wetlands. Near channel relief (the maximum height of dune surfaces above the river within 500 m of the channel) is 35 m at the 6 km sample area. As downstream distance increases, near channel relief increases, and wetlands occupy a smaller area on either side of the channel. At the 13 km sampling area, near channel relief has a value of 60 m and the steepest dune faces exhibit eroded gullies. At the 20 km sampling area eroded gullies also exist and near channel relief is 32 m. Between the 20 and 40 km sampling areas entrenchment increases, and erosional gullies have higher frequency than upstream. At the 40 km sampling area near channel relief is 65 m. Between the 40 and 99 km sampling areas, near channel relief reaches a maximum value of 100 m. Downstream of the confluence of the North, Middle, and South Branches of the Middle Loup River, the floodplain widens. At the 99 km sampling area near the town of Seneca Nebraska, near channel relief is 80 m.

May (1992), May et al. (1995), May (2003), and May and Holen (2014) performed detailed studies of alluvial stratigraphy within the Loup River Basin. They interpreted stratigraphy and radiocarbon samples of floodplain SOM to document periods of incision and aggradation across the basin. Their findings indicate the rivers of the Loup River Basin responded to changes in climate and water availability throughout the Quaternary by aggrading or incising as the water budget fluctuated. Brice (1964), and Guhman and Pederson (1992), report channel incision/entrenchment on the North Loup and Dismal Rivers, and Chen et al. (2003) demonstrate that depth to the water table and hydraulic gradient of the groundwater increase significantly in the vicinity of the channel of the Middle Loup River compared to the area between the Middle Loup and adjacent rivers.

Hobza and Schepers (2018) report that the Middle Loup River receives more than 90% of streamflow through base flow. Most baseflow in this region is due to groundwater discharge. Groundwater discharge is primarily diffuse seepage through the riverbed and banks, though focused discharge at does occur in small springs and seeps in gullies that occur along the banks of rivers (Guhman and Pederson 1992; Hobza and Schepers 2018).

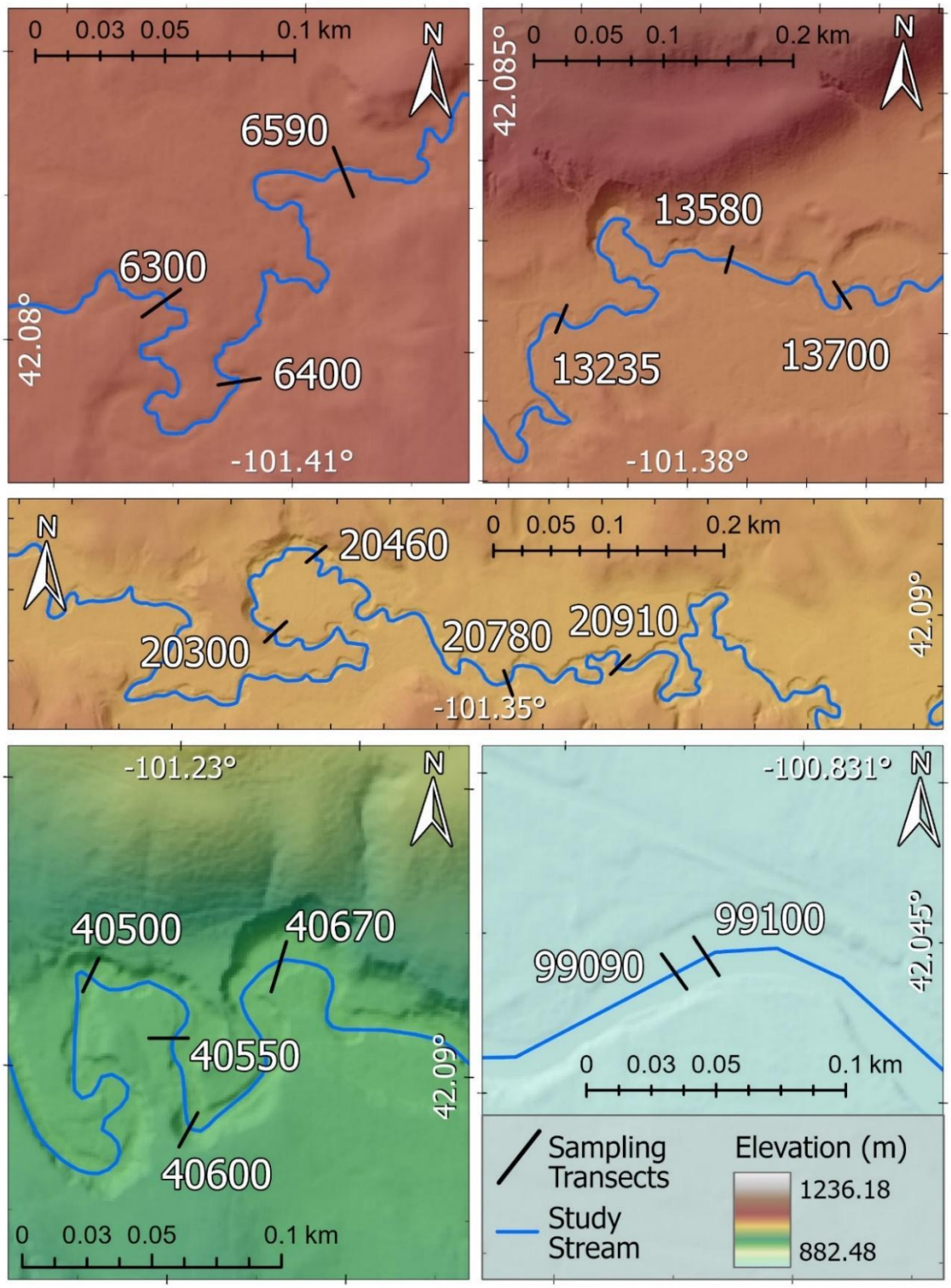

Figure 3. Detail of sampling transect locations at the 6, 13, 20, 40, and 99 km sampling areas. Each transect is named by its distance downstream (in meters) from the arbitrary zero point at Gudmundsen Research Laboratory, as measured along the channel.

2.4. Carbon Isotopic Signatures of Subsurface Carbon Sources

The three most abundant isotopes of carbon (C) in earth's environment are carbon-12 (^{12}C), a stable C isotope that comprises about 98.9% of all carbon on earth; carbon-13 (^{13}C), another stable C isotope, comprises almost all of the remaining 1.1% of C in the environment; and carbon-14 (^{14}C) a radioactive C isotope present in the earth's atmosphere at much lower levels than ^{12}C and ^{13}C (about 1 ^{14}C atom per 10^{12} stable C atoms) (Clark and Fritz 1997).

^{14}C is continually produced as solar cosmic radiation bombards the upper atmosphere, when slow neutron particles (secondary particles produced in the upper atmosphere as cosmic rays interact with other gasses) collide with ^{14}N. The slow neutron enters the ^{14}N nucleus, causing a proton to be ejected. The resulting element (^{14}C) is a carbon atom with 6 protons and 8 neutrons (^{14}C) (Clark and Fritz 1997). ^{14}C rapidly forms $^{14}CO_2$ ($^{14}C_g$) as it interacts with O_2 molecules in the atmosphere and integrates into the biosphere as it dissolves into oceans or is taken up by plants during photosynthesis (Clark and Fritz 1997).

Determining representative values for the isotopic signature of C sources can be more difficult in semiarid and arid climates than in aquifers where the primary mineral C source is ancient marine limestone (Cartwright 2020). Choosing incorrect values for these parameters can lead to the over- or underestimation of groundwater age depending on which models are applied to the samples (Cartwright 2020; Han and Wassenaar 2021). To determine representative values for the C isotope sources in the Sand Hills, I performed a survey of literature reporting C isotopic values for soil organic matter (SOM) and calcite, and used the data to help define the C isotopic values taken as input to the ^{14}C models that were used to estimate groundwater age.

Data from paleoclimate and landscape evolution studies indicate that the C isotopic signatures of carbon sources vary with location and depth in the Sand Hills and the surrounding loess plains (Tables 1 and 2, Figures 4 and 5). Understanding the carbon isotopes in subsurface carbon sources is essential to this study because these carbon pools represent the sources of groundwater DIC, and their isotopic compositions are inputs to the geochemical correction models used to estimate groundwater ^{14}C age. The effectiveness of the correction models rely in part on accurate input values of ^{14}C and $\delta^{13}C$ for these carbon pools.

DIC in groundwater has two primary contributing pools, 1) soil CO_2 and 2) carbonate minerals. Soil CO_2 primarily dissolves into groundwater in the unsaturated zone above the water table and is produced by plants during root respiration and by microbes that produce CO_2 through respiration as they consume the decaying plant material which makes up SOM (Davidson, 1995). In most aquifers the primary mineral source of carbon is calcite, though dissolution of dolomite and magnesian carbonates also produces DIC.

The $\delta^{13}C$ content of soil CO_2 depends on the isotopic composition of the current and historical plant community occupying an area, as well as the $\delta^{13}C$ of CO_2 in the atmosphere. As plants utilize atmospheric CO_2, they become depleted in ^{13}C due to fractionation during photosynthesis (Clark and Fritz 1997). The amount of ^{13}C fractionation depends on the photosynthetic pathway utilized by the plant. About 80% of terrestrial plant species utilize the Calvin (C3) photosynthetic pathway, which results in plant material with $\delta^{13}C$ values between -37 and -20‰, with an average value of about -27‰ (Cartwright et al. 2020; Clark and Fritz 1997). About 15% of plant species, primarily grasses growing in warm or semi-arid climates, utilize the Hatch Slack (C4) photosynthetic pathway, which results in plant material with $\delta^{13}C$ values between -16 and -10‰, with an average value of about -12.5‰ (Cartwright et al., 2020; Clark and Fritz, 1997). SOM in landscapes where both C3 and C4 plants are present has intermediate values of $\delta^{13}C$ dependent on the relative proportion of plants utilizing each mode of photosynthesis (Fox and Koch, 2007). While growing, plant roots exude CO_2 gas into the pore space of the soil. The CO_2 produced by roots makes up about 60% of the soil CO_2 in non-forested environments (Hanson et al. 2000). As plants die, some of their remains are incorporated into the soil and begin to

decompose as they are consumed aerobically by bacteria. This process is responsible for about 40% of the soil CO_2 in non-forested environments (Hanson et al. 2000).

The $\delta^{13}C$ of microbially respired CO_2 is essentially identical to that of SOM; fractionation between SOM and CO_2 is between -0.1 and +0.1‰ (Breecker et al. 2015). Similarly, soil respired CO_2 from plant roots shows very little fractionation between SOM and CO_2 (the review and experiment by Breecker et al. (2015) show a fractionation between SOM and CO_2 between -0.7 and +0.5‰ in undisturbed soil). Following Cerling et al. (1991), "soil respired CO_2" refers here to CO_2 moving upward across the ground surface. Soil respired CO_2 exhibits essentially no $\delta^{13}C$ fractionation relative to SOM, but the $\delta^{13}C$ of CO_2 in the soil is generally isotopically heavier than SOM and soil respired CO_2 (Cerling et al. 1991; Davidson 1995). This is due to the diffusive fractionation during the movement of CO_2 gas upward through the soil profile toward the soil/atmosphere boundary (Cerling et al. 1991). The diffusion coefficient for $^{13}CO_2$ in air is 4.4‰ (0.44%) smaller than that for $^{12}CO_2$ (Craig 1953; Jost 1960; Cerling et al. 1991), therefore the $\delta^{13}C$ in soil gas will be at least 4.4‰ greater than soil respired CO_2 (Cerling et al. 1989; Cerling et al., 1991; Davidson 1995). In other words, the $\delta^{13}C$ of the gaseous CO_2 contributing to DIC is at least 4.4‰ greater than the $\delta^{13}C$ of SOM from which it is produced; the difference might be even greater if the soil respiration rate is low (Cerling et al. 1991).

A distinction also exists in the $\delta^{13}C$ and ^{14}C content between carbonates formed in marine environments and those formed more recently in terrestrial environments. Marine limestones on land (on the continents) generally have $\delta^{13}C$ close to 0‰ and are old enough that ^{14}C = 0 pmc (Fontes, 1992). Carbonates forming in terrestrial environments are largely pedogenic, which commonly form in isotopic equilibrium with the soil atmosphere (Cerling et al. 1989; Cerling 1991; Davidson 1995) and therefore have greater $\delta^{13}C$ than marine limestone (Table 1) and non-zero ^{14}C at the time of deposition. Reports of distinct and laterally continuous carbonate layers in the dunes of the Nebraska Sand Hills are uncommon (Muhs and Budahn 2019), but pedogenic and groundwater carbonates are well documented in the Ogallala group (Diffendal 1982; Gardner et al. 1992; Fox and Koch 2003; McMahon et al. 2007) and diffuse pedogenic carbonates are documented in modern soils (Kelly et al. 1991) as well as paleosols (Tecsa et al. 2020) in the region. In UNL CSD testhole logs, calcite was documented relatively infrequently in the subsurface surrounding and within the study area. Only 6 of the 53 CSD testhole logs reviewed for this study had documentation of calcite occurring at depths shallower than 33 m below ground surface. Where present, carbonate minerals in the Sand Hills usually occur as diffuse evaporitic and pedogenic deposits in soils and paleosols (Kelly et al. 1991; Fox and Koch 2004; Tecsa et al. 2020).

In the Sand Hills, $\delta^{13}C$ values tend to decrease with increasing depth for both SOM (Steuter et al. 1990; Goble et al. 2004; Johnson and Willey 2000; May 2003; Mason et al. 2008) and pedogenic carbonates (Kelly et al. 1991; Fox and Koch 2003; Fox and Koch 2004; Layzell and Mandel 2020; Tecsa et al. 2020), a result of a change in plant species community composition throughout time (Figure 5). $\delta^{13}C$ values of SOM range from -25.0‰ in a paleosol dated at 9000 yr (Layzell and Mandel 2020) to -12.2‰ in a modern Sand Hills soil (Steuter et al. 1990). $\delta^{13}C$ values in pedogenic carbonates also become more depleted (lower) with depth. Shallow, modern pedogenic carbonates exhibit $\delta^{13}C$ values as high as +0.75‰ in southern NE (Kelly et al. 1991), while a carbonate sampled from a depth of 145 m below ground surface in the Sand Hills exhibited a value of -9.1‰ (McMahon et al. 2007).

Plant community composition is a function of many factors, including temperature, aridity, water availability, and historical species distribution. Thus, trends in $\delta^{13}C$ of SOM and pedogenic carbonates were not necessarily uniform across the Sand Hills at any time, nor are they with depth, as paleosols may be eroded or buried as geomorphic processes act on the surface.

Given the demonstrated lack of major carbonate deposits in the Sand Hills, it is likely that the primary source of mineral C to the DIC is the diffuse pedogenic carbonates deposited as a product of water use and transpiration by plants (Tecsa et al. 2020). Pedogenic carbonates form in isotopic equilibrium with soil CO_2 (Cerling et al. 1989; Cerling and Quade 1993). The age and $\delta^{13}C$ values of

pedogenic calcite can help in identifying reasonable values of $\delta^{13}C_s$ (the $\delta^{13}C$ of calcite) and $^{14}C_s$ (the ^{14}C of calcite) for use in the groundwater age models that use these values.

There are at least 51 published optically stimulated luminescence (OSL) and radiocarbon dates for sediments and paleosols collected less than 25 km north or south of the main channel of the Middle Loup River, many of which were within the primary watershed of this study. These samples show that the age of the current landscape and shallow subsurface ranges from 0 to 11,000 yr, with a median value of 897 yr (median sample depth of 3 m)(Swinehart 1989; Muhs et al. 1997, Stokes and Swinehart 1997; Goble et al. 2004; Mason et al. 2004; Miao et al. 2007; Schmeisser et al. 2015).

While the overall variability of $\delta^{13}C_s$ in the High Plains Aquifer is high, the variability and spread of $\delta^{13}C_s$ in the shallow subsurface is much lower. The 116 published $\delta^{13}C_s$ values from studies in and around the Sand Hills for samples from depths of 6 m or shallower had a median, range, and standard deviation of -2.5, 9.5, and 1.53‰ respectively, while these values for all $\delta^{13}C_s$ samples collected in Nebraska were -5.0, 12.6, and 2.55‰ respectively.

Tecsa et al. (2020) reported the age and $\delta^{13}C$ of nearly 100 samples of SOM and pedogenic calcite from a 5.6 m continuous vertical profile of soils and paleosols near southern areas of the Sand Hills about 200 km south of the Middle Loup River (Study #10 in Figure 4). All but 1 sample with age <13,000 yr had $\delta^{13}C_s$ between 0 and -5‰ and the majority had $\delta^{13}C_s$ between -1 and -3‰. The outlier sample had a value of +2.88‰, and was measured at a depth of 2.45 m. Given that the maximum unadjusted age of any groundwater sample collected for the present study did not exceed 10,000 yr (as shown later in Chapter 5), and the maximum age of the landscape surrounding the Middle Loup River was 11,000 yr as mentioned above, the $\delta^{13}C_s$ encountered by groundwater in the shallow subsurface would likely have been between -1 and -3‰. Also, given the age of the paleosols in which these carbonates formed (700 to 13,000 yr), it is likely that the pedogenic carbonates in the shallow subsurface have $^{14}C_s > 0$ pmc, though no published data were found on $^{14}C_s$ in or near the study site.

$\delta^{13}C_g$ values may be more variable than $\delta^{13}C_s$ in the Sand Hills due to the seasonality of groundwater recharge and soil respiration (McMahon et al. 2007; Hartman 2015). Miao et al. (2007) performed a similar study to that of Tecsa et al. (2020), measuring the age and $\delta^{13}C_{SOM}$ of a 6 m profile of loess fields of southwest Nebraska. The 6 m profile represented a nearly continuous 10,000 yr record of $\delta^{13}C_{SOM}$ at their site; the majority of $\delta^{13}C_{SOM}$ values were between -17 and -13‰. At high soil respiration rates these $\delta^{13}C_{SOM}$ values would lead to $\delta^{13}C_g$ values of -13 to -9‰. In winter when soil respiration rate drops to nearly zero (Hartman 2015), $\delta^{13}C_g$ would likely be closer to atmospheric value (Cerling et al. 1991), which prior to the onset of large scale fossil fuel combustion was about -6.5‰ and is presently about -8‰ (Graven et al. 2016).

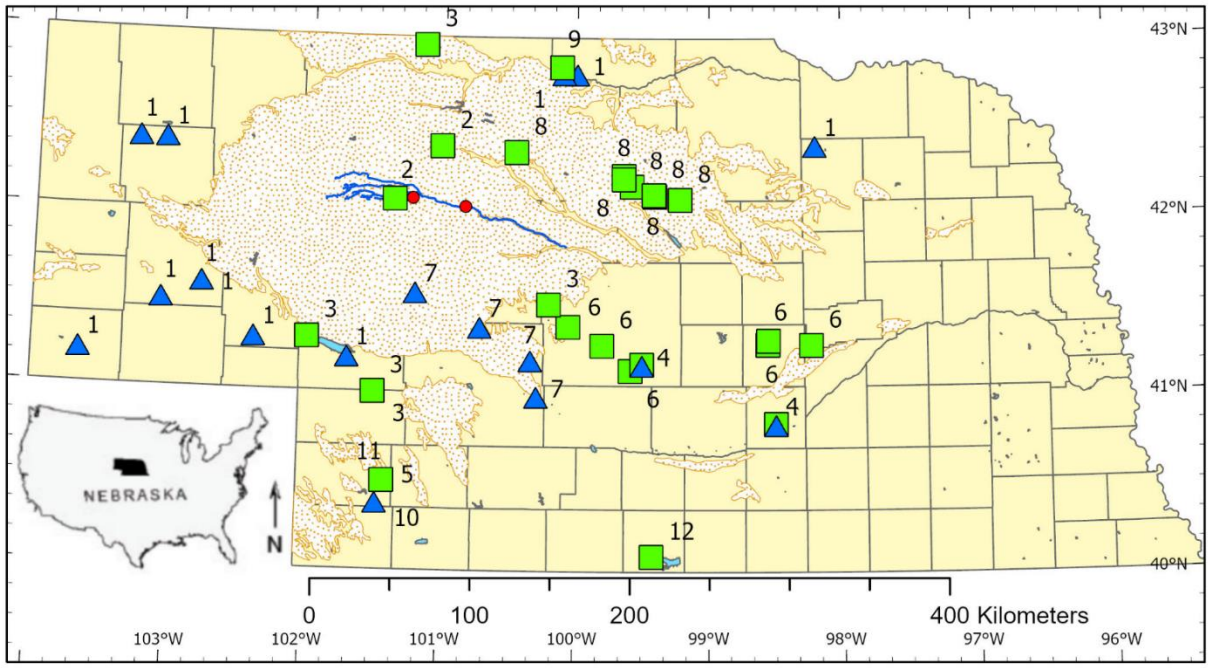

ID	Study Name
1	Fox and Koch 2003
2	Goble et al. 2004
3	Johnson and Willey 2000
4	Kelly et al. 1991
5	Mason et al. 2008
6	May 2003
7	McMahon et al. 2007
8	Moussel 2007
9	Steuter et al. 1990
10	Tecsa et al. 2020
11	Woodburn et al. 2017
12	Layzell and Mandel 2020

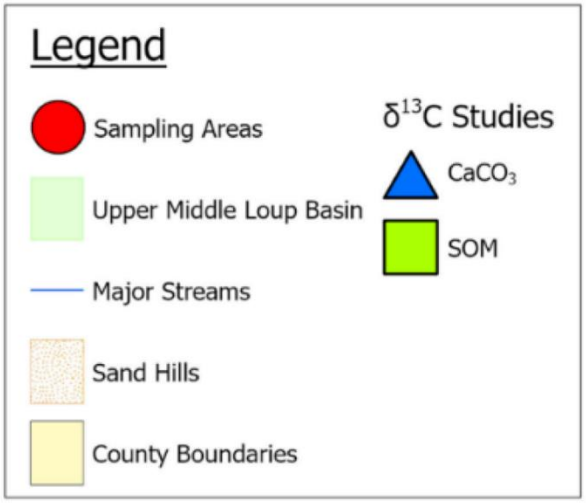

Figure 4. Sampling locations of studies reporting δ13C of SOM (green squares) or carbonate mineral solids (likely calcite, blue triangles) throughout Nebraska.

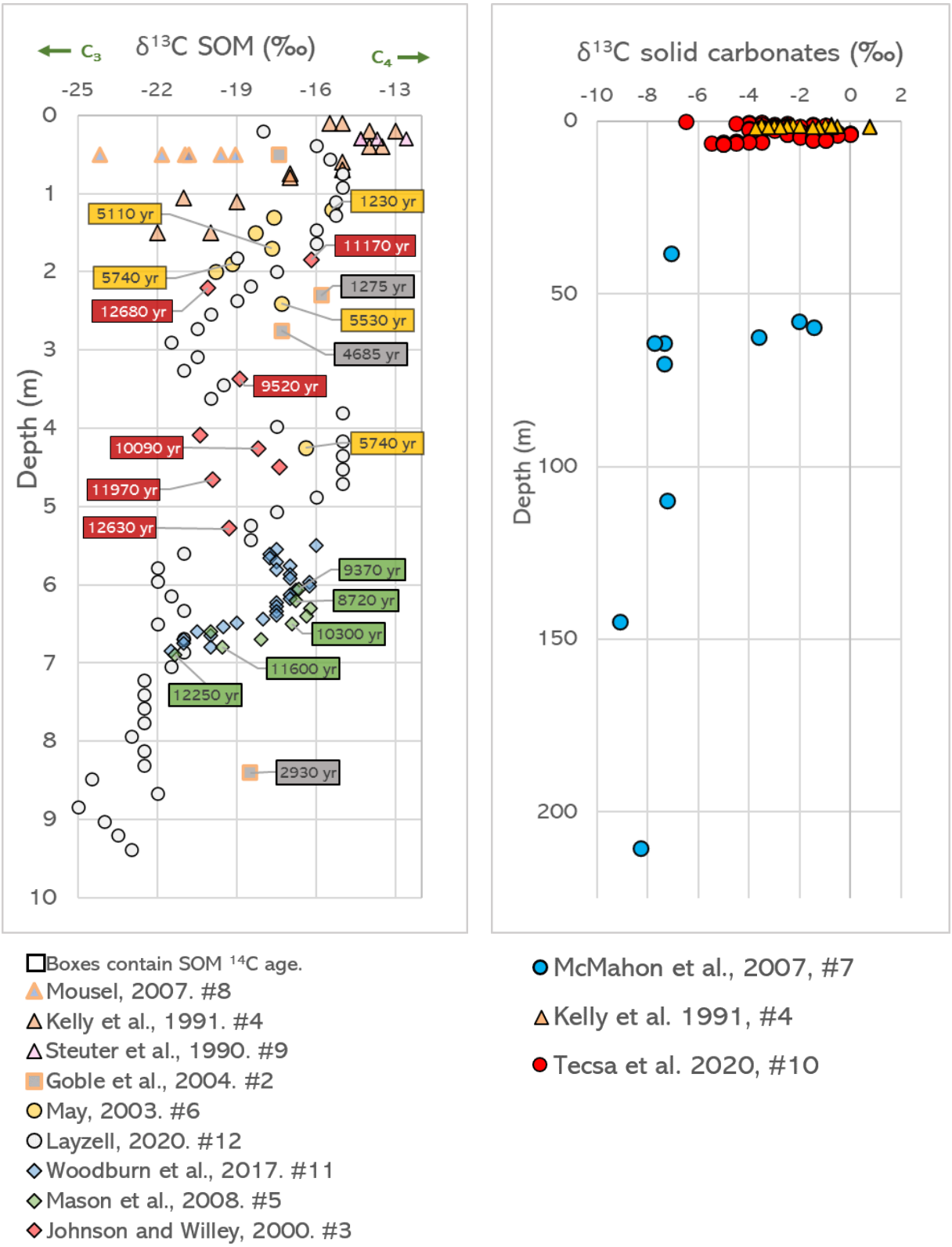

Figure 5. Variation of $\delta^{13}C_{SOM}$ (left) and $\delta^{13}Cs$ (right) with depth as reported by sources listed in Table 1.

Table 1. Summary of $\delta^{13}C$ values measured in SOM and carbonates throughout the Great Plains. Variation in $\delta^{13}C$ of material analyzed is controlled in part by the relative abundance of C3 vs C4 plants rooted in a soil during pedogenesis. Values in the study ID column correspond to locations shown in Figure 4. Values in the "ALL" rows show the total number of samples, the minimum value, maximum value, and mean of all reported values for each category ($\delta^{13}C$ of SOM or $\delta^{13}C$ of $CaCO_3$). The $\delta^{13}C$ of $CO_{2(g)}$ column shows the average $\delta^{13}C$ of SOM plus 4.4‰ for the SOM studies, based on Cerling et al. (1991), and $\delta^{13}C$ of $CaCO_3$ minus 15‰ for solid carbonate studies based on Cerling et al. (1989) and Fox and Koch (2003); see text for explanation.

Study ID	Study	Material Analyzed	Number of Samples	$\delta^{13}C$ Min (‰)	$\delta^{13}C$ Max (‰)	Median (‰)	Average (‰)	$\delta^{13}CO_{2(g)}$ Estimated
Studies Reporting $\delta^{13}C$ of Soil Organic Matter (SOM)								
2	Goble et al. 2004	Dune Paleosols	4	-17.4	-17.3	-17.4	-17.4	-13.0
3	Johnson and Willey 2000	Loess Paleosols	8	-20.4	-17.4	-19.1	-18.8	-14.4
4	Kelly et al. 1991	Prairie Soils	14	-22.0	-13.0	-15.3	-16.5	-12.1
5	Mason et al. 2008	Loess Paleosols	9	-21.3	-16.2	-16.9	-18.0	-13.6
6	May 2003	Fluvial Terraces	8	-18.3	-17.3	-17.7	-17.7	-13.3
8	Moussel 2007	Wetland Soils	13	-24.2	-17.7	-20.8	-21.1	-16.7
9	Steuter et al. 1990	Prairie Soils	4	-14.3	-12.6	-14.0	-13.7	-9.3
11	Woodburn et al. 2017	Loess Paleosols	27	-21.5	-16.0	-17.5	-18.1	-13.7
12	Layzell et al. 2020	Alluvial Fan	52	-25.0	-15.0	-20.3	-19.5	-15.1
	All SOM	**All SOM**	**139**	**-25.0**	**-12.6**	**-18.3**	**-18.6**	**-14.2**
Studies Reporting $\delta^{13}C$ of $CaCO_3$								
4	Kelly et al. 1991	Carbonates, bulk soil	22	-3.8	0.8	-2.1	-1.8	-16.8
1	Fox & Koch 2003	Pedogenic Carbonates	273	-8.7	-0.7	-6.7	-6.3	-21.3
7	McMahon 2007	Bulk Carbonate	10	-8.3	-1.4	-7.3	-6.1	-21.1
10	Tecsa et al. 2020	Bulk Carbonate	94	-4.5	-1.0	-2.5	-2.4	-17.4
	All $CaCO_3$	**All $CaCO_3$**	**399**	**-8.7**	**0.8**	**-6.0**	**-5.1**	-20.1

Table 2. Summary statistics for $\delta^{13}C$ values. All $\delta^{13}C$ values of SOM come from samples collected in Nebraska (NE), in the Sand Hills or the surrounding loess plains. Carbonate $\delta^{13}C$ values are shown for different sets of samples, from NE and beyond.

$\delta^{13}C$ of Organic Matter	**Number of Samples**	**Mean**	**Min**	**Max**	**Median**	**Range**	**Standard Deviation**
All $\delta^{13}C_{SOM}$ Samples	139	-18.61	-25.0	-12.6	-18.3	12.40	2.770
$\delta^{13}C$ of $CaCO_3$	**Number of Samples**	**Mean**	**Min**	**Max**	**Median**	**Range**	**Standard Deviation**
All $\delta^{13}C_s$ Samples	399	-5.13	-9.6	3.0	-6.0	12.60	2.35
Samples from NE, KS	300	-4.54	-9.6	3.0	-4.9	12.60	2.46
Samples from NE	240	-4.64	-9.6	3.0	-5.0	12.60	2.55
Samples collected from ≤ 6m depth NE	116	-2.39	-6.5	3.0	-2.5	9.50	1.53

3. Sampling Design

During three sampling campaigns which took place during May 2019, August 2019, and September 2020, 100 groundwater samples were collected from 50 cm below the riverbed at the five sampling areas (Figure 3 and Table 3), using a narrow steel piezometer with a 5 cm screen, inserted such that the top of the screen was 50 cm below the top of the riverbed. Each of these samples was analyzed for $^{14}C_{DIC}$, $\delta^{13}C_{DIC}$, and $^{3}H/^{3}He$. During the May 2019 campaign, 65 samples were collected. After this, samples at the 40 km sampling area were collected in August 2019 (n=21), and transects 13580, 20780 and 20910 were resampled in September of 2020 (n=14). Finally, in December of 2020 ^{14}C, $\delta^{13}C$, and major ion data were collected from groundwater monitoring wells in the study area (Table 4) to determine if groundwater in the shallow aquifer was isotopically and or chemically similar to the samples collected from beneath the riverbed.

Table 3. Riverbed groundwater sampling summary. Transect ID is the distance downstream from the zero point (Fig. 3) to the transect measured along the channel in meters. Sampling campaign indicates the month and year of sample collection.

Sampling Area	**Transect ID**	**Number of samples**	**Sampling Campaign**
6 km	6300	3	May 2019
6 km	6400	3	
6 km	6590	3	
13 km	13235	8	
13 km	13580	4	
13 km	13700	4	
20 km	20300	5	
20 km	20460	5	
20 km	20780	5	
20 km	20910	5	
99 km	99090	10	
99 km	99100	10	
40 km	40500	6	Aug. 2019
40 km	40550	5	
40 km	40600	5	
40 km	40670	5	
13 km	13580	4	Sept. 2020
20 km	20780	5	
20 km	20910	5	

Sample points are named such that the leading number is the distance downstream from the zero point (Figure2) to the sampling transect along the channel, the letter indicates whether the

sampling point was in the center of the channel (C) or to the right (R) or left (L) of center, and the trailing number is the distance from channel center in decimeters. At each of the five sampling areas, sampling points were arranged in 2 to 4 transects across the channel, perpendicular to the direction of stream flow (Figure 3, Table 3). The goal in sampling points spanning the width of the riverbed was to sample the full range of flowpaths and groundwater transit times to the river. Flowpaths that originate closer to a gaining stream tend to be shorter, shallower, and terminate closer to the banks. Flowpaths originating further from the channel tend to be longer, deeper, and terminate closer to the center of the stream. Thus, groundwater seepage into gaining streams will often increase in age with distance from the bank to the center of the channel (Browne and Guldan 2005; Kennedy et al. 2009; Gilmore et al. 2016). Age may also increase with distance downstream (Modica et al. 1998). Coupling groundwater age dating with the groundwater seepage rate through the riverbed (specific discharge) at each sampling point allowed flow-weighting of the age results in this work, an important aspect of estimating the groundwater transit time distribution (Kennedy et al. 2009, Gilmore et al. 2016).

Table 4. Groundwater monitoring wells sampled for C isotopes and major ions. Depth to water measurements on the 9-GSL-94 wells were taken by Aaron Young (UNL Conservation and Survey Division Geologist) on 9/24/2020, all other depth to water measurements were completed as listed in the "Sampling Date" column. Well installation dates and locations are from the Nebraska Department of Natural Resources registered wells database (https://www.nebraskamap.gov/).*BGS= below ground surface**Depth to water for GSL-01-03 was measured during well installation.

Well Name	Sampling Date	Well Installation Date	Depth to top of screen (m) BGS*	Screen Length (m)	Depth to water (m) BGS	Lat	Long
9-GSL-94-S	8/11/2020	03/28/1994	1.14	3.05	1.60	42.07132	-101.4064
9-GSL-94-M1	8/11/2020	03/28/1994	17.68	0.91	1.49	42.07132	-101.4064
9-GSL-94-M2	8/11/2020	03/28/1994	22.49	0.61	1.41	42.07132	-101.4064
9-GSL-94-D	8/11/2020	03/28/1994	29.63	1.52	1.59	42.07132	-101.4064
01-GSL-2020-S	12/8/2020	08/12/2020	7.96	0.30	6.53	42.06797	-101.361
01-GSL-2020-M1	12/8/2020	08/12/2020	9.45	0.30	6.46	42.06797	-101.361
01-GSL-2020-M2	12/8/2020	08/12/2020	12.10	0.30	6.43	42.06797	-101.361
01-GSL-2020-D	12/8/2020	08/11/2020	121.25	1.52	7.93	42.06797	-101.361
01-SEN-2020-S	12/7/2020	08/04/2020	7.32	0.61	4.43	42.04654	-100.8331
01-SEN-2020-M	12/7/2020	08/04/2020	19.14	0.91	3.57	42.04654	-100.8331
01-SEN-2020-D	12/7/2020	08/05/2020	35.36	3.05	3.36	42.04654	-100.8331
GSL-01-03**	4/26/2019	07/17/2003	176.78	24.38	1.37	42.0828	-100.833

At each sampling point, the first step was measurement of basic groundwater quality parameters (dissolved oxygen, conductivity, temperature, and pH) in the field by pumping the groundwater through a low-volume flow cell containing a multiparameter probe. Next, a groundwater sample for analysis of $\delta^{13}C$, ^{14}C, and DIC (dissolved inorganic carbon) was collected using established protocols from the National Ocean Sciences Accelerator Mass Spectrometry laboratory (NOSAMS) at the Woods Hole Oceanographic Institution (https://www2.whoi.edu/site/nosams/).

Groundwater specific discharge was determined at each of the 100 sample points, by collaborators using the automated seepage meter of Solomon et al. (2020). Also, 38 of the 100 riverbed groundwater samples were analyzed for alkalinity and major ions. Alkalinity and major ion concentrations were analyzed at the Nebraska Water Sciences Laboratory. $\delta^{13}C$, ^{14}C, and DIC were analyzed at NOSAMS. ^{14}C was reported by NOSAMS normalized to a $\delta^{13}C$ value of -25‰. Because this

normalization is unnecessary in groundwater age-dating calculations, data were de-normalized following the procedure of Mook and van der Plicht (1999) prior to use in age analysis.

4. Methods

4.1. Analytical Methods

Groundwater $\delta^{13}C_{DIC}$ and $^{14}C_{DIC}$ were analyzed at the NOSAMS facility at the Woods Hole Oceanographic Institution following the methods outlined by Gospodinova et al. (2016) and Shah Walter et al. (2015). The extraction method uses a gas-polymer membrane contactor to extract all DIC from a sample in the form of $CO_{2(g)}$. CO_2 extracted from the sample was cryogenically isolated from the helium carrier gas and subsequently graphitized before analysis. Analysis of $^{14}C_{DIC}$ involved the simultaneous direct counting of the number of ^{14}C atoms in the sample and in the ^{14}C standard (NBS Oxalic Acid I, NIST-SRM-4490). A process blank devoid of ^{14}C was analyzed alongside the standard and sample (NOSAMS memo, May 25, 2020, General Statement of ^{14}C Procedures at the National Ocean Sciences AMS Facility). $^{14}C_{DIC}$ was reported as fraction modern (F_m), which is "a measurement of the deviation of the $^{14}C/^{12}C$ ratio of a sample from the "modern" standard" (NOSAMS memo May 25, 2020, General Statement of ^{14}C Procedures at the National Ocean Sciences AMS Facility). Modern is defined by Olsson (1970) as 95% of the radiocarbon concentration of NBS Oxalic Acid I standard normalized to $\delta^{13}C$ Vienna Pee Dee Belemnite (VPDB) value of -19‰. NOSAMS calculates both an internal statistical error, and an external error for ^{14}C measurements. The larger of the two values is reported (https://www2.whoi.edu/site/nosams/). The internationally recognized standard for $\delta^{13}C$ is the VPDB, the standard value of which is 0‰. NOSAMS applies a correction to the reported $^{14}C_{DIC}$, to normalize the result to a $\delta^{13}C_{DIC}$ value of -25‰. NOSAMS measured $\delta^{13}C$ on a sample of $CO_{2(g)}$ split from each groundwater sample prior to graphitization. Analysis was performed using either a VG PRISM or VG OPTIMA mass spectrometer. NOSAMS also measured DIC concentration in the process of $^{14}C_{DIC}$ analysis, the results of which were reported in mmol DIC per kg H_2O. Error associated with DIC concentration is estimated to be about 2% (personal communication, February 5, 2021, Roberta Hansman).

Analysis of Na^+, K^+, Ca^{2+}, Mg^{2+}, Br^-, Cl^-, F^-, NO_3^-, NO_4^-, PO_4^{3-}, SO_4^{2-}, alkalinity and SiO_2 was performed at the University of Nebraska Lincoln Water Sciences Laboratory. Ca^{2+}, K^+, Mg^{2+}, and Na^+ were analyzed via atomic absorption spectrophotometry following Standard Methods 3111 (Lipps et al. 2018a). Br^-, Cl^-, F^-, NO_3^-, NO_4^-, PO_4^{3-}, and SO_4^{2-} were analyzed via ion chromatography following EPA Method 300 "Determination of Inorganic Anions by Ion Chromatography" (Pfaff 1993). Alkalinity was analyzed via potentiometric titration, following Standard Methods 2320B.(Lipps et al. 2018b)

4.2.Estimation of Groundwater Age

4.2.1. Overview

The equation used for calculating the ^{14}C age of a groundwater sample is:

$$t = -\frac{t_{1/2}}{\ln 2}\ln\left(\frac{^{14}C_{DIC}}{^{14}C_{REF}}\right) = -\left(\frac{5730\,yr}{\ln 2}\right)\ln\left(\frac{^{14}C_{DIC}}{^{14}C_{REF}}\right) \quad (1)$$

where t is the age of the sample, $t_{½}$ is the radioactive half-life of ^{14}C (5,730 ± 40 yr), $^{14}C_{DIC}$ is the ^{14}C activity of the groundwater DIC, and $^{14}C_{REF}$ is the reference ^{14}C activity used for groundwater dating. The ^{14}C of DIC can be affected by processes such as dissolution or precipitation of calcite or other carbonates, oxidation of organic matter, and isotopic exchange between DIC and other C phases. These processes can alter the $^{14}C_{DIC}$ activity in groundwater, and lead to groundwater age being under- or overestimated. Because of this dating groundwater with $^{14}C_{DIC}$ requires age to be calculated from a

reference ^{14}C activity ($^{14}C_{REF}$) that accounts for all processes, other than radioactive decay, which affect $^{14}C_{DIC}$.

Two common approaches were used to correct for the geochemical processes affecting $^{14}C_{DIC}$, and estimate the ^{14}C age of groundwater samples collected for this study. The first approach was to apply five of the most commonly used models for groundwater geochemical ^{14}C age correction (Section 4.2.2). These models are referred to as "single sample models" because each is applied to samples individually, one sample at a time (in contrast to another approach described below that is based on pairs of samples). The single sample models correct for changes to $^{14}C_{DIC}$ that are not caused by radioactive decay (ageing). For example, when calcite with ^{14}C = 0 pmc dissolves into groundwater, $^{14}C_{DIC}$ decreases in proportion to the amount of DIC contributed by the dissolution of calcite. If the ^{14}C age of this groundwater was calculated assuming (incorrectly) that $^{14}C_{DIC}$ was < 100 pmc due only to radioactive decay, the calculated age would be an overestimate. Each single sample model calculates a $^{14}C_{REF}$ value that accounts for changes to $^{14}C_{DIC}$ that were not caused by radioactive decay. However, the application of these models has typically been in aquifers composed largely of ancient marine limestones free of ^{14}C (Fontes and Garnier, 1979; Fontes 1992; Clark and Fritz 1997); in comparison to such aquifers, the High Plains Aquifer has a much lower content of carbonate minerals, and the carbonates present are younger pedogenic calcite that might contain ^{14}C.

The second approach was to estimate groundwater ^{14}C age using the inverse geochemical modeling software NETPATH (Plummer et al. 1994; Parkhurst and Charlton 2008). NETPATH is designed to calculate $^{14}C_{REF}$ by accounting for the net geochemical reactions occurring between the aquifer media and groundwater as groundwater chemistry evolves along a flowpath. NETPATH can also be used to model isotopic evolution of groundwater along flowpaths and estimate ^{14}C age of groundwater based on chemical and isotopic differences between upgradient and downgradient groundwater samples (Parkhurst and Charlton, 2008). This software can account for many more geochemical reactions than the single sample models but may also require more data about aquifer geochemistry.

When dating organic material radiocarbon activity is commonly normalized to a $\delta^{13}C$ value of -25‰ and adjusted to represent ^{14}C content in the year 1950 (Mook and van der Plicht, 1999). These corrections are extraneous in groundwater ^{14}C dating, and as such, values of $^{14}C_{DIC}$ reported here have been denormalized using equations 12 and 17 of Mook and van der Plicht (1999). I use the notation of Mook and van der Plicht, using percent modern carbon (pmc) throughout this work to distinguish that the $^{14}C_{DIC}$ value being referenced is the denormalized ^{14}C content of the DIC in the year that the sample was collected.

4.2.2. Single Sample Models

$^{14}C_{REF}$ was calculated for each riverbed groundwater sample using five single sample models discussed below: the "Tamers", "Ingerson and Pearson," "IAEA," "Han and Plummer," and "Tamers Mass Balance" models. Each model accounts for changes in $^{14}C_{DIC}$ due to the addition of DIC from carbonate minerals (e.g., calcite) (equation 2), and/or due to isotope exchange between DIC and other carbon sources (CO_2 or carbonate minerals) present in the subsurface.

Dissolution of calcite in water that is in contact with gaseous CO_2 (reaction 2) produces one mole of Ca^{2+} for every two moles of DIC, based on the net stoichiometry of equation (reaction) 2.

$$CaCO_3 + CO_2 + H_2O \rightarrow Ca^{2+} + 2HCO_3^- \quad (2)$$

In equation 2, two HCO_3^- molecules are produced, with one of the C atoms sourced from calcite and the other from CO_2. The single sample models based on measurements of concentrations of DIC species are rooted in the assumption that all of the aqueous CO_2 and half of the HCO_3^- are sourced from recently living plant material with ^{14}C activity similar to that of the atmosphere, and half of the HCO_3^- is sourced

from carbonate minerals (which often have ^{14}C much lower than that of the atmosphere due to ^{14}C decay over time)(Tamers 1967, 1975). For groundwater samples in which much but not necessarily all DIC was generated by the process in equation 2, Tamers (1967) developed an equation to calculate the approximate fraction of DIC sourced from recent plant material:

$$F = \frac{[DIC] - 0.5[HCO_3^-]}{[DIC]} \quad (3)$$

where the "Tamers F" is the fraction of carbon in the DIC sourced from plant materials and 1-F is the fraction of DIC sourced from carbonate minerals (Tamers 1975). Tamers (1975) showed that values of F ranged between about 0.52 and 0.88 in groundwater samples, with values above 0.52 reflecting slow kinetics of calcite dissolution (groundwater in which equation 2 had not yet reached its equilibrium value of about 0.52).

The single sample models rely on several chemical and isotopic variables (Table 5), including the concentrations of DIC species and the $\delta^{13}C$ and ^{14}C content of carbon sources present in the subsurface. Further information regarding the assumptions, limitations, and applicability of these models can be found in Fontes (1992), Clark and Fritz (1997), Geyh (2000) , Plummer and Glynn (2013), Han and Plummer (2016), and Cartwright et al. (2020).

The “Tamers” model (Tamers 1967; Tamers 1975) :

$$^{14}C_{REF} = F \cdot ^{14}C_g + \left(1 - F\right) \cdot ^{14}C_s$$

Equation 4. Tamers proposed that DIC is produced by equation 2 above, which would lead to DIC with Tamers F (equation 3) equal to about 0.52 if all DIC were generated by equation 2). But he also recognized that actual F values in real groundwater samples were usually greater than 0.52, indicating slow calcite dissolution and that DIC acquisition is not defined completely by equation 2. Equation 4 does not account for C isotope exchange between DIC and other C pools such as soil CO2 or carbonate minerals.

The “Ingerson and Pearson” model (Ingerson and Pearson 1964; Pearson and White 1967; Pearson and Hanshaw 1970; Pearson et al. 1972; Pearson and Swarzenki 1974):

$$^{14}C_{REF} = \frac{^{14}C_g(\delta^{13}C_s - \delta^{13}C_{DIC}) + ^{14}C_s(\delta^{13}C_{DIC} - \delta^{13}C_g)}{(\delta^{13}C_s - \delta^{13}C_g)}$$

Equation 5. The Ingerson and Pearson is an isotopic mixing model which assumes that DIC is a mixture of C from soil CO_2 and carbonate minerals. It calculates $^{14}C_{REF}$ using the $\delta^{13}C$ value measured in DIC, and the assumed or measured values of $^{14}C_g$, $\delta^{13}C_g$, $^{14}C_s$, and $\delta^{13}C_s$. The Ingerson and Pearson model does not use DIC concentration to calculate $^{14}C_{REF}$.

Table 5. Description of variables used in the single sample models and NETPATH. Modified in part from Han and Plummer (2016).

Term	Description	Unit	Determination/Calculation
$^{14}C_{REF}$	Reference ^{14}C value for calculation of groundwater ^{14}C age.	pmc	$^{14}C_{REF}$ was calculated using the single sample models, or NETPATH.
C_a, C_b, C_c, C_{DIC}	Molar concentrations of dissolved carbon dioxide, bicarbonate, carbonate, and total DIC. C_a = $[CO_{2(aq)}]$, C_b = $[HCO_3^-]$, C_c=$[CO_3^-]$, C_{DIC} = [DIC].	mol/kg	C_{DIC} was measured in each sample. C_a, C_b, and C_c were calculated using the sample's pH, DIC, temperature, and the disassociation constants of carbonic acid.
$^{14}C_g$, $\delta^{13}C_g$	Carbon isotopic composition of soil gas CO_2.	pmc, ‰	$^{14}C_g$ was assumed to equal 100 pmc. See text of Section 4.2.2 for details. $\delta^{13}C_g$ was estimated based on C isotope content of (1) the groundwater samples or (2) SOM present in the study area.
$^{14}C_s$, $\delta^{13}C_s$	Carbon isotopic composition of solid carbonate minerals (usually calcite).	pmc, ‰	$\delta^{13}C_s$ was estimated based on $\delta^{13}C$ values of pedogenic carbonates in/near the study area. $^{14}C_s$ was estimated based on ^{14}C isotope content of (1) the groundwater samples or (2) SOM in/near the study area.
$^{14}C_{DOL}$	^{14}C Carbon isotopic composition of dolomite.	pmc	$^{14}C_{DOL}$ was assigned the same values as $^{14}C_s$ which varied across modeling scenarios.
$^{14}C_{a1}$, $\delta^{13}C_{a1}$	Carbon isotopic composition of dissolved CO_2 in isotopic equilibrium with soil gas CO_2.	pmc, ‰	$^{14}C_{a1} = {}^{14}C_g + 0.2\varepsilon_{ag} \approx 100$ pmc $\delta^{13}C_{a1} = \delta^{13}C_g + \varepsilon_{ag}$
$^{14}C_i$, $\delta^{13}C_i$	Carbon isotopic composition of dissolved HCO_3^- prior to isotopic exchange	pmc, ‰	$^{14}C_i = 0.5(^{14}C_{a1} + {}^{14}C_s)$ $\delta^{13}C_i = 0.5(\delta^{13}C_{a1} + \delta^{13}C_s)$
ε_{gb}	^{13}C fractionation factor of gaseous CO_2 relative to HCO_3^-	‰	ε_{gb} = -9483/T + 23.89, e.g., at 10°C ε_{gb} = -9.60‰, meaning bicarbonate in isotopic equilibrium with soil CO_2 is 9.60‰ enriched (heavier) in $\delta^{13}C$ compared to the soil CO_2.
ε_{sb}	^{13}C fractionation factor of calcite relative to HCO_3^-.	‰	ε_{sb} = -4232/T + 15.1, e.g., at 10°C ε_{sb} = 0.15‰, meaning bicarbonate in isotopic equilibrium with solid calcite is -0.15‰ depleted (lighter) in $\delta^{13}C$ compared to calcite.

The "Han and Plummer" model (Han and Plummer 2013; Han and Plummer 2016) :

$$^{14}C_{REF} = \left(\frac{C_a}{C_{DIC}} {}^{14}C_{a1} + \frac{C_b}{C_{DIC}} {}^{14}C_i \right) + \left({}^{14}C_x - {}^{14}C_i - 0.2\varepsilon_{xb} \right) \cdot \frac{\delta^{13}C_{DIC} - \frac{C_a}{C_{DIC}} \delta^{13}C_{a1} - \frac{C_b}{C_{DIC}} \delta^{13}C_i}{\delta^{13}C_x - \delta^{13}C_i - \varepsilon_{xb}}$$

Equation 6. The Han and Plummer model accounts for dissolution of solid carbonate minerals as well as isotope exchange between DIC and soil CO_2, or between DIC and solid carbonates. The model adds a correction term for C isotopic exchange to the Tamers model. Depending on whether the isotopic exchange is between DIC and soil CO_2 or between DIC and solid carbonate, the subscript 'x' in Equation 6 is replaced with either 'g' (for soil gas CO_2) or 's' (for solid carbonate minerals). When modeling isotope exchange between DIC and soil CO_2, the Han and Plummer model yields $^{14}C_{REF}$ values within ±1 pmc of the Mook model (Mook 1976), which simulates the same process (Han and Plummer 2012).

The "IAEA" model (Salem et al. 1980):

$$^{14}C_{REF} = \frac{(\delta^{13}C_{DIC} - \delta^{13}C_s)({}^{14}C_g - {}^{14}C_s) + ((\delta^{13}C_g - \varepsilon_{gb} - \delta^{13}C_s)^{14}C_s)}{(\delta^{13}C_g - \varepsilon_{gb} - \delta^{13}C_s)}$$

Equation 7. The IAEA model. Like the Ingerson and Pearson model, the IAEA model does not rely on carbonate species aqueous concentrations (C_a, C_b, or DIC) to calculate $^{14}C_{REF}$, instead relying on C isotope values of DIC, soil gas CO_2, and solid carbonate minerals. The IAEA model assumes that complete isotope exchange between DIC and soil CO_2 occurs prior to the groundwater becoming isolated from interaction with soil CO_2.

The "Tamers Mass Balance" model (Plummer et al. 1990; Plummer et al. 1994; Plummer and Glynn 2013) :

$$^{14}C_{REF} = \frac{\left[{}^{14}C_s \left(\Delta Ca - \Delta Mg - \Delta SO_4 \right) + {}^{14}C_g (\Delta C_{DIC} - \Delta Ca - \Delta Mg + \Delta SO_4) + (2 \cdot {}^{14}C_{DOL} \cdot \Delta Mg) \right]}{C_{DIC}}$$

Equation 8. The "Tamers Mass Balance" model is a single sample model first used by Plummer et al. (1990) which assumes that $^{14}C_{REF}$ is controlled by CO_2, calcite, dolomite, and gypsum. This model uses measured or assumed values of $^{14}C_s$, $^{14}C_g$, and the ^{14}C content in dolomite ($^{14}C_{DOL}$), along with Ca, Mg, SO_4, and DIC concentration to calculate $^{14}C_{REF}$. Δ refers to the change in concentration between pure H_2O and the concentration of an ion in the sample being modeled (Plummer and Glynn 2013). This model was first used by Plummer et al. (1990) on the Madison aquifer approximately 100 km northwest of our field site.

The "Mook" model (Mook 1972; Mook 1976; Mook 1980), the "Fontes and Garnier" model (Fontes et al. 1978; Fontes and Garnier 1979; Fontes 1983), and the "Oeschger" model (described in Geyh (2000), and Han and Plummer (2016)), were also applied to our samples. The Han and Plummer model simulates the geochemical reactions implied by both the Fontes and Garnier model and the Mook model. As such, these models are not discussed here. The Oeschger model is mentioned both in Geyh (2000) and Han and Plummer (2016) but does not appear to be published elsewhere. Geyh (2000) asserts that the model was proposed by Hans Oeschger in 1972 but does not provide citation to an associated publication. Due to the lack of documentation surrounding this method, values calculated via the Oeschger model are not reported here.

4.2.3. NETPATH

NETPATH requires the definition of an upgradient "initial water" which evolves chemically and isotopically toward a downgradient "final water." The point of the model is to quantify all the net chemical mass transfers into and/or out of the groundwater, per unit volume of groundwater, to explain its chemical evolution from initial water to final water. Any mass transfers that affect ^{14}C of groundwater DIC are relevant to estimating the age of the final water.

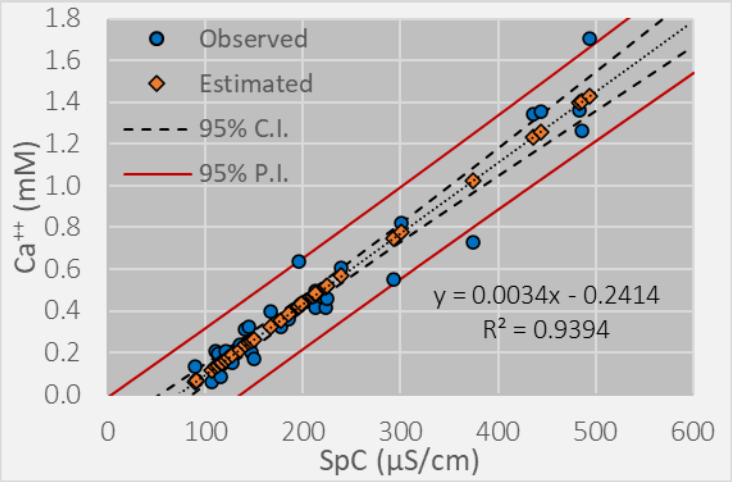

Figure 6. Regression of calcium concentration vs. specific conductance in groundwater samples, used to estimate calcium concentration in samples not analyzed for major ions. Measured values are shown as blue circles. Values estimated from regression are shown as orange diamonds. 95% confidence interval of the regression is shown as dashed black lines. 95% prediction interval is shown as red lines.

The user enters constraints and phases into the program to set the conditions of the model. Quoting from Plummer et al. (1994), page 8, "A constraint is typically a chemical element, but may also be an expression of electron conservation (termed redox state) or conservation of a particular isotope of an element. A constraint is included in the model to constrain the masses of selected phases (minerals and gasses) that can enter or leave the aqueous solution. The constraints selected for the model will determine the number and types of phases that need to be selected to solve the modeling problem." A phase is "any mineral or gas that can enter or leave the aqueous solution along the evolutionary path" (page 12, Plummer et al. 1994). Each constraint defines the total mass of an element in the groundwater or the conservation of an isotope from initial to final water. Elements enter or leave the groundwater through "phases" (minerals or gasses) that dissolve into groundwater, precipitate out of groundwater, or exchange with the aquifer matrix. For example, if carbon is chosen as a constraint, the difference in measured carbon concentration between the initial and final waters is calculated, and the model determines the mass of carbon that must be added to or subtracted from each unit volume of groundwater (by dissolving or precipitating phases) in order to account for the measured concentration difference. NETPATH then determines what chemical reactions could explain the concentration difference, using only the phases selected by the user (Plummer et al. 1994).

Review of the literature provided information regarding the primary constituents comprising the sediments of the Sand Hills and Ogallala group. Given the goal of calculating groundwater ^{14}C age, I prioritized identification of subsurface DIC sources that could alter the $^{14}C_{DIC}$ signature. As noted in section 2.2 thick layers of peat are present in interdunal wetlands throughout the central Sand Hills. The presence of secondary carbonates is also well documented (Kelly et al. 1991; Gardner et al. 1992; Fox and Koch 2003; Fox and Koch 2004; Tecsa et al. 2020). These two substances are the primary potential sources for DIC below the water table in the study area. NETPATH modeling was performed using just two constraints: carbon and calcium. Because each sample had not been analyzed for major ions, the calcium concentration of some samples was estimated using the linear regression of SpC and Ca (Figure 6).

Phases included in the NETPATH models were calcite, CH_2O (a proxy for solid organic matter in the form of carbohydrate), and $CO_{2(g)}$, each with assigned C isotope values. The CH_2O phase was only allowed to enter (not precipitate from or leave) the groundwater system. All negative C mass transfers

that could not be accounted for by calcite precipitation occurring in the form of CO_2 evasion. $^{14}C_g$ = 100 pmc was used in all simulations. This is a widely used assumption in ^{14}C groundwater age dating (Han and Plummer 2016; Cartwright 2020), which improves our ability to compare ages derived from our study to previous groundwater age research (Solder and Jurgens 2020). The values of $\delta^{13}C_s$ and $\delta^{13}C_{CH2O}$ used in NETPATH modeling were based on the averages presented in Table 2. As explained in section 5.3.1, values for $^{14}C_s$, $^{14}C_{CH2O}$ and $\delta^{13}C_g$ varied across modeling scenarios and were based on C isotope data from the literature and from groundwater samples collected for this study.

4.3. Estimating the Groundwater Transit Time Distribution

To better understand the extent to which relatively old groundwater contributes to total groundwater discharge through the riverbed at the study site, the ^{14}C groundwater ages were flow-weighted to compute a groundwater transit time distribution (TTD) based on the samples from the 40 and 99 km sampling areas (the samples that proved to be amenable to ^{14}C dating). Because all ages were determined at the ends of groundwater flowpaths, just below the riverbed, the ages correspond to groundwater transit times (i.e., travel times from groundwater recharge at the water table to discharge at the riverbed). The age at each riverbed sampling point was weighted by the groundwater specific discharge through the riverbed at the same point. Specific discharge values were determined by collaborators at the University of Utah and the University of Nebraska using the automated seepage meter of Solomon et al. (2020). To calculate the flow weighted cumulative transit time distribution, I divided each specific discharge measurement (q) by the sum of all 41 such measurements at 40 and 99 km (q_{TOT}). The ratio q/q_{TOT} is the fraction of total measured groundwater discharge at a given riverbed sampling point. The 41 values of age times q/q_{TOT} were ordered from youngest (shortest transit time) to oldest (longest transit time) and summed in sequence to determine the cumulative fraction of groundwater discharge younger than each sample (Kennedy et al. 2009; Gilmore et al. 2016).

5. Results

5.1. Water Chemistry: Streambed, Well, and Surface Water Samples.

Groundwater samples taken from below the streambed ranged in temperature from 7.4 to 21.4 ^{o}C, with an average value of 13.0 ^{o}C. These samples had pH close to neutral, with values ranging from 6.0 to 8.9 and an average of 7.2. Total dissolved inorganic carbon (DIC) ranged from 0.8 to 5.9 mmol/kg and averaged 1.9 mmol/kg (Tables 6 and 7). Groundwater was usually anoxic but dissolved oxygen concentrations spanned a wide range from 0.01 to 0.238 mM (0.3 to 7.6 mg/l). Bicarbonate was the dominant anion, and Ca or Na the dominant cation (Tables 6 - 9 and Figures 7 and 8). Si concentrations ranged from 0.4 to 1.4 mM and averaged 0.9 mM. For groundwater beneath the riverbed, the Piper diagram showed no apparent trend between major ion chemistry and distance along the channel (Figure 7). There was significant variability within each riverbed sampling area, though less at 99 km.

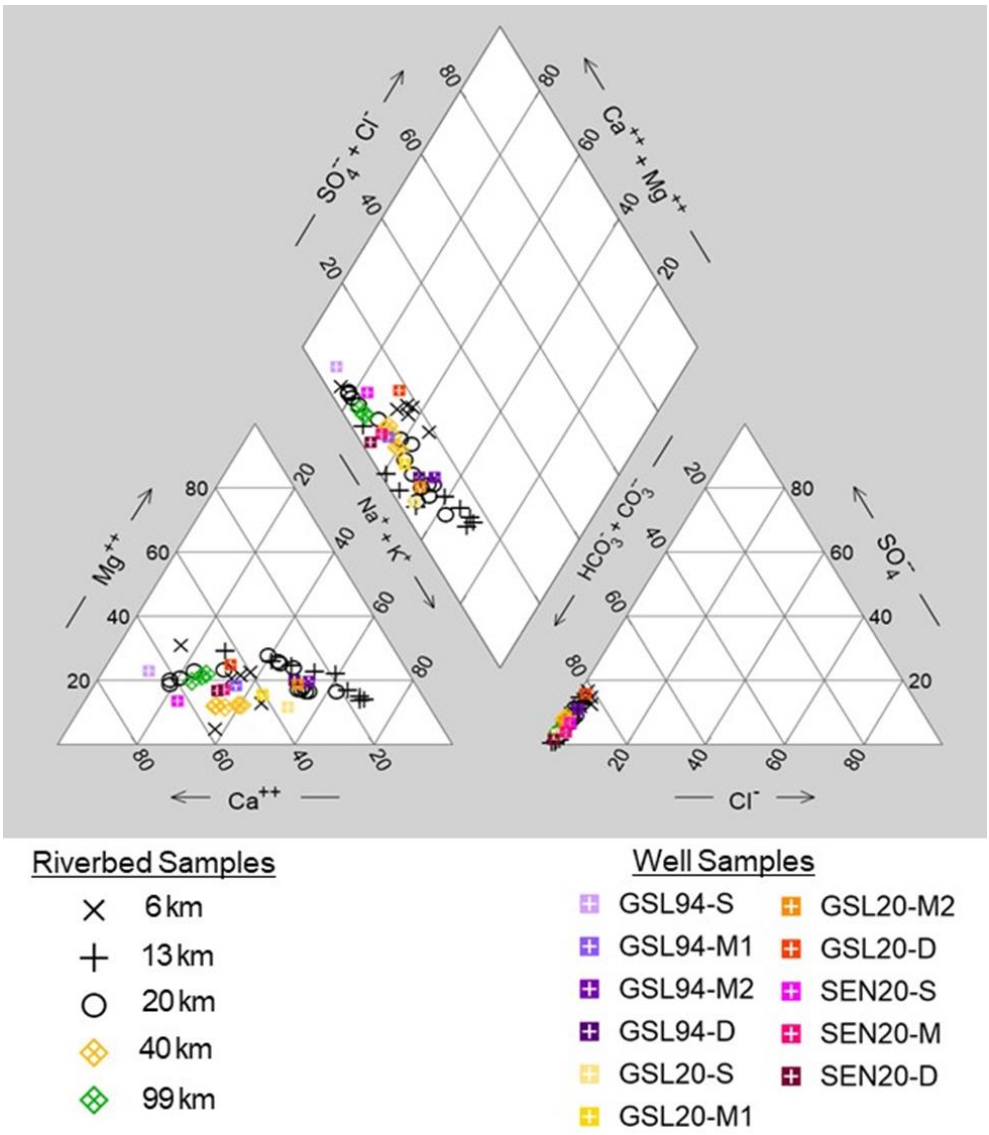

Figure 7. Piper diagram of groundwater samples collected in May 2019, and August or September 2020.

Table 6. Physical and chemical data for streambed groundwater samples analyzed for major ions from the 6, 13, and 20 km sampling areas. Data that were below the limit of quantification are shown in blue. *Calcite saturation index (SI) reported as log (IAP/K_{sp}).

Sample ID	Date	Temp (°C)	pH	SpC (µS/cm)	O_2 (µM)	DIC (µM)	Ca (µM)	Mg (µM)	Na (µM)	K (µM)	NO_3 (µM)	PO_4 (µM)	Cl (µM)	SO_4 (µM)	F (µM)	Si (µM)	$CaCO_3$ SI*
6400L06	5/28/2019	11.5	7.32	121	15.0	1160	209	95.0	217	93.9	0.00	1.99	30.7	81.7	27.8	618	-1.49
6400C00	5/28/2019	11.9	7.98	135	13.8	1180	241	74.1	212	311	1.08	3.39	29.3	123	11.9	353	-0.72
6400R06	5/28/2019	12.4	8.32	167	17.8	1400	395	34.6	150	362	0.00	1.76	31.6	121	3.53	608	-0.08
6590L06	5/28/2019	12.4	6.87	224	12.2	2550	415	244	115	134	0.00	7.49	44.3	24.9	7.16	1138	-1.39
6590C00	5/28/2019	12.6	7.19	123	12.8	1210	158	80.6	165	99.5	0.00	5.60	73.3	92.0	9.63	1000	-1.72
6590R06	5/28/2019	12.0	7.24	128	12.8	1230	154	88.5	188	102	0.00	4.50	54.7	113	13.2	959	-1.67
13235L30	5/27/2019	12.7	6.12	293	11.6	3910	553	376	276	441	0.00	2.58	66.0	23.1	19.4	789	-2.88
13235L20	5/27/2019	12.3	6.78	91.3	11.9	1000	66.4	62.1	249	229	0.00	5.06	25.7	73.1	14.6	827	-2.68
13235C00	5/27/2019	13.9	6.75	106	11.9	940	59.4	53.5	320	225	0.00	7.04	13.1	80.9	60.0	846	-2.76
13235R20	5/27/2019	15.5	6.61	116	11.6	1080	83.6	97.9	381	149	0.00	6.88	14.0	70.0	70.0	706	-2.72
13235R40	5/27/2019	14.7	5.99	117	12.2	1880	152	146	555	141	0.00	9.50	46.0	13.1	102.1	759	-3.22
13580L10	9/9/2020	13.7	8.27	102	107	860	48.2	39.7	217	188	30.5	5.98	22.0	56.1	0.80	829	-1.20
13580C00	9/9/2020	13.8	7.78	101	148	750	43.4	40.1	189	183	41.0	6.00	21.4	59.5	0.80	857	-1.80
13580R10	9/9/2020	15.2	6.95	258	10.9	3630	242	188	357	246	0.00	11.3	37.0	7.50	1.36	1238	-1.32
13580R20	9/9/2020	16.2	6.72	226	12.5	2900	178	153	452	139	0.00	11.2	51.3	5.41	169.0	1426	-1.81
20300L20	5/18/2019	11.4	6.93	374	10.9	3630	729	362	780	192	0.00	0.94	70.8	118	35.1	774	-0.76
20300L10	5/18/2019	11.6	6.95	486	10.0	5910	1263	527	925	175	0.00	2.17	78.4	118	25.1	787	-0.74
20300C00	5/18/2019	13.1	6.91	494	20.3	5920	1708	509	890	170	0.00	1.98	79.5	97.8	22.8	877	-0.43
20300R10	5/18/2019	14.1	6.86	484	11.9	5850	1359	472	790	177	0.00	1.70	83.8	97.1	28.2	927	-0.56
20300R20	5/18/2019	13.6	7.06	443	14.4	5510	1355	434	656	169	0.00	1.83	73.1	96.4	26.4	924	-0.34
20780L16	5/19/2019	13.5	8.90	116	125	850	75.6	42.0	163	122	0.00	4.74	26.8	42.1	32.6	1070	-0.28
20780L07	5/19/2019	13.3	8.06	107	153	1600	76.9	43.2	172	102	0.00	5.16	27.4	28.2	23.7	885	-1.11
20780R02	5/19/2019	13.3	7.38	108	170	1830	84.3	46.5	183	106	15.6	4.95	35.8	62.4	14.2	967	-1.74
20780R11	5/19/2019	12.1	7.08	101	238	1270	71.1	44.4	176	89.3	11.5	4.21	35.0	55.4	12.1	947	-2.16
20780R19	5/19/2019	12.1	7.14	95.2	87.5	1400	68.9	39.7	185	86.2	6.61	3.69	34.4	49.8	10.0	912	-2.07
20910L14	9/7/2020	18.2	8.14	143	64.7	1190	86.6	65.4	344	164	30.0	3.05	21.2	55.9	14.7	949	-1.28
20910L07	9/7/2020	18.4	7.90	146	11.3	1370	106	87.6	189	168	26.3	1.47	17.2	49.4	13.2	1077	-1.28
20910C00	9/7/2020	20.3	7.46	149	10.9	1870	129	105	194	161	0.00	2.42	33.3	116.6	37.4	974	-1.79
20910R08	9/7/2020	18.4	7.47	138	11.3	1660	126	105	176	125	0.00	4.00	33.8	80.5	28.4	910	-2.03
20910R15	9/7/2020	18.1	7.43	148	10.0	1620	119	94.6	185	150	0.00	5.58	31.9	56.6	28.4	1114	-1.35

Table 7. Physical and chemical data for streambed groundwater samples analyzed for major ions from the 40 and 99 km sampling areas. Data that were below the limit of quantification are shown in blue. *Calcite saturation index (SI) reported as log (IAP/Ksp).

Sample ID	Date	Temp (°C)	pH	SpC (µS/cm)	O_2 (µM)	DIC (µM)	Ca (µM)	Mg (µM)	Na (µM)	K (µM)	NO_3 (µM)	PO_4 (µM)	Cl (µM)	SO_4 (µM)	F (µM)	Si (µM)	$CaCO_3$ SI*
40670L20	8/3/2019	17.9	7.36	214	52.5	2210	419	106	579	141	1.32	1.12	18.3	92.3	19.9	729	-0.78
40670L10	8/3/2019	18.2	7.44	225	13.8	2330	459	116	613	146	0.66	0.95	19.5	94.0	17.3	952	-0.63
40670C00	8/3/2019	17.0	7.35	210	16.9	2190	459	102	513	142	1.03	0.98	19.6	95.5	16.5	756	-0.77
40670R10	8/3/2019	17.5	7.37	199	20.3	2080	437	99.2	424	136	1.02	0.90	17.6	86.8	12.0	667	-0.78
40670R20	8/3/2019	15.9	7.32	213	13.1	2240	497	109	478	147	0.53	0.76	22.6	103.8	12.2	739	-0.78
99090L99	5/24/2019	13.7	6.88	186	157	1960	363	146	183	175	30.5	0.00	29.9	38.0	9.11	1025	-1.51
99090L68	5/24/2019	13.9	6.88	177	64.1	1920	324	137	191	147	26.6	0.00	24.8	39.8	8.47	1074	-1.57
99100L99	5/23/2020	13.2	6.91	196	193	2040	421	147	198	165	31.3	0.00	25.3	36.5	9.32	960	-1.41

Table 8. Physical and chemical data for groundwater sampled from wells and analyzed for major ions. Sample ID corresponds to the University of Nebraska Conservation and Survey Division testhole ID system (https://snr.unl.edu/csd/geology/testholes.aspx). NA = Not Analyzed. Data that were below the limit of quantification are shown in blue. *Calcite saturation index (SI) reported as log (IAP/Ksp).

Well ID	Date	Temp (°C)	pH	SpC (µS/cm)	O_2 (µM)	DIC (µM)	Ca (µM)	Mg (µM)	Na (µM)	K (µM)	NO_3 (µM)	PO_4 (µM)	Cl (µM)	SO_4 (µM)	F (µM)	Si (µM)	$CaCO_3$ SI*
9-GSL-94S	8/11/2020	11.1	6.94	436	NA	5770	1345	465	291	199	0.00	0.00	118	104	52.1	832	-0.51
9-GSL-94M1	8/11/2020	9.78	7.07	301	NA	3690	818	325	1040	251	0.00	2.62	86.9	108	13.4	869	-0.77
9-GSL-94M2	8/11/2020	8.47	7.29	149	NA	1560	170	123	461	225	0.00	5.74	42.9	96.2	0.00	1044	-1.54
9-GSL-94D	8/11/2020	8.76	7.33	148	NA	1590	200	132	470	197	17.3	4.59	46.3	56.3	9.26	842	-1.41
01-GSL-2020S	12/8/2020	11.5	7.50	113	309	1310	198	63	405	180	10.7	1.48	21.9	33.5	6.95	NA	-1.27
01-GSL-2020M1	12/8/2020	11.5	7.48	111	280	1200	206	79	298	155	23.9	1.30	32.7	64.2	5.84	NA	-1.31
01-GSL-2020M2	12/8/2020	11.4	7.82	89.1	297	910	136	84	304	168	9.45	3.50	21.8	73.4	9.74	NA	-1.25
01-GSL-2020D	12/8/2020	13.6	7.75	239	21.9	2760	604	337	705	161	11.0	1.13	32.7	125	19.48	NA	-0.19
01-SEN-2020S	12/7/2020	13.0	7.80	196	293	2080	636	134	289	192	36.8	0.80	35.0	44.1	8.11	NA	-0.23
01-SEN-2020M	12/7/2020	13.4	7.30	141	9.38	1980	312	107	263	166	10.9	4.60	28.0	17.3	5.84	NA	-1.07
01-SEN-2020D	12/7/2020	14.0	7.34	145	17.8	1980	324	105	228	180	14.8	3.09	26.3	19.1	5.11	NA	-1.00
01-GSL-2003	4/26/2019	17.2	7.41	234	9.38	2040	NA	NA	NA	NA	NA	NA	NA	NA	NA	NA	NA

Table 9. Physical and chemical data for surface water samples. NA = Not Analyzed. Data that were below the limit of quantification are shown in blue. Calcite saturation index (SI) reported as log (IAP/K_{sp}).

Sample ID	Date	Temp (°C)	pH	SpC (µS/cm)	O_2 (µM)	DIC (µM)	Ca (µM)	Mg (µM)	Na (µM)	K (µM)	NO_3 (µM)	PO_4 (µM)	Cl (µM)	SO_4 (µM)	F (µM)	Si (µM)	$CaCO_3$ SI*
50	6/12/2019	11.6	NA	NA	NA	2770	523	259	466	158	1.10	3.45	43.7	50.3	18.6	862	NA
3500	6/12/2019	15.4	NA	NA	NA	2790	636	292	498	163	0.00	3.23	59.5	60.9	25.8	774	NA
7730	6/12/2019	12.7	NA	NA	NA	3450	840	378	980	229	0.82	1.68	110	96.8	38.7	674	NA
8960	6/12/2019	14.1	NA	NA	NA	3330	783	361	913	222	0.00	1.03	108	86.4	35.0	679	NA
16275	6/12/2019	15.0	NA	NA	NA	3450	763	355	883	224	0.00	1.04	105	85.0	37.8	684	NA
21300	6/12/2019	17.4	NA	NA	NA	3110	738	346	858	217	0.00	0.00	102	90.1	34.8	712	NA
39950	6/12/2019	12.5	NA	NA	NA	2870	621	310	744	202	0.00	0.82	84.1	79.2	29.9	769	NA
61200	6/12/2019	15.0	NA	NA	NA	4210	418	362	1705	662	0.00	0.00	178	84.4	39.4	806	NA
85000	6/12/2019	18.1	NA	NA	NA	3360	385	294	1244	513	2.81	0.00	131	85.6	28.8	869	NA
99050	6/12/2019	17.4	NA	NA	NA	3210	375	265	1400	446	0.00	0.00	118	86.2	27.2	909	NA
50	9/11/2020	10.9	7.74	266	234	2480	469	281	457	481	0.65	2.00	90.6	78.5	25.8	900	-0.46
7800	9/11/2020	12.3	8.02	279	269	2600	464	286	600	476	1.61	1.58	94.5	89.3	29.5	799	-0.04
8900	9/11/2020	12.5	8.01	261	274	2620	449	281	587	460	1.77	1.58	91.7	84.0	29.5	796	-0.06
20000	9/11/2020	12.8	7.91	280	275	2560	337	212	435	345	2.26	1.58	62.6	60.5	23.2	792	-0.16
40000	9/11/2020	12.8	8.02	226	259	2170	269	131	250	276	12.4	0.95	39.5	83.0	14.7	969	-0.24
99000	9/11/2020	12.9	7.90	198	257	1740	379	247	487	389	1.77	2.42	104	103	21.1	831	-0.55

The groundwater type was predominantly calcium-bicarbonate. Of the 49 groundwater samples analyzed for major ions, 32 were calcium-bicarbonate type, and 17 were sodium-bicarbonate type. The average compositions of streambed groundwater, well water, and surface water samples were all calcium-bicarbonate type (Figure 8). In samples analyzed for major ion concentration, charge imbalance (calculated in NETPATH) ranged from -20.8 to 3.6%, with negative numbers indicating a deficit of positive charge. This could be due to the combination of analytical uncertainty and charge deficit due to cationic species that were not analyzed such as iron, manganese, and other metals (Table 10, Figure 8).

All streambed groundwater samples and well water samples analyzed for major ions were undersaturated with respect to calcite (Tables 6 - 9). Calcite saturation index (SI) was calculated as log (IAP/K_{sp}); where IAP is the ion activity product, calculated using the Debye-Huckel equations (as presented in Morel and Hering (1993)) and K_{sp} is the temperature dependent solubility product constant for calcite (Plummer and Busenberg 1982). These results were consistent with SI values calculated in NETPATH. Negative calcite saturation indices (Tables 7-9) are consistent with the general lack of calcite observed in boreholes in the study area (section 2.4).

Dissolution of calcite in water that is in contact with gaseous CO_2 (reaction 2) produces one mole of Ca^{2+} for every two moles of DIC, based on the net stoichiometry of equation (reaction) 2 (reprinted below).

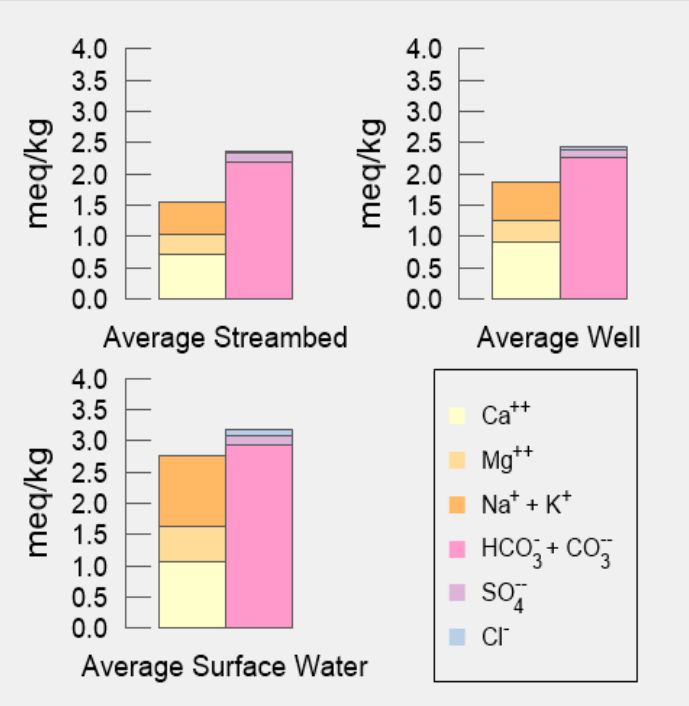

Figure 8. Ion balance for average streambed groundwater, well water, and surface water samples. Cation deficit is greatest in streambed groundwater and lowest in surface water.

Table 10. Average contribution of dissolved ions to groundwater charge balance.

Ion (% charge)	Average Streambed Groundwater	Average Well Water	Average Surface Water
Ca^{++}	18.3	20.7	17.7
Mg^{++}	7.6	8.2	9.7
Na^{+}	8.8	9.9	13.1
K^{+}	4.3	4.4	5.7
Cl^{-}	0.9	1.0	1.6
SO_4^{--}	3.6	3.1	2.7
HCO_3^{-}	55.4	52.0	48.9
F^{-}	0.6	0.3	0.5
NO_3^{--}	0.2	0.3	0.0
PO_4^{--}	0.2	0.1	0.0
Cations	39.0	43.2	46.2
Anions	61.0	56.8	53.8

If equation 2 were the only process contributing Ca^{2+} and DIC to the groundwater, the ratio of calcium to DIC would be 1:2. The data show that the ratio of Ca^{2+} to DIC in the groundwater is closer to 1:4 (Figure 9), suggesting equation 2 does not account for all DIC in the groundwater.

$$CaCO_3 + H_2O + CO_2 \rightarrow Ca^{2+} + 2HCO_3^- \quad (2)$$

Aerobic oxidation of organic matter, anaerobic nitrate or sulfate reduction, and bacterial methanogenesis contribute DIC to groundwater without contributing calcium (Cartwright 2010; Han et al. 2012), potentially lowering the Ca^{2+}/DIC ratio. Also, weathering of silicate minerals such as plagioclase above the water table, in contact with gaseous CO_2, would contribute DIC and calcium to the groundwater in a Ca^{2+}/DIC ratio close to 1:4. For example, above the water table where soil gas CO_2 would be the reactant carbon species, incongruent weathering of plagioclase (62% albite – 38% anorthite) would generate molar a Ca^{2+}/DIC ratio of 1/3.64 in groundwater (McMahon et al. 2007), close to that observed in both the present study (Fig. 9) and in the data of McMahon et al. in the High Plains Aquifer.

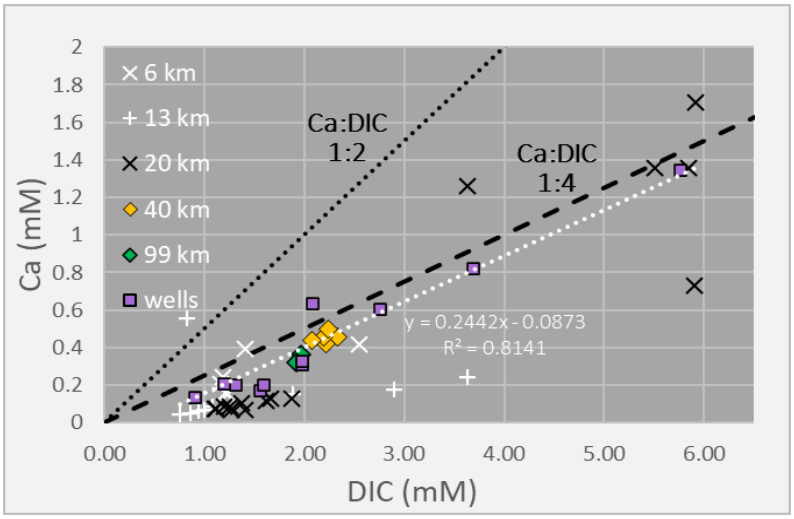

Figure 9. Ca vs DIC concentration in groundwater samples collected below the streambed and from wells. Samples indicate a Ca^{2+} to DIC ratio of about 1:4. A regression line of all groundwater samples is shown as a white dotted line.

Near the 6, 13, and 20 km sampling areas, measurable methane concentrations up to 2 µM were present in river water samples (Jensen 2021). Methanogenesis via microbially mediated acetate fermentation produces CO_2 and would lower the Ca^{2+}/DIC ratio of the groundwater. The river water has likely lost some methane to the atmosphere by gas exchange, but the amount of methane in groundwater would have to be on the order of 1000x greater than measured to indicate that the Ca^{2+}/DIC of groundwater was lowered by methanogenesis: CO_2 and methane are produced in roughly equal amounts by methanogenesis, and 2 µM is roughly 1000x lower than typical measured DIC concentrations in the groundwater (Fig. 9). It is not known whether methane (and CO_2 from methanogenesis) are locally higher than 2 µM in some groundwater, but the low methane concentrations observed in river water are not strong evidence that methanogenesis has lowered the groundwater Ca^{2+}/DIC. The more likely influence on groundwater Ca^{2+}/DIC is weathering reactions with minerals known to be present (such as calcite and plagioclase).

5.2. Tritium

All streambed groundwater samples were analyzed for tritium (^3H) content by our collaborators at the University of Utah. Beginning in the late 1950s, widespread atmospheric nuclear weapons testing caused the ^3H and ^{14}C content of precipitation to rapidly increase (McMahon et al. 2011). By 1953, ^3H concentrations in precipitation in Lincoln NE are estimated to have reached 20 tritium units (TU) (McMahon et al. 2011). In the 66 yr between 1953 and 2019, the ^3H content of precipitation from 1953

would have decayed to a concentration of 0.5 TU. Thus, groundwater samples collected in 2019 with greater than 0.5 TU or 100 pmc are likely younger than 66 yr, and those with less than 0.5 TU or 100 pmc are likely older than 66 yr.

Of the 59 samples from the 6, 13, and 20 km sampling areas, 43 had ^{3}H > 0.5 TU and/or $^{14}C_{DIC}$ > 100 pmc, suggesting that most (73 %) of the samples collected in these areas were too young to be effectively dated using $^{14}C_{DIC}$ (Tables 11 and 12). ^{14}C dating was focused on the samples from 40 and 99 km, and included a few samples from further upstream exhibiting relatively low ^{3}H and $^{14}C_{DIC}$ < 100 pmc (6590C00, 13235C00, 20300L20, 20300L10, 20300C00, 20300R10, 20300R20).

Table 11. C isotope and ^{3}H data for groundwater samples collected from below the riverbed at the 6, 13, and 20 km sampling areas. *Normalized $^{14}C_{DIC}$ reported by NOSAMS. "Error" column refers to the reported counting error in ^{14}C analysis by NOSAMS. **De-normalized $^{14}C_{DIC}$ in the year of sample collection (Mook and van der Plicht 1999). The "Reg." column refers to two regressions of $^{14}C_{DIC}$ vs. δ^{13}_{DIC} that are explained in section 5.3: "upper" and "lower" refer to the regression trend on which the sample falls, "excluded" indicates the sample did not plot near to, and was not used in, either regression. NA indicates samples for which ^{3}H was not successfully measured or was unavailable.

Sample	Date	$\delta^{13}C_{DIC}$ (‰)	$^{14}C_{DIC}$ (pMC)*	Error (pMC)	$^{14}C_{DIC}$ (pmc)**	^{3}H (TU)	Reg.
6300L05	5/28/2019	-10.77	75.4	0.15	77.0	0.87	Lower
6300C00	5/28/2019	-10.02	71.0	0.14	72.6	0.64	Lower
6300R05	5/28/2019	-9.29	66.2	0.18	67.7	0.21	Lower
6400L06	5/28/2019	-7.98	114.6	0.21	117.6	7.01	Excluded
6400C00	5/28/2019	-8.55	113.6	0.21	116.5	6.27	Excluded
6400R06	5/28/2019	-11.28	107.1	0.21	109.3	4.09	Upper
6590L06	5/28/2019	-9.83	89.3	0.18	91.3	6.69	Upper
6590C00	5/28/2019	-10.35	81.4	0.16	83.1	0.38	Lower
6590R06	5/28/2019	-9.22	73.1	0.15	74.9	0.08	Lower
13235L30	5/27/2019	-14.15	99.4	0.19	100.8	6.02	Lower
13235L20	5/27/2019	-12.11	90.6	0.18	92.2	NA	Lower
13235L10	5/27/2019	-12.01	91.9	0.18	93.6	7.96	Lower
13235C00	5/27/2019	-10.13	81.7	0.16	83.5	9.52	Lower
13235R10	5/27/2019	-8.17	85.0	0.17	87.2	10.37	Upper
13235R20	5/27/2019	-5.87	62.1	0.14	64.1	4.89	Upper
13235R30	5/27/2019	-6.87	74.7	0.15	76.8	3.73	Upper
13235R40	5/27/2019	-11.89	90.8	0.19	92.5	0.54	Lower
13580L20	5/20/2019	-14.62	103.4	0.21	107.9	10.62	Lower
13580L10	5/20/2019	-11.27	110.0	0.22	110.3	10.89	Upper
13580C00	5/20/2019	-11.78	101.2	0.21	111.7	11.75	Upper
13580R10	5/20/2019	-10.80	96.2	0.20	101.1	6.15	Upper
13580L10	9/09/2020	-11.23	106.6	0.21	105.4	NA	Upper
13580C00	9/09/2020	-10.49	108.1	0.24	112.3	NA	Upper
13580R10	9/09/2020	-0.79	109.6	0.21	105.4	NA	Excluded
13580R20	9/09/2020	-10.06	99.0	0.20	98.4	NA	Upper
13700L10	5/19/2019	-8.34	85.5	0.18	87.8	0.07	Upper
13700R02	5/19/2019	-11.20	87.0	0.17	88.8	0.06	Lower
13700R12	5/19/2019	-12.62	91.1	0.18	92.7	0.24	Lower
13700R22	5/19/2019	-10.03	100.6	0.20	102.9	8.31	Upper
20300L20	5/18/2019	-8.07	94.0	0.16	96.5	0.08	Upper
20300L10	5/18/2019	-9.26	94.8	0.16	97.1	0.08	Upper
20300C00	5/18/2019	-9.43	93.9	0.18	96.1	NA	Upper
20300R10	5/18/2019	-9.16	94.1	0.16	96.4	0.05	Upper
20300R20	5/18/2019	-9.78	93.8	0.22	95.9	0.06	Upper
20460L12	5/18/2019	-9.73	100.7	0.19	103.0	6.85	Upper
20460L04	5/18/2019	-9.20	70.9	0.27	72.6	2.35	Lower
20460R02	5/18/2019	-10.48	78.1	0.22	79.8	4.03	Lower
20460R10	5/18/2019	-8.54	70.0	0.19	71.8	0.27	Lower
20460R18	5/18/2019	-6.74	83.0	0.19	85.5	0.05	Upper
20780L16	5/19/2019	-7.58	102.0	0.20	104.8	7.25	Excluded
20780L07	5/19/2019	-9.89	101.6	0.23	103.9	5.65	Upper
20780R02	5/19/2019	-9.63	101.0	0.20	103.4	5.44	Upper
20780R11	5/19/2019	-11.61	104.4	0.29	106.4	5.16	Upper
20780R19	5/19/2019	-11.69	104.5	0.28	106.5	5.27	Upper
20780L16	9/08/2020	-9.71	106.1	0.22	108.6	NA	Upper
20780L07	9/08/2020	-9.67	105.9	0.22	108.3	NA	Upper
20780R02	9/08/2020	-9.61	105.5	0.22	108.0	NA	Upper
20780R11	9/08/2020	-9.35	105.9	0.30	108.5	NA	Upper
20780R19	9/08/2020	-11.32	105.5	0.21	107.6	NA	Upper
20910L07	5/18/2019	-14.00	97.3	0.28	98.7	4.25	Lower
20910C00	5/18/2019	-13.01	97.1	0.20	98.7	4.26	Lower
20910R08	5/18/2019	-14.11	101.7	0.21	103.2	5.47	Lower
20910R15	5/18/2019	-15.15	104.6	0.23	105.9	5.41	Lower
20910R21	5/18/2019	-13.81	104.0	0.20	105.5	2.91	Lower
20910L14	9/07/2020	-12.10	94.2	0.20	95.9	NA	Lower
20910L07	9/07/2020	-13.64	98.7	0.20	100.1	NA	Lower
20910C00	9/07/2020	-14.08	99.7	0.20	101.1	NA	Lower
20910R08	9/07/2020	-13.91	104.1	0.22	105.6	NA	Lower
20910R15	9/07/2020	-14.85	102.3	0.20	103.6	NA	Lower

Table 12. C isotope and ^{3}H data for groundwater samples collected from below the riverbed at the 40 and 99 km sampling areas. *Normalized $^{14}C_{DIC}$ reported by NOSAMS. "Error" column refers to the reported counting error in ^{14}C analysis by NOSAMS. **De-normalized $^{14}C_{DIC}$ in the year of sample collection (Mook and van der Plicht 1999). NA – Sample not collected.

Sample	Date	$\delta^{13}C_{DIC}$ (‰)	$^{14}C_{DIC}$ (pMC)*	Error (pMC)	$^{14}C_{DIC}$ (pmc)**	^{3}H (TU)
40500L24	08/02/2019	-8.18	66.7	0.17	68.5	0.06
40500L16	08/02/2019	-8.32	70.2	0.19	72.0	0.06
40500L08	08/02/2019	-8.29	61.0	0.16	62.6	0.08
40500C00	08/02/2019	-8.14	57.4	0.15	58.9	0.06
40500R08	08/02/2019	-8.24	62.9	0.22	64.5	0.05
40500R16	08/02/2019	-8.18	63.7	0.18	65.4	0.07
40553SIDE	08/02/2019	-7.92	70.1	0.15	72.0	0.09
40550L33	08/02/2019	-7.94	55.4	0.17	56.8	0.04
40550L25	08/02/2020	-8.05	56.1	0.17	57.5	0.06
40550L17	08/02/2019	-8.18	56.3	0.17	57.8	0.07
40550L09	08/02/2019	-8.18	55.0	0.16	56.4	0.08
40600L20	08/02/2019	-7.63	79.0	0.19	81.2	0.05
40600L10	08/02/2019	-7.63	78.5	0.22	80.7	0.06
40600C00	08/02/2019	-7.66	78.8	0.21	80.9	0.06
40600R10	08/02/2019	-7.52	79.2	0.18	81.4	0.07
40600R20	08/02/2019	-8.99	82.5	0.19	84.6	0.07
40670L20	08/03/2019	-7.94	56.3	0.16	57.8	0.03
40670L10	08/03/2019	-7.99	54.3	0.17	55.8	0.05
40670C00	08/03/2019	-8.08	55.8	0.16	57.3	0.00
40670R10	08/03/2019	-8.18	56.6	0.15	58.1	0.05
40670R20	08/03/2019	-8.12	54.3	0.16	55.8	0.07
99090L99	05/24/2019	-8.32	60.0	0.19	61.6	NA
99090L93	05/24/2019	-8.15	60.0	0.25	61.5	0.19
99090L68	05/24/2019	-8.33	52.6	0.17	54.0	0.22
99090L43	05/24/2019	-8.18	46.8	0.24	48.0	0.44
99090L18	05/24/2019	-7.89	36.6	0.14	37.6	NA
99090R08	05/24/2019	-7.98	31.2	0.13	32.0	0.05
99090R33	05/24/2019	-8.17	27.6	0.14	28.3	0.26
99090R58	05/24/2019	-8.08	28.5	0.13	29.2	2.20
99090R83	05/24/2019	-8.29	33.7	0.14	34.5	0.10
99090R99	05/24/2019	-8.90	50.8	0.16	52.1	0.16
99100L99	05/23/2019	-8.41	63.1	0.32	64.7	0.26
99100L85	05/23/2019	-8.18	59.4	0.20	61.0	0.12
99100L60	05/23/2019	-8.29	57.9	0.15	59.4	0.17
99100L35	05/23/2019	-8.03	51.5	0.16	52.8	0.10
99100L10	05/23/2019	-8.07	38.9	0.14	39.9	0.08
99100R15	05/23/2019	-8.08	38.0	0.13	39.0	0.06
99100R40	05/24/2019	-8.00	36.6	0.15	37.6	0.06
99100R65	05/24/2019	-8.05	31.1	0.16	32.0	0.12
99100R82	05/24/2019	-7.89	32.7	0.14	33.6	0.02
99100R99	05/24/2019	-8.13	33.6	0.18	34.5	0.06

5.3. Carbon isotopes: $^{14}C_{DIC}$ and δ^{13}_{DIC}

5.3.1 Overview

$^{14}C_{DIC}$ and δ^{13}_{DIC} varied widely among the groundwater samples. Two linear trends were observed in the $^{14}C_{DIC}$ and δ^{13}_{DIC} of samples from the 6, 13, and 20 km sampling areas (Figure 10). Best-fit lines to these linear trends are referred to here as the "lower regression" and "upper regression". Data from the 40 and 99 km sampling areas followed a different vertical trend on Figure 10, with $\delta^{13}C_{DIC} \approx$ -8‰ and $^{14}C_{DIC}$ between 28.3 and 80.9 pmc.

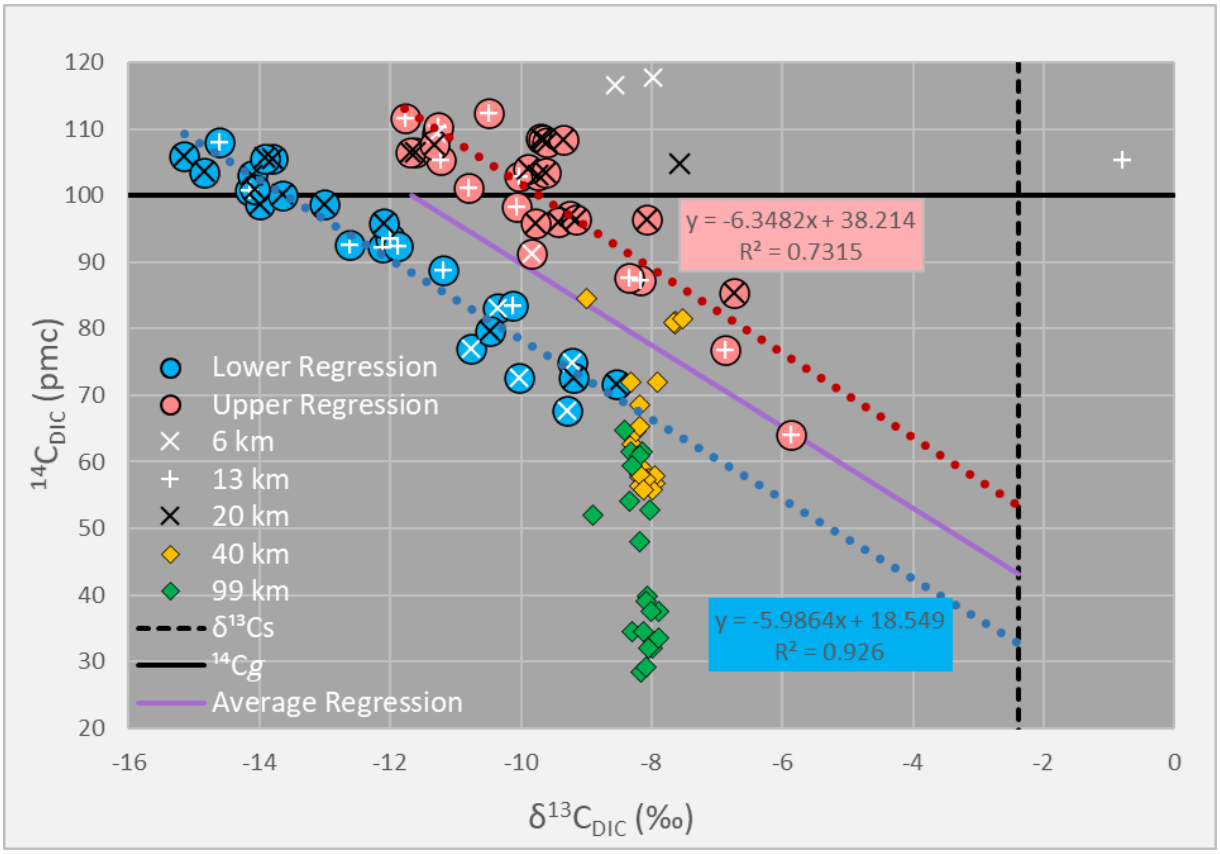

Figure 10. $^{14}C_{DIC}$ vs. $\delta^{13}C_{DIC}$ for groundwater samples collected below the riverbed.

Trends such as the upper and lower regressions have been interpreted in past work to indicate isotopic evolution of DIC from upper left to lower right as dissolution of carbonate minerals modifies DIC that was originally dominated by soil gas CO_2 in the upper left (Ingerson and Pearson 1964; Clark and Fritz 1997; Noseck et al. 2009; Han and Plummer 2016; Gardner et al. 2020). The upper and lower regressions may exhibit such a trend due to dissolution of calcite. These regressions were used to infer the C isotope content of DIC sources in groundwater discharging through the riverbed. There is also a suggestion of decreasing $^{14}C_{DIC}$ with increasing (Ca+Mg)/DIC, albeit with significant scatter (Figure 11), which would be consistent with reduction in $^{14}C_{DIC}$ by dissolution of carbonate minerals low in ^{14}C.

The two samples with the highest $^{14}C_{DIC}$, 6400L06 (117.6 pmc) and 6400C00 (116.5 pmc), were collected 100 m downstream of 6300R05 (67.7 pmc), a difference of about 50 pmc over a straight line distance of about 40 m across a meander. The maximum range in denormalized $^{14}C_{DIC}$ among samples collected across one transect during one sampling campaign was 36.7 pmc (transect 13235, May 2019), while the minimum was 0.97 pmc (transect 20780, September 2020). Apparently, some groundwater traveling along flowpaths to the upstream sampling areas undergoes geochemical reactions that

significantly lower $^{14}C_{DIC}$, while groundwater traveling along other flowpaths does not, with significant variation both within and among some streambed sampling transects. This seems consistent with the spatially variable and spotty occurrence of calcite in the porous medium, as mentioned regarding major ion results in section 5.1 and aquifer core lithology in section 2.1.

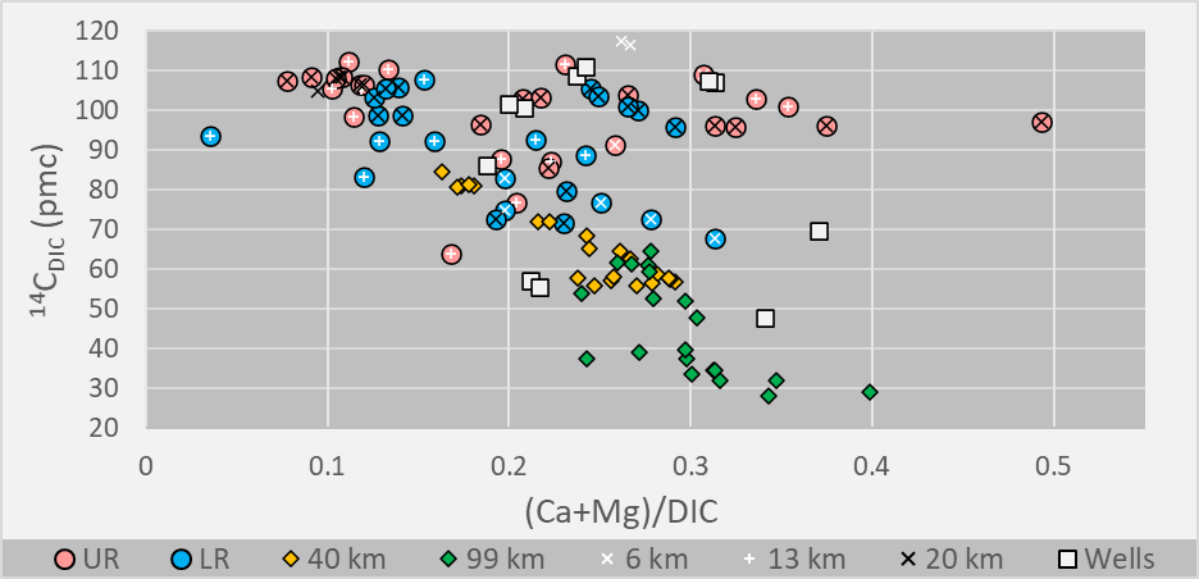

Figure 10. $^{14}C_{DIC}$ vs. $\delta_{13}C_{DIC}$ for groundwater samples collected below the riverbed.

At the 40 and 99 km sampling areas denormalized groundwater $^{14}C_{DIC}$ ranged from 28.3 to 84.6 pmc (Table 12); the average was 55.6 pmc, and the median was 57.5 pmc. $\delta^{13}C_{DIC}$ ranged from -9.0 to -7.52‰, with an average of -8.12‰ and a median of -8.13‰. While the range in $^{14}C_{DIC}$ among the upstream samples from 6, 13, and 20 km (53.6 pmc) was similar to the range for the downstream samples at 40 and 99 km (56.2 pmc), the range in $\delta^{13}C_{DIC}$ was much larger at the upstream sampling areas (14.36‰) than at the downstream sampling areas (1.47‰). Well samples (Table 13) had similar $\delta^{13}C_{DIC}$ to samples from the 40 and 99 km sampling areas but a much wider range in $^{14}C_{DIC}$.

Surface water samples exhibited similar but higher C isotope content than the groundwater discharging in the same area (Tables 13 and 14). At most sites surface water had $^{14}C_{DIC}$ between 80-100 pmc, reflecting that the stream water was not in isotopic equilibrium with the atmosphere. $\delta^{13}C_{DIC}$ values of surface water are higher than for groundwater samples but lower than atmospheric $\delta^{13}C$ which also is evidence that the samples had not reached equilibrium with the atmosphere. Only one sample was collected near the 99 km sampling area, which had $^{14}C_{DIC}$ = 64.1 pmc, much lower than surface water samples collected upstream of this site. This is consistent with a large discharge of groundwater low in ^{14}C upstream of the 99 km sampling area, at a rate sufficient to keep surface water in a state of isotopic disequilibrium with the atmosphere.

Table 13. C isotope data for groundwater samples collected from wells across the study area. *Normalized $^{14}C_{DIC}$ reported by NOSAMS. "Error" column refers to the reported counting error in ^{14}C analysis reported by NOSAMS. **De-normalized $^{14}C_{DIC}$ in the year of sample collection (Mook and van der Plicht 1999).

Well Samples	Date	$\delta^{13}C_{DIC}$ (‰)	$^{14}C_{DIC}$(pMC)*	Error (pMC)	$^{14}C_{DIC}$ (pmc)**
9-GSL-94S	8/11/2020	-8.76	104.7	0.22	107.3
9-GSL-94M1	8/11/2020	-6.12	104.4	0.23	107.6
9-GSL-94M2	8/11/2020	-7.05	83.7	0.20	86.1
9-GSL-94D	8/11/2020	-5.73	97.7	0.21	100.7
01-GSL-2020S	12/8/2020	-9.39	99.4	0.22	101.7
01-GSL-2020M1	12/7/2020	-8.41	106.2	0.27	108.9
01-GSL-2020M2	12/7/2020	-9.19	108.6	0.31	111.2
01-GSL-2020D	12/7/2020	-7.83	46.6	0.14	47.8
01-SEN-2020S	12/8/2020	-8.14	68.0	0.15	69.8
01-SEN-2020M	12/8/2020	-8.69	55.8	0.15	57.1
01-SEN-2020D	12/8/2020	-8.84	54.2	0.13	55.5
01-GSL-2003a	4/26/2019	-8.19	21.1	0.10	21.7
01-GSL-2003b	4/26/2019	-8.19	21.1	0.09	21.7

Table 14. C isotope and ^{3}H data for surface water samples collected in the study stream (Fig. 2). "Location" refers to distance downstream of the zero point measured in meters. *Normalized $^{14}C_{DIC}$ reported by NOSAMS. "Error" column refers to the reported counting error in ^{14}C analysis by NOSAMS. **De-normalized $^{14}C_{DIC}$ in the year of sample collection (Mook and van der Plicht 1999). NA – Sample not collected.

Location	Date	$\delta^{13}C_{DIC}$ (‰)	$^{14}C_{DIC}$ (pMC)*	Error (pMC)	$^{14}C_{DIC}$ (pmc)**	^{3}H (TU)
0	02/08/2019	-7.47	89.7	0.17	92.2	NA
7800	02/08/2019	-7.77	92.2	0.19	94.7	NA
7924	02/08/2019	-7.82	93.8	0.20	96.3	NA
21300	02/08/2019	-7.61	93.3	0.23	95.8	NA
39950	02/09/2019	-7.22	91.4	0.19	94.0	NA
84977	02/09/2019	-7.36	66.8	0.16	68.7	NA
50	06/12/2019	-10.16	88.9	0.21	90.9	0.611
3500	06/12/2019	-9.98	92.5	0.23	94.5	2.442
7730	06/12/2019	-9.38	98.2	0.21	100.5	5.690
8960	06/12/2019	-9.07	97.8	0.20	100.2	5.196
16275	06/12/2019	-8.98	97.7	0.20	100.1	5.143
21300	06/12/2019	-8.89	98.1	0.20	100.5	5.490
39950	06/12/2019	-9.06	96.1	0.20	98.5	4.550
61200	06/12/2019	-6.90	90.4	0.19	93.0	3.668
85000	06/12/2019	-7.31	85.8	0.20	88.2	2.961
99050	06/12/2019	-7.35	82.9	0.18	85.2	3.516
50	09/112020	-10.44	89.4	0.18	91.3	NA
7800	09/11/2020	-8.92	91.1	0.23	93.3	NA
8900	09/11/2020	-7.26	93.9	0.19	96.5	NA
20000	09/11/2020	-7.34	93.9	0.19	96.5	NA
40000	09/11/2020	-7.74	92.2	0.18	94.7	NA
99000	09/11/2020	-7.93	64.1	0.15	65.8	NA

5.3.2. C isotope regressions

Both single sample models and NETPATH modeling require values for the C isotope content of DIC sources in the aquifer. Given that no direct measurements of $\delta^{13}C_g$ or $^{14}C_s$ were available for our study site, published C isotope data for SOM and carbonates (Tables 1 and 2) and isotopic trends present in the new data (Figure 10) were used to determine values for these variables needed as inputs to the ^{14}C age modeling described in Section 4.2.

Given the evidence provided by tritium and $^{14}C_{DIC}$ data, the groundwater samples comprising the upper and lower regressions (Figure 10) are relatively young (≤ 100 yr), and the regressions may represent groundwater at progressive stages of chemical and isotopic evolution. Based on these assumptions, I used the two regressions to derive reasonable values for the C isotopic content of calcite and soil CO_2 (Table 15), to be used as input in the ^{14}C dating models.

In all simulations, $^{14}C_g$ was assumed to be 100 pmc (modern) and $\delta^{13}C_s$ was assumed to be -2.39‰ (an average from Table 2). To determine $\delta^{13}C_g$ input values for the age models, I found the $\delta^{13}C$ value at which each regression intersected 100 pmc (Figure 10): -13.61‰ for the lower regression, -9.73‰ for the upper regression, and -11.67‰ for "average regression" (Table 15), a line equidistant from the upper and lower regressions (Figure 10). These values are similar to the values implied by published $\delta^{13}C_{SOM}$ values (Table 1). Miao et al. (2007a) found that $\delta^{13}C_{SOM}$ was between -18.7 and -13.6‰ throughout the Holocene at their site in southwest Nebraska. The corresponding $\delta^{13}C_g$ values for these soils would be between -14.3 and -9.2‰, in close agreement with the range of $\delta^{13}C_g$ inferred from the regressions in Figure 10.

A similar method was used to determine values of $^{14}C_s$, the ^{14}C of carbonate mineral solids. I found the ^{14}C value at which each regression intersected $\delta^{13}C_{DIC}$ = -2.39‰: 32.86 pmc for the lower regression, 53.39 pmc for the upper regression, and 43.12 pmc for the average regression. The $^{14}C_{CH2O}$ values were assigned assuming that pedogenic carbonates were in isotopic equilibrium with the soil CO_2 and soil organic matter in which they formed, as often occurs in natural soils (Cerling et al. 1989; Cerling and Quade 1993). The cumulative effects of diffusive fractionation between SOM and CO_2 and mass fractionation between CO_2 and carbonate minerals (Section 2.4 & Table 5) impart a 3‰ enrichment on carbonates that are in isotopic equilibrium with soil CO_2 (and SOM) at 10°C. Thus, the $^{14}C_s$ values in Table 15 are enriched by 3‰ with respect to the associated $^{14}C_{CH2O}$ values.

Table 15. C isotope values of DIC sources used in groundwater age modeling. Values were derived from regression analysis and literature review (see text of section 5.3.1.).

	C isotope source	Lower Regression	Average Regression	Upper Regression	Literature Values
1	$^{14}C_g$ (pmc)	100	100	100	100
2	$\delta^{13}C_g$ (‰)	-13.61	-11.67	-9.73	-14.20
3	$^{14}C_s$ (pmc)	32.86	43.12	53.39	19.4
4	$\delta^{13}C_s$ (‰)	-2.39	-2.39	-2.39	-2.39
5	$\delta^{13}C_{CH2O}$ (‰)	-18.60	-18.60	-18.60	-18.60
6	$^{14}C_{CH2O}$ (pmc)	29.86	40.12	50.39	16.4

I also present modeling results for simulations that use the average $\delta^{13}C_g$ value implied by published data (Table 1), and the commonly assumed value of $^{14}C_s$ = 0 pmc (Table 15, last column). The $\delta^{13}C_g$ value of -14.20 for simulations labeled "Literature Values" or "LV" is based on the average subsurface $\delta^{13}C_{SOM}$ values reported in the sources shown in Table 1. The $^{14}C_{CH2O}$ value of 16.4 pmc is based on the maximum (oldest) age of soil organic matter reported in the literature for sites in the Sand Hills (14,500 yr) (Nicholson and Swinehart 2005).

While no studies reporting measured values of $^{14}C_s$ in Nebraska were found, several studies in New Mexico, Iowa, and Illinois (Chen and Polach 1986; Amundson et al. 1994; Deutz et al. 2000; Deutz et al. 2002; Plummer et al. 2004) demonstrate the occurrence of non-zero $^{14}C_s$ (5 – 90 pmc) in pedogenic

carbonates. Solder and Jurgens (2020) also inferred the presence of soil carbonates with $^{14}C_s$ as high as 90 pmc in southeastern NE, and greater than 90 pmc in northeastern Iowa and eastern South Dakota.

The conditions causing the two regressions (Fig. 10) are unknown, but the existence of two trends rather than one may be related to spatial or temporal differences in recharge conditions. No obvious relationships were observed between regression group and downstream distance or relative position across transects. Samples were relatively evenly distributed across the two regressions. The lower regression included 26 samples, while the upper regression had 29. Neither regression was consistently associated with the left (north) or right (south) side of the channel: the upper regression included 10 samples from left of center and 16 from right of center, while the lower regression included 9 from left of center and 12 from right of center. Also, the two regressions had similar proportions of samples from each sampling area: 19% of samples in the lower regression were from the 6 km sampling area, 31% were from the 13 km area, and 50% were from the 20 km area, while the corresponding percentages for the upper regression were 7, 38, and 55%, respectively.

In both regressions, samples plotting in the upper left have lower DIC concentrations and SpC values relative to other samples in the regression, another indication that they are chemically immature relative to other samples in the regression, which would be consistent with their C isotope signature being more similar to the soil gas and less affected by carbonate mineral dissolution. Further, the $^3H/^3He$ ages of the samples from 6, 13, and 20 km indicate that 38 of the 45 samples collected in May 2019 (84%) were younger than 75 yr, 5 of 45 samples (11%) were too old to be dated with $^3H/^3He$, and 2 of the 45 samples (4%) were not dated by $^3H/^3He$ due to errors in extraction or sampling. Of the 43 samples successfully dated using $^3H/^3He$, 88% were deemed younger than ~75 yr.

Between the upper and lower regression, the difference in $\delta^{13}C_{DIC}$ content at $^{14}C_{DIC}$ = 100 pmc (Table 15) is consistent with samples from the lower regression ($\delta^{13}C_g$ = -13.61‰) being recharged through soil less enriched in $\delta^{13}C_g$ relative to the upper regression ($\delta^{13}C_g$ = -9.73‰). In the eastern Sand Hills, Hartman 2015 found that the average $\delta^{13}C$ of plants growing on dune ridges was 7‰ greater than the average $\delta^{13}C$ of the C3 plants being cultivated in interdunal wetlands. He estimated that species composition was 69.2% C4 grasses on ungraded dune ridges, and 21.5% C4 grasses in interdunes. One possible explanation of the two regressions is that samples from the upper regression recharged in an area with a higher proportion of C4 plants such as on the dune ridges.

Another possible cause is temporal and/or spatial variability in soil respiration rate. Soil respiration rate is primarily dependent on soil temperature and moisture, with respiration rates increasing as soil temperature and moisture increase (Hartman 2015). At high soil respiration rates, $\delta^{13}C_g$ is enriched relative to SOM by 4.4‰. As soil respiration rate decreases, the enrichment increases until $\delta^{13}C_g$ approaches the $\delta^{13}C$ value of the atmosphere above the soil if respiration rate is very low (Cerling 1984; Cerling et al. 1991; Cerling 1991). The difference in $\delta^{13}C_g$ implied by the two regressions could be due, at least in part, to differences in soil respiration rates over time and space at the study site.

At the UNL Barta Brothers Ranch in the eastern Sand Hills, soil CO_2 flux was less than 0.5 µmol $m^{-2}s^{-1}$ in December and January, while the mean peak soil respiration was 3.26 µmol $m^{-2}s^{-1}$ in June (Hartman 2015). Dormant season (November – March) respiration accounted for only 8% of total annual soil CO_2 flux during his study. The contrast in soil respiration rates between the summer and winter months may contribute to the differences in $\delta^{13}C_{DIC}$ between the two regressions. Hartman also found that respiration rates vary with topography in the Sand Hills. Mean growing season soil respiration rate in interdunal wetlands (2.53 µmol $m^{-2}s^{-1}$) was significantly greater than on dune ridges (2.17 µmol m^{-2} s^{-1}), though this difference alone would not result in $\delta^{13}C_g$ values differing by the 3.88‰ that separates the two regressions. The seasonal and topographic variability in soil respiration rate, coupled with geographic variability of C3/C4 plant ratios, may be responsible for the two regressions. Water recharging through a soil zone with a higher proportion of C3 plants or increased soil respiration rates

would be depleted in $\delta^{13}C$ relative to samples that recharged through zones with a greater proportion of C4 plants and/or lower respiration rates. Consequently, the samples plotting in the lower regression may represent samples that recharged in conditions more like those found in the interdunes, and samples plotting in the upper regression may represent water that recharged in conditions more similar to those found on dune tops.

5.4. Groundwater Age Results

5.4.1. Determining reasonable $^{14}C_{REF}$ values

The minimum possible $^{14}C_{REF}$ value required to produce positive ages for all samples in a transect is the maximum $^{14}C_{DIC}$ value observed at a transect. These values helped to identify unreasonable model results. Only 3 of the 13 transects from the 6, 13, and 20 km sampling areas had minimum $^{14}C_{REF}$ values below 100 pmc, an indicator that samples from these transects are relatively young. This observation reinforces conclusions derived from riverbed groundwater ^{3}H concentrations that these transects primarily receive young groundwater discharge contaminated by anthropogenic "bomb" ^{14}C. Due to the nature of DIC being a mixture of carbon from multiple sources,, using anthropogenic $^{14}C_{DIC}$ as a dating method for young groundwater is usually unfeasible due to high levels of uncertainty in isotopic signatures of the many carbon sources encountered along a groundwater flowpath (Plummer and Glynn 2013).

Table 16. Minimum $^{14}C_{REF}$ value required to produce all positive ages at each transect. Only 3 transects from the 6, 13, and 20 km sample areas would produce positive ages if modeled using $^{14}C_{REF}$ = 100 pmc.

Transect	Minimum $^{14}C_{REF}$
6300	77.0
6400	117.6
6590	91.3
13235	100.8
13580	111.7
13580	112.3
13700	102.9
20300	97.1
20460	103.0
20780	106.5
20780	108.6
20910	105.9
20910	105.6
40500	72.0
40550	72.0
40600	84.6
40670	58.1
99090	61.6
99100	64.7

Another means I used to constrain values of $^{14}C_{REF}$ was determining a threshold number of unrealistic results allowable for each model. Unrealistic $^{14}C_{REF}$ values were those that resulted in negative ages, and those greater than 102 pmc (approximate maximum possible $^{14}C_{DIC}$ value under pre-modern atmospheric conditions) (Han and Plummer 2016). Model scenarios that produced more than 6 negative ages or more than 2 $^{14}C_{REF}$ values greater than 102 pmc, among the 41 samples from the 40 and 99 km sampling areas, were identified as unrealistic and eliminated from further consideration.

Of the samples from 40 and 99 km, those from transect 40600 consistently yielded negative ages across modeling scenarios, despite being too old for $^{3}H/^{3}He$ dating. Negative modeled ages are primarily due to these samples' high $^{14}C_{DIC}$ content, averaging 84.6 pmc (Table 16). Transect 40600 lies downgradient of a narrow meander neck, which initially suggested that mixing of river water and groundwater may have been the cause of the negative ages. Given that these samples have lower SpC and [DIC] than any surface water samples collected (Figure 12), they do not seem to be mixtures of river water and groundwater and may simply be the youngest groundwater samples collected from the 40 km sampling area.

Using the criteria outlined above, 22 of the 39 model scenarios were eliminated from consideration as unrealistic and 17 were not (Tables 17 and 18). All of those eliminated were scenarios based on single-sample models (not on NETPATH or the Tamers Mass Balance model). The abbreviation convention used throughout the text below gives the abbreviated model name first, followed by the abbreviated regression name, followed finally by whether the simulation had calcite with or without ^{14}C. For example, a simulation in which ages were computed in NETPATH (NP), using C source isotope values derived from the lower regression (LR), and calcite with ^{14}C (W) would have the abbreviation NP-LR-W. The NETPATH (NP), Tamers (T), and Tamers Mass Balance (TMB) models do not rely on $\delta^{13}C$ values of DIC sources to calculate sample age. As such, the upper, lower, average, and literature-derived simulations produced identical age results for the simulations assuming calcite without ^{14}C (WO). For this reason, the NETPATH, Tamers, and Tamers Mass Balance "WO" simulations do not include the middle abbreviation referring to a regression (LR, UR, or AR) or the literature values (LV) of $\delta^{13}C_g$.

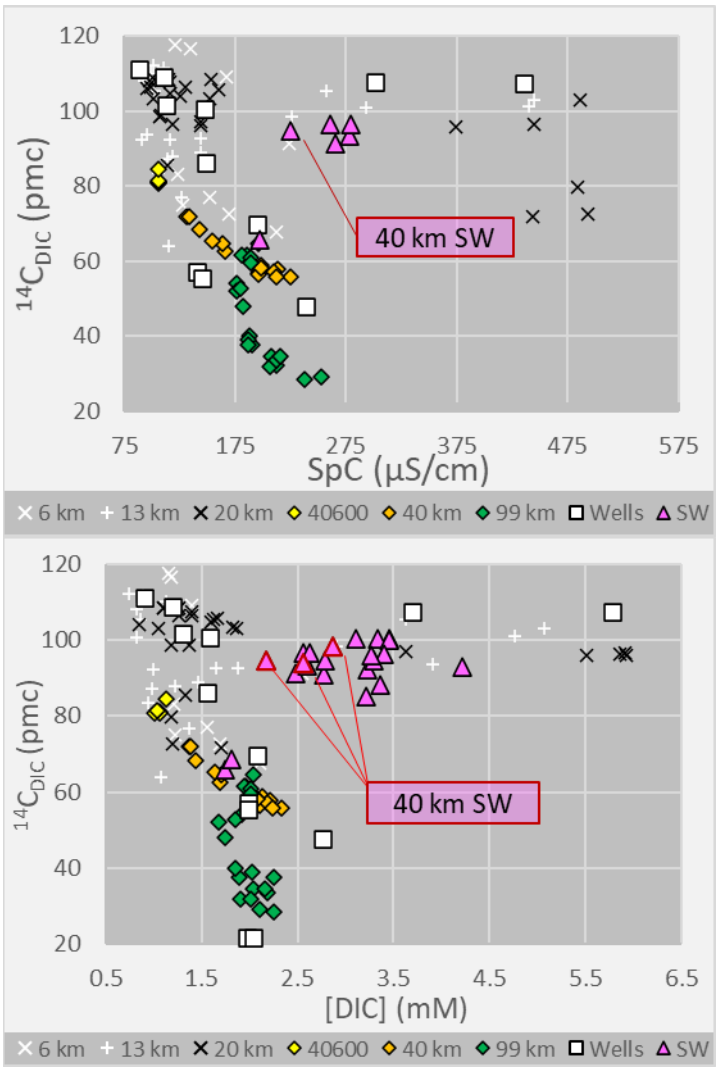

Figure 12. $^{14}C_{DIC}$ vs. SpC (top) and $^{14}C_{DIC}$ vs. DIC for groundwater and surface water (SW) samples. 6 surface water samples were analyzed for both SpC and $^{14}C_{DIC}$, while 22 were analyzed for both $^{14}C_{DIC}$ and [DIC].

Table 17. The 39 modeling scenarios considered. Scenarios shown in red were eliminated as unrealistic. Columns 2-5 refer to the approach for defining $\delta^{13}C_g$ and $^{14}C_s$ in the simulations as explained in the text: Lower Regression (LR), Average Regression (AR), Upper Regression (UR), and Literature Value (LV). WO = calcite without ^{14}C, W = calcite with ^{14}C.-- Modeled ages are identical across this row of the table.
* Rejected for producing 6 or more negative ages.** Rejected for producing more than 2 $^{14}C_{REF}$ values greater than 102 pmc.

Model	Lower	Average	Upper	Lit-Val
NETPATH, calcite with ^{14}C	NP-LR-W	NP-AR-W	NP-UR-W	NP-LV-W
NETPATH, calcite without ^{14}C	NP-WO	--	--	--
Tamers Mass Balance, calcite with ^{14}C	TMB-LR-W	TMB-AR-W	TMB-UR-W	TMB-LV-W
Tamers Mass Balance, calcite without ^{14}C	TMB-WO	--	--	--
Ingerson and Pearson, calcite with ^{14}C	I&P-LR-W *	I&P-AR-W	I&P-UR-W	I&P-LV-W *
Ingerson and Pearson, calcite without ^{14}C	I&P-LR-WO *	I&P-AR-W *	I&P-UR-W	I&P-LV-WO *
Han and Plummer, calcite with ^{14}C	H&P-LR-W	H&P-AR-W *	H&P-UR-W *	H&P-LV-W
Han & Plummer, calcite with ^{14}C	H&P-LR-WO *	H&P-AR-WO *	H&P-UR-WO *	H&P-LV-WO *
Tamers, calcite with ^{14}C	T-LR-W *	T-AR-W	T-UR-W	T-LV-W *
Tamers, calcite without ^{14}C	T-WO *	--	--	--
IAEA, calcite with ^{14}C	IAEA-LR-W **	IAEA-AR-W **	IAEA-UR-W **	IAEA-LV-W **
IAEA, calcite without ^{14}C	IAEA-LR-WO **	IAEA-AR-WO**	IAEA-UR-WO**	IAEA-LV-WO**

Table 18. Models not rejected using the criteria described in the text. All scenarios used 14Cg = 100 pmc and $\delta^{13}C_s$ = -2.39‰. The NETPATH, Tamers Mass Balance, and Tamers models are not affected by changes to δ13Cg. Only NETPATH used the value of 14CCH2O. "NA" (not applicable) indicates a value not needed or used in the model.

	Accepted Model Scenario	$\delta^{13}C_g$ (‰)	$^{14}C_s$ (pmc)	$^{14}C_{CH2O}$ (pmc)
1	NP-LR-W	NA	32.86	29.86
2	NP-AR-W	NA	43.12	40.12
3	NP-UR-W	NA	53.39	50.39
4	NP-LV-W	NA	19.40	16.40
5	NP-WO	NA	0	0
6	TMB-LR-W	NA	32.86	NA
7	TMB-AR-W	NA	43.12	NA
8	TMB-UR-W	NA	53.39	NA
9	TMB-LV-W	NA	19.40	NA
10	TMB-WO	NA	0	NA
11	I&P-AR-W	-11.67	43.12	NA
12	I&P-UR-W	-9.73	53.39	NA
13	I&P-UR-WO	-9.73	0	NA
14	H&P-LR-W	-13.61	32.86	NA
15	H&P-LV-W	-14.20	19.40	NA
16	T-AR-W	NA	43.12	NA
17	T-UR-W	NA	53.39	NA

5.4.2. NETPATH Modeling Results

All NETPATH simulations were performed using groundwater from well 9-GSL-94M2 as the initial water. Each groundwater sample collected from one of the 11 monitoring wells was tested as a potential "initial water" for NETPATH modeling. Each well sample was compared chemically and isotopically to the average groundwater composition of samples from the 40 and 99 km sampling areas, to see whether the 40 and 99 km averages could reasonably be generated from the well sample and a set of plausible mass transfers into groundwater in the aquifer. While NETPATH models and ages were attempted for 7 groundwater samples from the 6, 13, and 20 km sampling areas, the attempts were mostly not successful as shown below, and the focus of the dating was on the clearly older groundwater from 40 km and 99 km.

The 3 samples from the well nest near Seneca Nebraska (01-SEN-2020) were ruled out based on their location. The well nest is located only about 200 m northwest of the 99 km sampling area, far downgradient of the 40 km sampling area and much too close to the 99 km sampling area to serve as the site of initial water in NETPATH simulations.

Using wells 01-GSL-2020M1 and 01-GSL-2020M2 as initial waters to model average 40 km and 99 km groundwater samples would involve plausible chemical mass transfers (e.g., gains in SpC, Ca+Mg, and DIC), but the $^{14}C_{DIC}$ of these samples was greater than 100 pmc, indicating contamination with anthropogenic "bomb" carbon. The presence of bomb carbon contamination means these samples wouldn't show the $^{14}C_{DIC}$ content of uncontaminated pre-1950s initial water, disqualifying these samples from serving as the initial water in NETPATH. Also, the NETPATH models would involve a large mismatch between predicted and observed $\delta^{13}C_{DIC}$ at 99 km (between 3 and 5‰); mismatch at 40 km would be smaller but other wells (below) were useful as initial water for both 40 and 99 km. Using the deepest sample from this well nest (01-GSL-2020D) as initial water would require calcite precipitation and additional loss of DIC (beyond that lost through calcite precipitation) to achieve the C and Ca concentrations of the 40 and 99 km averages, which seems implausible.

The two shallowest wells from nest 9-GSL-94 were also rejected as candidates for initial water because they had higher concentrations of Ca and DIC (and all other major ions) than the average 40 and 99 km waters. Using them as initial waters would require calcite precipitation and additional loss of DIC beyond that subtracted due to calcite precipitation. Additionally, both were contaminated with bomb $^{14}C_{DIC}$.

Using the three remaining wells (9-GSL-94M2, 9-GSL-94D, and 01-GSL-2020S) as initial waters gave plausible chemical mass transfers to achieve average 40 and 99 km groundwaters. 01-GSL-2020S and 9-GSL-94D had $^{14}C_{DIC}$ of 101.7 and 100.7 respectively. While these values are higher than 100 pmc they are below the maximum $^{14}C_{DIC}$ value of DIC in isotopic equilibrium with $^{14}C_g$ = 100 pmc (approximately 102 pmc) (Mook 1972; Han and Plummer 2016). 01-GSL-2020S gave relatively large mismatch between the modeled and measured $\delta^{13}C_{DIC}$ making it a less suitable initial water.

9-GSL-94M2 had lower SpC, Ca, Mg, and DIC than the average composition of 40 and 99 km samples for which major ions had been analyzed, which is realistic for an initial water. It also had greater SO_4 and DO concentrations, which could serve as electron sources for microbial oxidation of organic matter, producing additional DIC beyond that generated through carbonate dissolution. Using 9-GSL-94M2 as initial water gave a relatively small mismatch between the modeled and measured $\delta^{13}C_{DIC}$ (about 1‰) and the well did not have the elevated ^{14}C associated with bomb carbon. The well is upgradient of all riverbed sampling points except for those at the 6 km sampling area. Groundwater from 9-GSL-94M2 was used as the initial water in all the NETPATH simulations reported here.

The model implemented in NETPATH determined the mass transfers occurring between the initial water and each final water as follows:

- Calcite mass transfers were calculated as [Ca] of the final water minus [Ca] of the initial water (0.017 mM in well 9-GSL-94M2).

- Positive calcite mass transfers reflecting dissolution of calcite add Ca and DIC to the initial water in a 1:1 ratio.
  - If the amount of DIC added through calcite mass transfer was not enough to account for the observed increase in DIC from initial to final water, then additional DIC was added through a positive mass transfer of CH_2O. This mass transfer reflects the microbial oxidation of organic matter.
  - If the amount of DIC added through calcite mass transfer was greater than the observed increase in DIC from initial to final water, the excess DIC was lost from the final water as a negative CO_2 mass transfer. This CO_2 mass transfer could reflect methanogenesis or diffusive loss of CO_2, but may simply indicate that well 9-GSL-94M2 does not accurately define initial water (at least for DIC) for the final water in question.
- Negative calcite mass transfers reflecting precipitation of calcite remove Ca and DIC in a 1:1 ratio from the initial water.
  - If the DIC subtracted from the initial water during calcite mass transfer resulted in a DIC concentration below that observed in the final water, additional DIC was added through a positive mass transfer of CH_2O.
  - If the DIC subtracted from the initial water during calcite mass transfer resulted in a DIC concentration above that observed in the final water, additional DIC was lost through a negative CO_2 mass transfer.

A subset of samples for which major ions had been measured were subjected to more comprehensive modeling in NETPATH prior to implementation of the model described above. Net mass transfer equations in NETPATH are solved using equation 9 (Plummer et al. 1994):

$$d\left(m_c\right) = \sum_{i=1}^{N} dI_i - \sum_{i=1}^{M} dO_i \qquad (9)$$

where m_c is the total concentration of an element (mmol/kg H_2O), *I* and *O* are the incoming and outgoing masses of that element per kg of H_2O through dissolution or precipitation of the i^{th} phase, and *N* and *M* are the total number of incoming and outgoing phases respectively. This simulation included constraints on C, Ca, Na, Si, K, Mg, and redox state, and included the phases shown in Table 19.

Table 19. Phases and stoichiometric coefficients of elements as they are added to (positive) or removed from (negative) solution through dissolution or precipitation of each phase in NETPATH modeling. "--" indicates the element is not included in the phase.

	Stoichiometric Coefficients							
Phase	Carbon (C)	Calcium (Ca)	Sodium (Na)	Potassium (K)	Magnesium (Mg)	Silica (Si)	Aluminum (Al)	Redox-State
Calcite	1	1	--	--	--	--	--	4
Lignite (CH_2O)	1	--	--	--	--	--	--	0
SiO_2	--	--	--	--	--	1	--	0
K-spar	--	--	--	1	--	3	1	0
K-mont	--	--	--	0.33	--	3.67	2.33	0
Ca-mont	--	0.16	--	--	--	3.67	2.33	0
Na-mont	--	--	0.33	--	--	3.67	2.33	0
Albite	--	--	1	--	--	3	1	0
Illite	--	--	--	0.6	0.25	3.5	2.3	0
Exchange Na:Ca	--	-1	2	--	--	--	--	0

Ages produced using this model were consistent with those produced by the simpler model applied to the full suite of groundwater samples. For example, using the more complex model with sample 99090L68 produced 68 possible simulation scenarios to achieve the chemistry of the final water using the input phases and constraints, 55 of which modeled age identically to the model using only C and Ca (2,139 years). The simpler model with fewer phases and constraints, which focused on C sources that could alter the $^{14}C_{DIC}$ of the groundwater, seemed sufficient for modeling the major reactions affecting groundwater $^{14}C_{DIC}$.

Of the 48 riverbed groundwater samples modeled with NETPATH, 41 exhibited calcite dissolution (positive calcite mass transfer into the initial water, Table 20). 33 of the 41 samples exhibiting calcite dissolution required additional C mass transfers in the form of organic matter oxidation (positive CH_2O mass transfer, Table 20), and 8 had a loss of DIC (as a negative CO_2 mass transfer). Seven samples, one each from 6 km and 13 km, and one 5-point transect at 40 km, had negative calcite mass transfers (calcite precipitation) even though all calcite SI values were negative (Tables 6 and 7)); this may imply that well 9-GSL-94M2 is not an ideal initial water for modeling these seven samples, and that they are possibly younger than the initial water sample.

Plummer et al. (1994) suggest comparing $\delta^{13}C_{DIC}$ values calculated in NETPATH to the values measured in the corresponding final water as a means to assess a model's performance. The average of the absolute values of the $\delta^{13}C_{DIC}$ differences (|measured – computed|) for the 48 groundwater samples (Table 20) was 1.66‰; the difference dropped to 0.88‰ when the less likely models with negative Ca or DIC mass transfer were excluded. This $\delta^{13}C_{DIC}$ mismatch is similar to or smaller than some other published values for NETPATH models. McMahon et al. (2007) had an average absolute $\delta^{13}C_{DIC}$ difference of 1.03‰ (n =11) from their modeling in the Sand Hills south of our study site. Plummer et al. (2004) used NETPATH in their characterization of groundwater flow in the Santa Fe Group aquifer, an unconfined aquifer much like the High Plains Aquifer in that it is comprised of unconsolidated to moderately consolidated "flood-plain, channel, and basin fill deposits" (p.15) containing secondary pedogenic carbonates with $^{14}C_s$ as high as 40 pmc. C4 plants are also the dominant species growing in the region. The average absolute $\delta^{13}C_{DIC}$ difference for their NETPATH models (n = 215) was 2.22‰. Kennedy and Genereux (2007) reported an average absolute $\delta^{13}C_{DIC}$ difference of 1.80‰ (n = 5) for their NETPATH models.

Table 20. Mass balance calculations performed with NETPATH for all samples dated using $^{14}C_{DIC}$. Well 9-GSL-94-M2 was used as initial water. Samples shown in bold were analyzed for major ion content; for those shown in normal typeface, Ca concentrations were estimated based on the relationship between Ca and SpC. *The three average values of "$\delta^{13}C$ mismatch" were calculated as the averages of the absolute values of the individual mismatches. *$\delta^{13}C$ Mismatch is the measured $\delta^{13}C$ minus the $\delta^{13}C$ simulated by NETPATH.

Final Water	Calcite Transfer	CH_2O Transfer	CO_2 Transfer	$\delta^{13}C_{DIC}$ Measured	$\delta^{13}C$ Calculated	$\delta^{13}C$ Mismatch	Final Water	Calcite Transfers	CH_2O Transfer	CO_2 Transfer	$\delta^{13}C_{DIC}$ Measured	$\delta^{13}C$ Calculated	$\delta^{13}C$ Mismatch
6590C00	**-0.01148**	**0**	**-0.33863**	**-10.35**	**-5.16**	**-5.19**	**40670R10**	**0.26703**	**0.25309**	**0**	**-8.18**	**-7.86**	**-0.32**
13235L20	**-0.11030**	**0**	**-0.50988**	**-10.13**	**-4.91**	**-5.22**	**40670R20**	**0.32693**	**0.35327**	**0**	**-8.12**	**-8.19**	**0.07**
20300L20	**0.55996**	**3.79256**	**0**	**-8.07**	**-11.35**	**3.28**	**99090L99**	**0.19341**	**0.20671**	**0**	**-8.32**	**-7.81**	**-0.51**
20300L10	**1.09351**	**0.97752**	**0**	**-9.26**	**-8.76**	**-0.50**	99090L93	0.20122	0.17874	0	-8.15	-7.63	-0.52
20300C00	**1.53906**	**2.82376**	**0**	**-9.43**	**-14.02**	**4.59**	**99090L68**	**0.15398**	**0.20612**	**0**	**-8.33**	**-7.92**	**-0.41**
2030010	**1.19005**	**3.10263**	**0**	**-9.16**	**-12.23**	**3.07**	99090L43	0.20737	0	-0.02747	-8.18	-6.40	-1.78
20300R20	**1.18602**	**2.76634**	**0**	**-9.78**	**-11.84**	**2.06**	99090L18	0.23373	0.09621	0	-7.89	-7.06	-0.83
40500L24	0.07277	0	-0.19293	-8.18	-5.77	-2.41	99090R08	0.30720	0.03275	0	-7.98	-6.50	-1.48
40500L16	0.03233	0	-0.22251	-8.32	-5.66	-2.66	99090R33	0.39197	0.29808	0	-8.17	-7.77	-0.40
40500L08	0.14934	0	-0.01945	-8.29	-6.55	-1.74	99090R58	0.44445	0.10558	0	-8.08	-6.65	-1.43
40500C00	0.26186	0.308150	0	-8.14	-8.15	0.01	99090R83	0.29116	0.18883	0	-8.29	-7.45	-0.84
40500R08	0.14450	0	-0.00461	-8.24	-6.63	-1.61	99090R99	0.18565	0	-0.06576	-8.90	-6.25	-2.65
40500R16	0.11134	0	-0.03146	-8.18	-6.58	-1.60	**99100L99**	**0.25106**	**0.22909**	**0**	**-8.41**	**-7.77**	**-0.64**
40553SW	0.04028	0	-0.22046	-7.92	-5.78	-2.14	99100L85	0.22897	0.22101	0	-8.18	-7.79	-0.39
40550L33	0.25414	0.20584	0	-7.94	-7.64	-0.30	99100L60	0.22995	0.22003	0	-8.29	-7.78	-0.51
40550L25	0.25550	0.23448	0	-8.05	-7.79	-0.26	99100L35	0.19929	0.09064	0	-8.03	-7.11	-0.92
40550L17	0.26328	0.26672	0	-8.18	-7.94	-0.24	99100L10	0.22368	0.06625	0	-8.07	-6.90	-1.17
40550L09	0.25313	0.29687	0	-8.18	-8.12	-0.06	99100R15	0.22328	0.23669	0	-8.08	-7.89	-0.19
40600L20	-0.05216	0	-0.44807	-7.63	-4.46	-3.17	99100R40	0.22143	0.46861	0	-8.00	-9.00	1.00
40600L10	-0.05405	0	-0.44618	-7.63	-4.20	-3.43	99100R65	0.28943	0.16055	0	-8.05	-7.30	-0.75
40600C00	-0.05344	0	-0.49679	-7.66	-3.83	-3.83	99100R82	0.30646	0.32357	0	-7.89	-8.10	0.21
40600R10	-0.05141	0	-0.46882	-7.52	-4.00	-3.52	99100R99	0.31972	0.28030	0	-8.13	-7.86	-0.27
40600R20	-0.05216	0	-0.37806	-8.99	-4.70	-4.29	40 km Avg*	0.14	0.15	-0.14	-8.06	-6.64	2.22
40670L20	**0.24957**	**0.40062**	**0**	**-7.94**	**-8.62**	**0.68**	99 km Avg*	0.26	0.18	0.00	-8.17	-7.45	0.84
40670L10	**0.28951**	**0.48076**	**0**	**-7.99**	**-8.85**	**0.86**	Average*	0.27	0.41	-0.09	-8.39	-7.39	1.66
40670C00	**0.28950**	**0.34068**	**0**	**-8.08**	**-8.23**	**0.15**							

5.4.3. Groundwater Age Results

Average age was much lower for samples from the 40 km sampling area than for samples from the 99 km sampling area, for both single sample and NETPATH modeling (Table 21). For the accepted simulations, average modeled age was 1,900 yr at the 40 km sampling area and 5,091 yr at the 99 km sampling area. For the 40 km sampling area, the TMB-UR-W scenario produced the greatest average age (2,822 yr) while the NP-WO scenario produced the smallest (917 yr). For the 99 km sampling area, the H&P-LV-WO scenario produced the greatest average age (6,228 yr), and the NP-WO scenario the smallest (3,719 yr) (Table 22). NETPATH and TMB were the only two models which produced acceptable results for scenarios with and without $^{14}C_s > 0$ pmc, and were also the only models that produced positive ages for all samples from 40 and 99 km (Table 22).

At transect 20300 there were only a few positive ages, all from I&P (Table 23); but for 6590C00 and 13235L20 there were positive NETPATH, Tamers Mass Balance, and I&P ages, that were mostly less than 1,000 yr. The low number of positive ages at 20300 is likely due to these samples having high $^{14}C_{DIC}$ content, elevated DIC concentrations, and/or error associated with C isotope input values.

Table 21. Average unadjusted age and average modeled age for the 17 accepted modeling scenarios, for each of the six transects in the 40 and 99 km sampling areas: 40500, 40550, 40600, 40670, 99090, and 99100. Sampling area averages are presented in the two columns furthest right.

	Average Age (yr) for Each Transect						Sampling Area Average Age (yr)	
Scenario	40500	40550	40600	40670	99090	99100	40 km	99 km
Unadjusted	3,537	4,245	1,667	4,656	7,147	6,796	3,527	6,972
NP-LR-W	1,788	1,896	477	1,706	4,809	4,237	1,482	4,523
NP-AR-W	1,885	2,094	477	2,054	5,030	4,503	1,640	4,766
NP-UR-W	1,987	2,348	477	2,442	5,259	4,795	1,822	5,027
NP-LV-W	1,638	1,549	477	1,224	4,497	3,874	1,242	4,185
NP-WO	1,436	1,105	477	545	4,076	3,362	917	3,719
TMB-LR-W	2,407	2,913	1,254	3,394	5,378	5,173	2,488	5,276
TMB-AR-W	2,591	3,132	1,319	3,600	5,675	5,443	2,657	5,559
TMB-UR-W	2,770	3,345	1,383	3,801	5,962	5,704	2,822	5,833
TMB-LV-W	2,160	2,617	1,168	3,116	4,971	4,805	2,260	4,888
TMB-WO	1,790	2,169	1,043	2,697	4,344	4,243	1,919	4,293
I&P-AR-W	1,577	2,175	-521	2,591	5,189	4,764	1,461	4,976
I&P-UR-W	2,707	3,316	633	3,731	6,319	5,901	2,602	6,110
I&P-UR-WO	1,640	2,102	-762	2,525	5,249	4,738	1,389	4,993
H&P-LR-W	1,079	2,469	-508	2,808	6,060	5,873	1,444	5,967
H&P-LV-WO	990	2,603	-517	2,908	6,308	6,147	1,472	6,228
T-UR-W	1,469	2,299	-412	2,699	5,474	5,152	1,512	5,313
T-AR-W	939	1,802	-945	2,199	5,054	4,741	996	4,898
Average	1,815	2,349	325	2,591	5,274	4,909	1,991	5,091

Table 22. ^{14}C age results for riverbed groundwater samples from the 40 and 99 km sampling areas. "Unadj." refers to the unadjusted ^{14}C age of the groundwater samples (age calculated assuming a reference activity of 100 pmc in the groundwater).

		NETPATH					Tamers Mass Balance					Ingerson and Pearson			Han and Plummer		Tamers	
Sample ID	**Unadj.**	NP-LR-W	NP-AR-W	NP-UR-W	NP-LV-W	NP-WO	TMB-LR-W	TMB-AR-W	TMB-UR-W	TMB-LV-W	TMB-WO	I&P-AR-W	I&P-UR-W	I&P-UR-WO	H&P-LR-W	H&P-LV-W	T-UR-W	T-AR-W
40500L24	3,133	1,667	1,715	1,763	1,604	1,512	2,123	2,285	2,445	1,904	1,579	1,144	2,277	1,173	583	457	1,033	494
40500L16	2,718	1,390	1,412	1,433	1,361	1,320	1,902	2,032	2,160	1,728	1,470	819	1,944	956	-146	-367	573	23
40500L08	3,869	2,171	2,262	2,352	2,050	1,873	2,630	2,832	3,029	2,357	1,948	1,950	3,077	2,064	1,376	1,270	1,812	1,284
40500C00	4,369	1,637	1,899	2,199	1,159	558	2,943	3,178	3,406	2,625	2,143	2,355	3,490	2,352	2,188	2,212	2,339	1,819
40500R08	3,620	1,938	2,025	2,112	1,821	1,650	2,414	2,610	2,802	2,149	1,751	1,670	2,799	1,745	1,293	1,236	1,593	1,074
40500R16	3,512	1,926	1,995	2,063	1,835	1,702	2,433	2,607	2,778	2,198	1,848	1,523	2,656	1,552	1,179	1,130	1,464	939
40553SW	2,716	1,359	1,386	1,413	1,324	1,272	1,858	1,995	2,130	1,674	1,402	559	1,709	377	972	1,124	738	232
40550L33	4,671	2,179	2,403	2,686	1,793	1,298	3,194	3,437	3,674	2,863	2,361	2,526	3,674	2,361	3,012	3,163	2,734	2,239
40550L25	4,569	2,010	2,245	2,546	1,599	1,075	3,109	3,350	3,584	2,783	2,288	2,496	3,638	2,422	2,752	2,869	2,613	2,114
40550L17	4,539	1,892	2,141	2,465	1,448	885	3,076	3,317	3,552	2,749	2,253	2,551	3,684	2,579	2,622	2,722	2,586	2,087
40550L09	4,732	2,042	2,296	2,633	1,579	999	3,328	3,559	3,783	3,015	2,542	2,743	3,876	2,772	2,989	3,139	2,823	2,338
40600L20	1,724	529	529	529	529	529	1,307	1,372	1,437	1,221	1,095	-627	541	-1,061	417	658	-197	-686
40600L10	1,773	583	583	583	583	583	1,371	1,434	1,496	1,287	1,166	-578	591	-1,012	-193	-139	-322	-861
40600C00	1,751	567	567	567	567	567	1,324	1,391	1,457	1,235	1,106	-580	587	-987	-236	-177	-349	-888
40600R10	1,702	516	516	516	516	516	1,272	1,339	1,406	1,182	1,052	-723	453	-1,258	-274	-211	-434	-982
40600R20	1,387	189	189	189	189	189	997	1,058	1,119	916	799	-95	990	510	-2,252	-2,716	-759	-1,309
40670L20	4,527	1,567	1,917	2,311	1,085	411	3,362	3,552	3,737	3,107	2,726	2,383	3,531	2,218	2,823	2,972	2,571	2,072
40670L10	4,827	1,626	2,029	2,482	1,065	274	3,594	3,795	3,991	3,323	2,916	2,716	3,861	2,592	2,931	3,033	2,831	2,320
40670C00	4,608	1,697	2,037	2,414	1,229	567	3,334	3,542	3,745	3,053	2,631	2,555	3,694	2,504	2,769	2,868	2,660	2,163
40670R10	4,490	1,824	2,111	2,429	1,430	875	3,197	3,408	3,615	2,911	2,481	2,502	3,635	2,531	2,520	2,589	2,531	2,030
40670R20	4,826	1,814	2,177	2,576	1,313	598	3,481	3,701	3,916	3,183	2,733	2,799	3,936	2,780	2,996	3,080	2,900	2,409
99090L99	4,010	1,624	1,852	2,107	1,315	887	2,558	2,797	3,030	2,233	1,741	2,112	3,237	2,249	3,235	3,559	2,450	2,063
99090L93	4,013	1,679	1,897	2,138	1,385	975	2,522	2,768	3,007	2,187	1,679	2,006	3,141	2,011	3,591	4,006	2,510	2,139
99090L68	5,092	2,802	3,009	3,245	2,522	2,139	3,779	3,994	4,203	3,488	3,050	3,200	4,324	3,344	4,311	4,636	3,530	3,143
99090L43	6,071	4,209	4,333	4,456	4,010	3,796	4,356	4,643	4,920	3,965	3,366	4,083	5,216	4,112	5,727	6,151	4,607	4,246
99090L18	8,083	5,885	6,076	6,263	5,628	5,260	6,390	6,673	6,946	6,005	5,415	5,905	7,057	5,698	7,640	8,040	6,521	6,134
99090R08	9,418	7,207	7,402	7,594	6,942	6,552	7,372	7,720	8,053	6,893	6,149	7,300	8,445	7,168	8,096	8,292	7,611	7,155
99090R33	10,427	7,406	7,773	8,124	6,899	6,164	8,379	8,727	9,061	7,899	7,155	8,433	9,567	8,454	8,941	9,093	8,621	8,164

Table 22. (continued)

99090R58	10,169	7,463	7,764	8,071	7,050	6,436	7,718	8,143	8,548	7,125	6,187	8,116	9,256	8,066	8,779	8,978	8,354	7,895
99090R83	8,791	6,224	6,492	6,781	5,859	5,337	6,976	7,281	7,575	6,559	5,917	6,874	8,000	6,987	7,019	7,097	6,934	6,462
99090R99	5,396	3,590	3,704	3,816	3,361	3,215	3,733	4,010	4,278	3,355	2,778	3,858	4,949	4,404	3,265	3,222	3,598	3,144
99100L99	3,597	1,022	1,290	1,586	657	142	2,010	2,273	2,529	1,651	1,105	1,755	2,874	1,959	2,643	2,917	2,010	1,616
99100L85	4,087	1,581	1,834	2,115	1,237	755	2,528	2,786	3,037	2,176	1,642	2,098	3,231	2,127	4,369	4,918	2,831	2,526
99100L60	4,310	1,805	2,058	2,339	1,461	979	2,747	3,006	3,257	2,394	1,857	2,392	3,519	2,506	4,068	4,513	2,905	2,560
99100L35	5,275	3,180	3,350	3,531	2,952	2,629	3,713	3,972	4,223	3,360	2,825	3,190	4,332	3,099	4,852	5,246	3,764	3,390
99100L10	7,597	5,505	5,675	5,852	5,278	4,950	5,914	6,195	6,467	5,531	4,946	5,537	6,677	5,478	7,106	7,480	6,078	5,702
99100R15	7,774	5,244	5,502	5,790	4,892	4,402	6,248	6,501	6,746	5,905	5,384	5,721	6,860	5,671	6,820	7,097	6,106	5,689
99100R40	8,084	5,036	5,404	5,824	4,527	3,821	6,736	6,957	7,173	6,437	5,986	5,980	7,124	5,864	6,663	6,828	6,258	5,795
99100R65	9,430	6,936	7,189	7,460	6,592	6,099	7,593	7,902	8,200	7,170	6,519	7,358	8,500	7,284	7,805	7,927	7,552	7,074
99100R82	9,011	6,102	6,442	6,816	5,634	4,969	7,269	7,561	7,842	6,871	6,261	6,832	7,984	6,625	7,370	7,462	7,104	6,619
99100R99	8,795	5,956	6,282	6,638	5,509	4,870	6,970	7,276	7,572	6,549	5,903	6,775	7,912	6,765	7,033	7,086	6,916	6,439

Table 23. ^{14}C age results for riverbed groundwater samples thought to be older than 75 yr, based on $^{3}H/^{3}He$ age dating, from the 6, 13, and 20 km sampling areas.

		NETPATH					Tamers Mass Balance					Ingerson and Pearson			Han and Plummer		Tamers	
Sample ID	**Unadj.**	NP-LR-W	NP-AR-W	NP-UR-W	NP-LV-W	NP-WO	TMB-LR-W	TMB-AR-W	TMB-UR-W	TMB-LV-W	TMB-WO	I&P-AR-W	I&P-UR-W	I&P-UR-WO	H&P-LR-W	H&P-LV-W	T-UR-W	T-AR-W
6590C00	1,528	322	322	322	322	322	826	938	1,048	678	460	831	1,848	2,199	-2,144	-2,689	-294	-755
13235L20	669	-536	-536	-536	-536	-536	356	405	453	292	198	890	1833	2991	-3,084	-3,649	-768	-1121
20300L20	296	-6,306	-5,024	-3,912	-8,364	-11,951	-672	-516	-363	-881	-1,191	-1,764	-624	-1,822	-477	-186	-1,293	-1,688
20300L10	246	-4,706	-3,869	-3,109	-5,951	-7,972	-2,813	-2,266	-1,752	-3,591	-4,859	-1,075	-4	-300	-1,529	-1,485	-1,365	-1,766
20300C00	331	-6,185	-4,914	-3,812	-8,221	-11,930	-1,941	-1,551	-1,177	-2,483	-3,332	-889	172	-14	-1,468	-1,409	-1,254	-1,648
20300R10	307	-6,208	-4,942	-3,843	-8,233	-11,855	-1,526	-1,218	-921	-1,949	-2,598	-1,073	3	-360	-1,080	-898	-1,235	-1,617
20300R20	344	-5,998	-4,782	-3,722	-7,926	-11,324	-1,565	-1,243	-933	-2,007	-2,689	-673	371	400	-2,346	-2,543	-1,384	-1,819

When using NETPATH to determine the total age of groundwater samples, the age of the initial water must also be estimated because the age of the final water is the age difference from the NETPATH simulation plus the age of the initial water. The TMB model is the only single sample model of those used in this study that produced reasonable age results for the initial water under all assumptions about the C isotopic compositions of calcite and soil CO_2 (Table 24). The H&P-LR-W, H&P-LV-W, and H&P-LV-WO simulations also resulted in positive ages (Table 24). The average of the 8 TMB calculations for 9-GSL-94M2 is 205 yr. Thus, the total age for NETPATH scenarios would be about 205 yr greater than the values shown in Tables 22 and 23. Increasing all NETPATH ages by 205 yr would increase the average age at the 40 and 99 km sampling areas by 12.6 and 4.4% respectively.

Table 24. Estimated age (yr) of NETPATH "initial water" (groundwater from well 9-GSL-94M2) using four single sample models.

Model	Tamers Mass Balance	Ingerson & Pearson	Han & Plummer	Tamers
Lower regression, calcite with ^{14}C (LR-W)	268	-2884	212	-1,755
Lower regression, calcite without ^{14}C (LR-WO)	123	-6027	-382	-3,453
Average regression, calcite with ^{14}C (AR-W)	313	-1515	-423	-1,100
Average regression, calcite without ^{14}C (AR-WO)	123	-4457	-1974	-3,453
Upper regression, calcite with ^{14}C (UR-W)	358	-305	-591	-762
Upper regression, calcite without ^{14}C (UR-WO)	123	-2519	-3324	-3,453
Literature Values, calcite with ^{14}C (LV-W)	209	-4296	608	-2,311
Literature Values, calcite without ^{14}C (LV-WO)	123	-6450	424	-3,453

5.4.4. Flow Weighted Mean Transit Times and Groundwater Transit Time Distributions

Flow weighted cumulative groundwater TTDs constructed using seepage flux measurements and modeled ^{14}C groundwater ages from 2019 indicate that at least 77% of groundwater discharging into the Middle Loup River at sampling locations in this study was greater than ~75 yr old, while only 23% was younger than 75 yr. Groundwater seepage flux across the 5 sampling areas ranged from -0.23 (6300C00) to 2.13 m/d (99090L99) for samples collected in 2019, with an average of 0.32 m/d. High streamflow conditions during sampling prevented collection of seepage data from 7 of the 20 points at the 99 km sampling area (Table 25). Ages from these points were included in TTDs, and assigned q values equal to the average value of successful seepage flux measurements from the 99 km sampling area (1.00 m/d). Groundwater seepage was highest at the 99 km sampling areas, and it is therefore unlikely that these points had negative seepage values.

Average ^{14}C ages were calculated for the 41 samples from the 40 and 99 km sampling areas, and the five samples from further upstream that were thought (by University of Utah collaborators) to be too old for successful $^{3}H/^{3}He$ dating (Table 25 and Figure 13). The average ^{14}C ages of these samples, based on the 17 accepted scenarios and excluding negative ages from the averaging, ranged from 3 to 8,168 yr; groundwater seepage rate (specific discharge) at these 46 sampling points was 0 to 2.13 m/day. Flow weighted mean transit times (MTT), calculated as $MTT = \Sigma q \cdot \tau / \Sigma q$ (Gilmore et al. 2016), were 1,944 and 5,029 yr for the 40 and 99 km sampling areas respectively and 3,383 yr for all samples in Table 25. These MTTs apply to "average" transit time distributions (TTDs) in which the age at each sampling point was taken to be the average of all the positive ages at that point from the 17 accepted modeling scenarios in Table 18 (Figure 13). The 41 samples collected at the 40 and 99 km sampling areas had a combined MTT of 4,494 yr

Table 25 Groundwater seepage rate (q), average age, and standard deviation (SD) in age for samples dated using $^{14}C_{DIC}$. Notes: A = no acceptable ^{14}C ages for these two samples, B = measured q was downward from channel to groundwater and the uncertainty in q was greater than the magnitude of the measured q, C = the q measurement was unsuccessful due to high flow in the river and the average q at 99 km was used for these points, n = number of ages used in calculation of the average age and SD, NA = not available (no age, or no standard deviation because n=1).

Sample ID	seepage q (m/day)	Average Age (yr)	Standard Deviation (yr)	Age + SD (yr)	Age – SD (yr)	n
6590C00	0.31	581	274	855	307	11
13235L20	0.15	432	220	653	212	6
20300L20[A]	0.55	NA	NA	NA	NA	0
20300L10[A]	0.15	NA	NA	NA	NA	0
20300C00	0[B]	172	NA	NA	NA	1
20300R10	0.78	3	NA	NA	NA	1
20300R20	0[B]	386	15	400	371	2
40500L24	0.01	1,515	605	2,120	911	17
40500L16	0.01	1,368	562	1,931	806	15
40500L08	0.01	2,138	533	2,671	1,604	17
40500C00	0.04	2,265	733	2,998	1,532	17
40500R08	0.33	1,923	501	2,423	1,422	17
40500R16	0.15	1,872	530	2,402	1,342	17
40553SW	0.04	1,266	532	1,798	735	17
40550L33	0.27	2,682	625	3,307	2,057	17
40550L25	0.75	2,558	648	3,207	1,910	17
40550L17	0.04	2,506	690	3,197	1,816	17
40550L09	0.02	2,733	727	3,459	2,006	17
40600L20	0.34	823	377	1,200	445	13
40600L10	0.31	933	390	1,322	543	11
40600C00	0.16	903	374	1,277	529	11
40600R10	0.22	844	380	1,224	464	11
40600R20	0.25	611	385	996	226	12
40670L20	0.30	2,491	877	3,368	1,614	17
40670L10	0.22	2,669	970	3,639	1,700	17
40670C00	0.45	2,557	826	3,383	1,731	17
40670R10	0.06	2,507	713	3,220	1,794	17
40670R20	0.20	2,729	862	3,591	1,867	17
99090L99	2.13	2,297	698	2,995	1,599	17
99090L93	0.72	2,332	761	3,093	1,571	17
99090L68	1.12	3,454	662	4,116	2,792	17
99090L43	1.26	4,482	676	5,159	3,806	17
99090L18	0.76	6,326	734	7,060	5,591	17
99090R08	1.00[C]	7,409	589	7,998	6,820	17
99090R33	1.26	8,168	854	9,022	7,315	17
99090R58	1.00[C]	7,879	812	8,691	7,068	17
99090R83	0.79	6,728	633	7,361	6,095	17
99090R99	0.28	3,664	519	4,182	3,145	17
99100L99	1.00[C]	1,767	746	2,513	1,021	17
99100L85	1.00[C]	2,458	1,016	3,474	1,442	17
99100L60	0.87	2,610	872	3,482	1,737	17
99100L35	0.96	3,624	690	4,314	2,934	17
99100L10	1.21	5,904	681	6,585	5,223	17
99100R15	0.59	5,916	715	6,631	5,201	17
99100R40	1.00[C]	6,024	900	6,924	5,124	17
99100R65	1.00[C]	7,362	601	7,963	6,761	17
99100R82	1.03	6,810	760	7,570	6,049	17
99100R99	1.00[C]	6,615	730	7,345	5,885	17

The 17 accepted modeling scenarios produce TTDs that are mostly concave downward to nearly linear in shape, with some concave-up areas, e.g., around 2,000 yr (Figure 14). To test which lumped parameter model (LPM) fit the entire suite of sample ages best, I used the $^{3}H/^{3}He$ ages calculated for the younger samples by our collaborators at the University of Utah and the average ages of the older samples (Table 24) to compile a cumulative TTD for the groundwater samples from each sampling area (Figure 15). A gamma distribution and an exponential distribution were fit to the data using the "solver" add-in in Microsoft Excel®, minimizing the sum of squared residuals for each distribution (Figure 16). The exponential distribution was constrained by limiting the rate parameter (λ, yr^{-1}) to values between 0 and 1. Mean transit time for the exponential model is equivalent to $1/\lambda$ (Haitjema 1995; Abrams and Haitjema 2018), consequently the MTT of the exponential distribution was only constrained to be ≥1 yr. The gamma distribution was constrained by allowing the shape factor (α, dimensionless) to vary between 0 and 10, and allowing the rate parameter (β, yr) to vary between 0 and 15,000. For the gamma distribution, MTT = $\alpha \cdot \beta$ (Abrams and Haitjema 2018). Consequently, the MTT for the gamma distribution was constrained between values of 0 and 15,000 yr.

The best-fit exponential distribution yielded MTT = 3,696 yr (λ = 0.000271 yr^{-1}) (Figure 16). The sum of squared residuals for the exponential model was 0.93. The best-fit gamma distribution yielded MTT = 5,158 yr, with α = 0.431 and β = 12,912 yr. The sum of squared residuals for the gamma model was 0.656. The gamma distribution appeared to fit better to young groundwater samples than it did older ones, while the opposite was true for the exponential distribution.

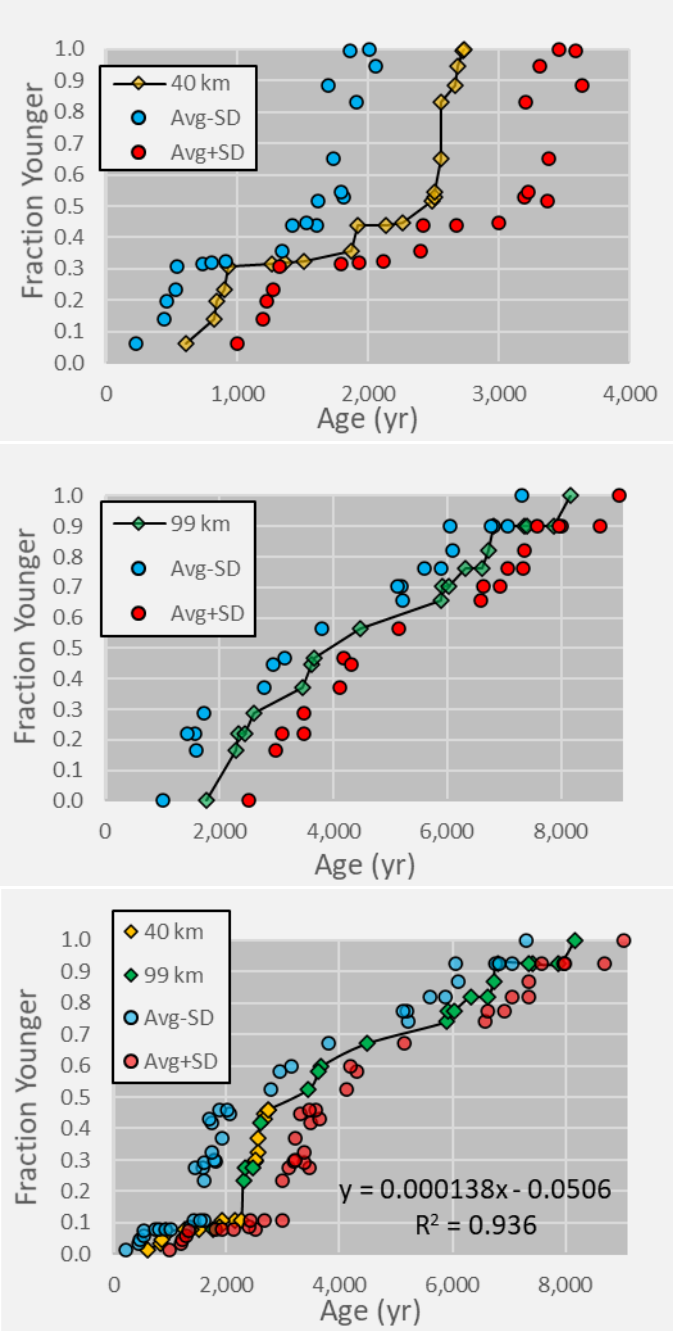

Figure 13. Cumulative TTDs for the 40 km (top), 99 km (center), and combined sampling areas. Yellow and green diamonds are the average of each positive age from the 17 accepted modeling scenarios. Average age minus standard deviation (SD) is shown in blue, age plus SD in red (data in Table 25). Only positive estimates of age were used to calculate average age and SD. The equation and R^2 value in the bottom panel is the linear best fit for all yellow and green diamonds.

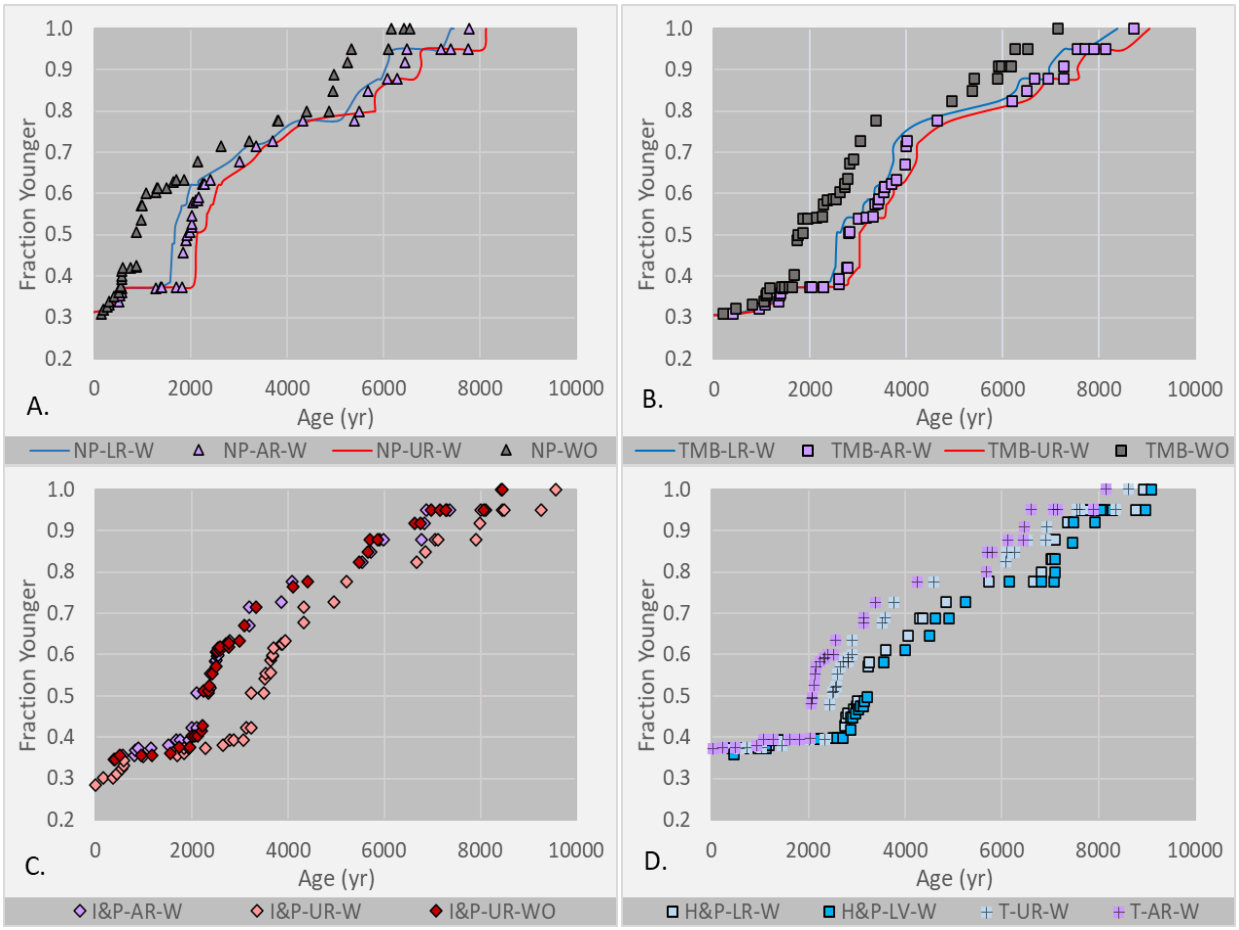

Figure 14. Selected cumulative TTDs resulting from modeling scenarios under A) NETPATH modeling, B) the Tamers mass balance model, C) the Ingerson and Pearson model, and D) the Han and Plummer and Tamers models. In graphs A and B, the TTDs based on the upper regression and lower regression scenarios are shown as lines rather than individual points for purposes of clarity (the upper, average, and lower regression TTDs are all very similar). Negative modeled ages were excluded from plots.

Maloszewski and Zuber (1996) explain that the exponential model can be used to model groundwater transit times in places with a shallow unsaturated zone, and also note (page 27):

> "The exponential model can be used for [unconfined aquifers] providing the transit time through the unsaturated zone is negligible in comparison with the total transit time. This condition results from the shape of the weighting function (Fig. 2) in which the infinitesimally short transit time appears. It is a common mistake to fit EM to the data obtained on samples taken ... from a phreatic aquifer but with a thick unsaturated zone. In all such cases the extremely short transit times do not exist, and, consequently, EM is not applicable."

It seems unlikely the issues raised by Maloszewski and Zuber (1996) in this quote are a concern here, because the presence of bomb ^{14}C in groundwater samples from shallow wells, and the $^{3}H/^{3}He$ ages <75 yr in streambed groundwater, are consistent with unsaturated zone transit times that are much shorter than the ^{14}C ages computed for groundwater from the 40 km and 99 km sampling areas.

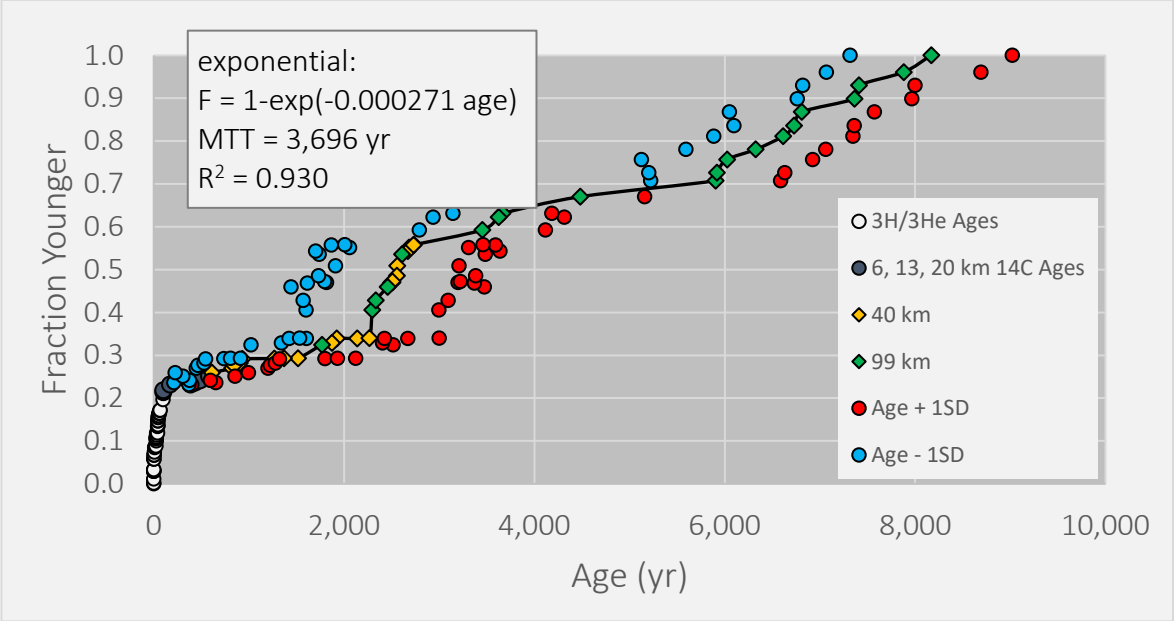

Figure 15. Cumulative TTD for all riverbed groundwater samples based on average ^{14}C ages (Table 25) and $^{3}H/^{3}He$ ages from the University of Utah.

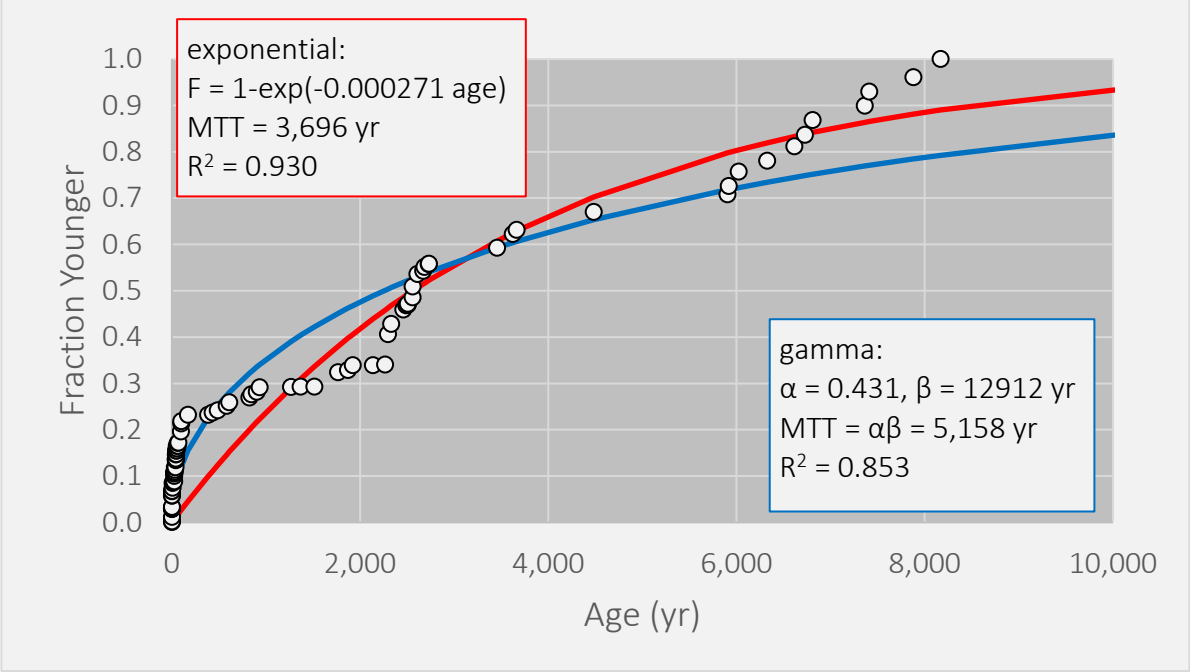

Figure 16. Exponential and gamma distributions fit to the TTDs based on average 14C ages (Table 25) and $^{3}H/^{3}He$ ages from the University of Utah.

6. Discussion

6.1. Uncertainty in Groundwater Ages

There are numerous factors influencing the uncertainty of the groundwater age estimates produced for this study. These factors can be grouped into three primary categories: 1.) uncertainty due to chemical/isotopic process assumptions in the $^{14}C_{REF}$ models, 2.) uncertainty in isotopic composition of C sources, and 3.) analytical uncertainty in measured C isotope values, and groundwater temperature and chemistry.

Individual $^{14}C_{REF}$ models are premised on different assumptions about the geochemical and isotopic processes occurring in the aquifer, and they require different input data to calculate $^{14}C_{REF}$ and groundwater age. For example, the H&P model involves C isotope exchange between DIC and CO_2 (or calcite), while the other models do not. The NP and TMB models include other reactions in addition to calcite dissolution, such as oxidation of SOM, Mg-carbonate dissolution, and gypsum dissolution. The H&P and I&P models use ^{13}C data to calculate $^{14}C_{REF}$ and groundwater age, while the other models do not. While each model considers reactions that may have occurred in the aquifer, it is not feasible to know with certainty which model best represents the conditions experienced by the samples analyzed in this study.

Additionally, there is uncertainty in the isotopic values of C sources used as inputs to the models. Uncertainty in $\delta^{13}C_g$ and $\delta^{13}C_s$ affects the H&P and I&P models, while uncertainty in $^{14}C_s$ affects all of the models used. The ^{14}C and ^{13}C values of C sources in the Sand Hills have varied over time as changing climate shifted the C3/C4 plant ratio (Chapter 2). These changes led to $\delta^{13}C_{SOM}$, $\delta^{13}C_g$, and $^{13}C_s$ having different values at different times (Goble et al. 2004; Mason et al. 2008; Layzell et al. 2020). Dune migration during severe drought led to relict paleosols being preserved in some places and destroyed in others, which resulted in spatial heterogeneity in subsurface $^{14}C_{SOM}$, $\delta^{13}C_{SOM}$, and $\delta^{13}C_s$ seen in the Sand Hills today (Nicholson and Swinehart 2005; Miao et al. 2007b; Mason et al. 2020; Tecsa et al. 2020). In modern Sand Hills soils $\delta^{13}C_{SOM}$ varies spatially with wetlands exhibiting lower values and dunes higher (Moussel 2007). $\delta^{13}C_g$ is also likely to vary spatially due to its dependence on the value of $\delta^{13}C_{SOM}$ (Cerling et al. 1991). $\delta^{13}C_g$ in the Sand Hills probably varies seasonally as well given the high seasonal variability of soil respiration rates (Moussel 2007).

The C isotopic values used in $^{14}C_{REF}$ models have been constrained (Chapters 2 and 5), but given the variability of these values in the Sand Hills they are probably less tightly constrained than for $^{14}C_{DIC}$ age dating studies in settings with more temporally consistent C3/C4 plant ratio and aquifers where carbonates are of ancient marine origin.

Laboratory analytical uncertainty associated with the measured parameters for each sample constitutes a third category of uncertainty. Numerous references from the groundwater $^{14}C_{DIC}$ dating literature report that analytical uncertainty is in almost all cases lower than uncertainty associated with geochemical process assumptions built into $^{14}C_{REF}$ models and uncertainty due to assumptions about the values of C isotope sources (Tamers 1967, Plummer and Glynn 2013, Han and Plummer 2016, McCallum et al. 2018, Cartwright 2020, Han and Wassenaar 2021).

Common methods of formal uncertainty assessment such as Monte Carlo uncertainty analysis and Gaussian error propagation would still fall short of fully capturing groundwater age uncertainty because these methods cannot incorporate uncertainty associated with the models' chemical/isotopic process assumptions, and the degree to which these assumptions are applicable to the samples being analyzed. Rather than applying these methods to one model at a time, with one set of model input values at a time, another approach was taken to understand and illustrate groundwater age uncertainty. I assumed that the spread in estimated ages resulting from the ensemble of accepted model simulations (Table 25, Figure 13) was a reasonable index of the possible uncertainty in groundwater age. The sensitivity of modeled age to incremental variation of model input parameters was also quantified. This

sensitivity analysis focused on the C isotope input variables, which are likely much larger sources of uncertainty in age than the chemical input values such as measured Ca and DIC concentrations in the groundwater samples.

The spread in ages represented by the 17 accepted modeling scenarios seems a reasonable index of uncertainty in age, based on the steps taken to ensure that results represented the most likely ages for the samples, namely:

1. Defining the range of C isotope values for C sources in the study area.
2. Determining the most likely values of these sources in potential recharge areas.
3. Identifying the likely geochemical/isotopic reactions occurring in the aquifer by performing graphical analysis of the chemistry and isotopic signatures of the samples.
4. Selecting groundwater $^{14}C_{DIC}$ age models that could simulate the reactions identified.
5. Applying the ensemble of chosen models across the range of C isotope values identified for the site.
6. Rejecting simulations that produced impossible $^{14}C_{REF}$ values greater than 102 pmc or negative groundwater ages.

Much of the uncertainty in C isotope values was accounted for in the application of the $^{14}C_{REF}$ models as described in chapter 5. By applying the ensemble of models to the data using a range of $\delta^{13}C_g$ and $^{14}C_s$ values (Table 15) and integrating the results into a representative age for each sample (Table 25), the effects of uncertainty in $\delta^{13}C_g$ and $^{14}C_s$ are represented in the average age produced by the 17 accepted modeling scenarios and the standard deviation of these values across the ensemble. Having reduced the uncertainty in the isotopic composition of C sources by as much as possible, the other primary sources of error in the groundwater age results are the chemical/isotopic process assumptions underlying the models, which may oversimplify the geochemical reactions occurring within the aquifer. At least one other study (Kreuzer et al. 2008) applied a multi-model ensemble approach to groundwater $^{14}C_{DIC}$ age modeling. They also presented the average age produced by their chosen models and represented the range in age for each sample as the mean of the simulated ages ± 1 standard deviation.

Additional insight comes from understanding the sensitivity of groundwater age calculations to incremental variation of model inputs. This was assessed with a series of model experiments in which the primary isotopic variables affecting the calculation of $^{14}C_{REF}$ and age were varied above and below likely values in the Sand Hills, in increments of plus or minus 1‰ or 1 pmc. For each model I changed one C isotopic value ($\delta^{13}C_g$, $\delta^{13}C_s$, or $^{14}C_s$) while all other model inputs were held constant. $^{14}C_g$ was maintained at 100 pmc.

I calculated the age of each sample from the 40 and 99 km sampling areas (41 samples in all) for different C isotope input values, varying one input value at a time, and then computed the mean age of the 41 samples for each set of input values (Figure 17). I next quantified the effect that changing a C isotope input value by 1 unit (1‰ for experiments 1 and 2, and 1 pmc for experiment 3) had on the average age (Figure 18). To do this I subtracted the average age produced by one model at one C isotope input value from the average age produced by the same model at a different input value 1‰ or 1 pmc greater. For instance, the average age produced by the I&P model when $\delta^{13}C_s$ = -6‰ is -3,004 yr, and the average age produced by the I&P model when $\delta^{13}C_s$ = -7‰ is -6,871 yr. I subtracted -6,871 yr from -3,004 yr to arrive at the value of 3,867 yr for the I&P model between the $\delta^{13}C_s$ values of -7 and -6‰ (Figure 18).

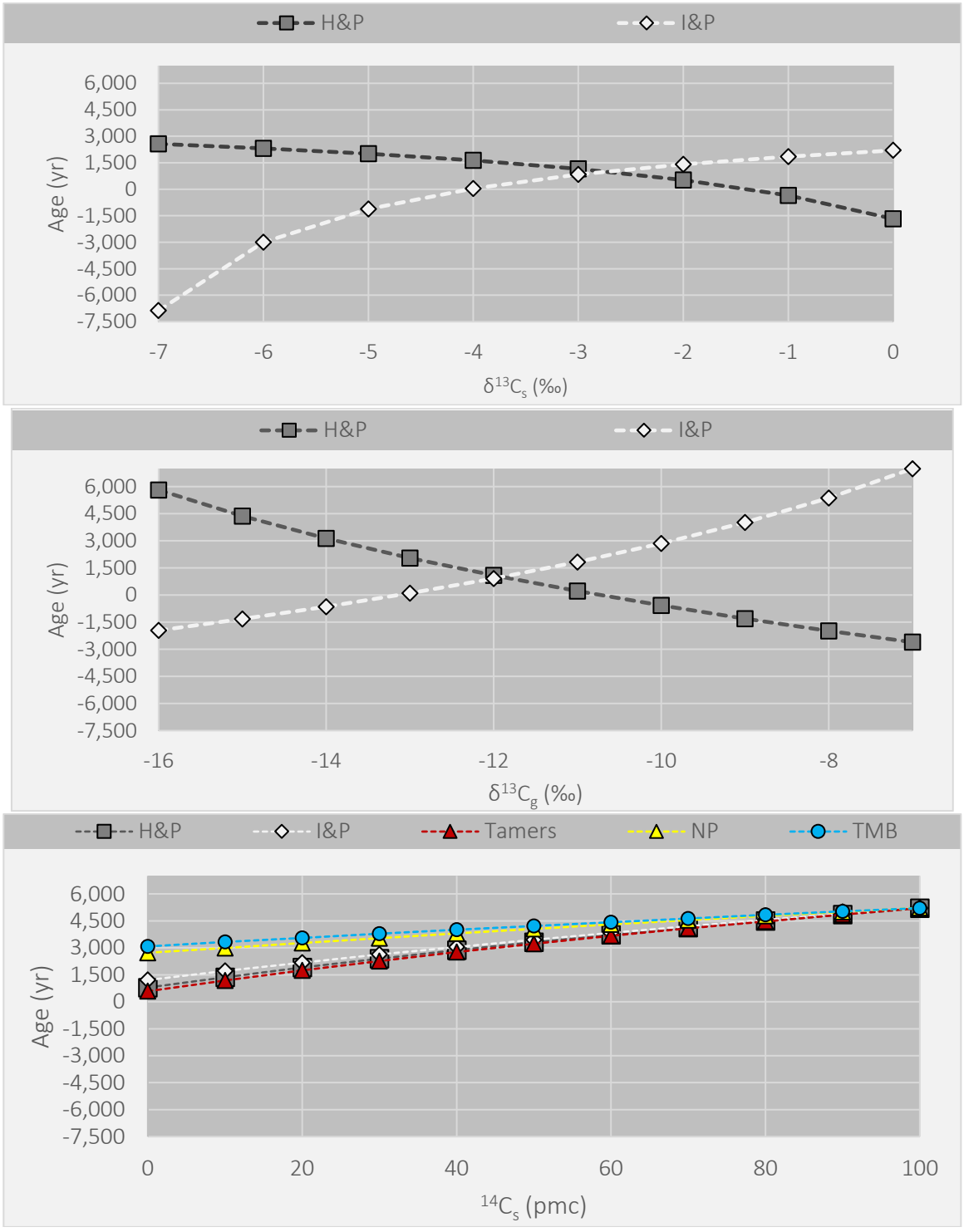

Figure 17. The effect on groundwater age of varying the estimate of the C isotopic composition of a C source, for the models used in this study. Experiments 1, 2, and 3 are shown in the top, middle, and bottom panels respectively. Each point represents an average age for all 41 groundwater samples from the 40 and 99 km sampling areas; negative ages are not possible and indicate poor model performance.

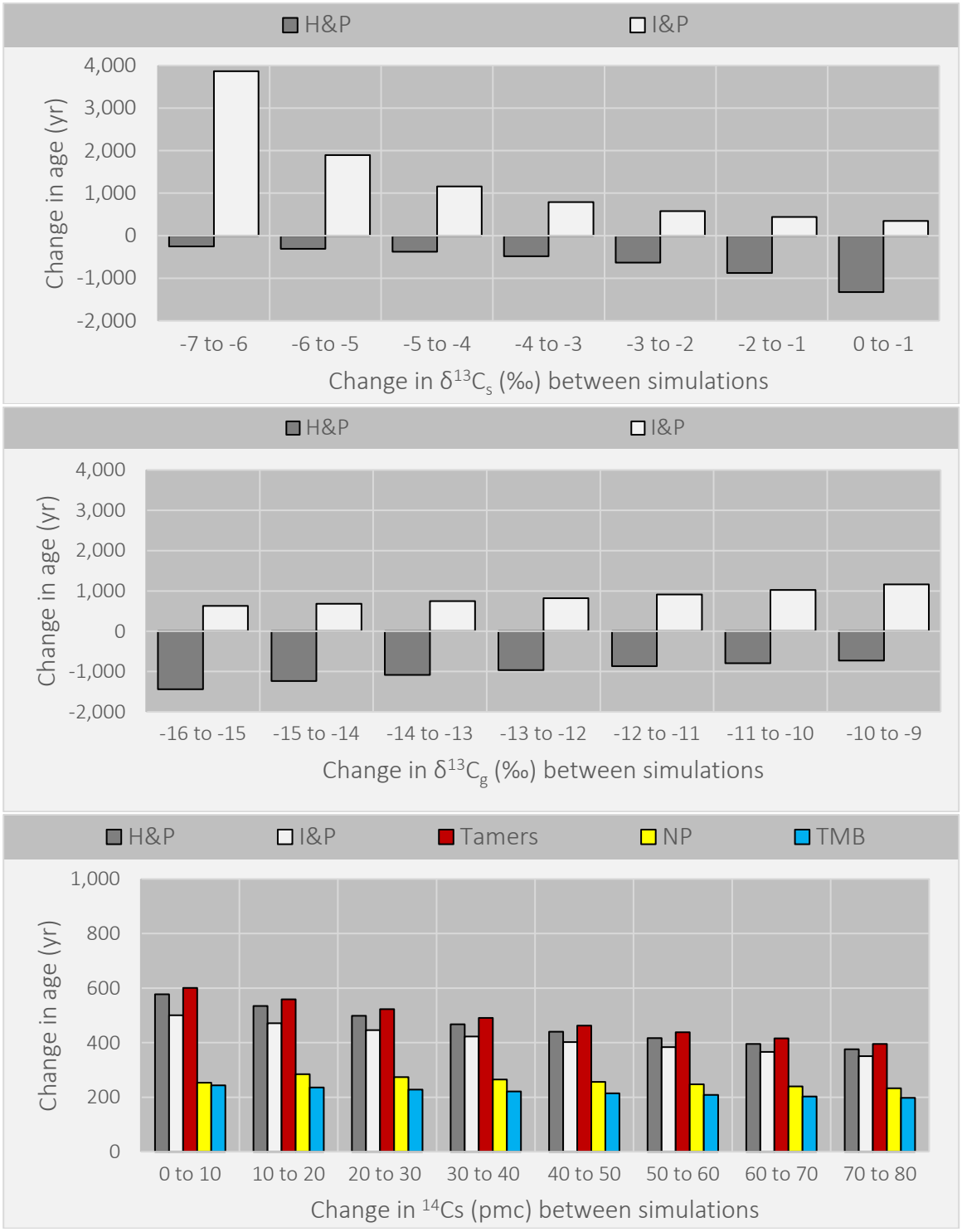

Figure 18. Change in average age for the 40 km and 99 km groundwater samples (n = 41) between successive simulations in experiments 1, 2, and 3 (top, middle, and bottom respectively). The magnitude of the age difference varies by model and the C isotope being changed.

In experiment 1, $\delta^{13}C_s$ was varied while $\delta^{13}C_g$ was -11.67‰ ($\delta^{13}C_g$ for the "average regression", Table 15) and $^{14}C_s$ was 0 pmc. In experiment 2, $\delta^{13}C_g$ was varied while $\delta^{13}C_s$ was -2.39‰ (Tables 2, 15) and $^{14}C_s$ was 0 pmc. In experiment 3, $^{14}C_s$ was varied while $\delta^{13}C_g$ was -11.67‰ and $\delta^{13}C_s$ was -2.39‰. Of the models that led to the 17 accepted sets of ages (Table 25), only the I&P and H&P models use $\delta^{13}C_g$ or $\delta^{13}C_s$ to calculate $^{14}C_{REF}$. Thus, experiments 1 and 2 resulted in no variation in age or $^{14}C_{REF}$ for the Tamers, TMB, and NP models. Overall, the largest sensitivities appear to be the sensitivity of I&P and H&P ages to the input values of $\delta^{13}C_g$ or $\delta^{13}C_s$ (Figure 18). Across the range of C isotope values tested, H&P was most sensitive to changes in $\delta^{13}C_g$, I&P was most sensitive to changes in $\delta^{13}C_s$, and the Tamers model was most sensitive to $^{14}C_s$.

For the H&P and I&P models, changing the $\delta^{13}C$ input by 1‰ resulted on average in the absolute value of age changing by 958 yr. Assuming that uncertainty in the values of $\delta^{13}C_g$ and $\delta^{13}C_s$ is 2‰ leads to an error of 1,916 yr for each sample. For comparison, the average standard deviation for all samples from the modeling ensemble is 625 yr, while the median, maximum, and minimum are 676, 1016, and 15 yr respectively. Increasing $^{14}C_s$ by 1 pmc (equivalent to a 10‰ increase in $^{14}C_s$) resulted in an age increase of 35 yr on average across the 5 models, meaning a 1‰ increase in $^{14}C_s$ would result in an age increase of only 3.5 yr on average, while the same increase in $\delta^{13}C_g$ or $\delta^{13}C_s$ would result in age changing by about 604 to 889 yr for the I&P and H&P models. These results demonstrate that the H&P and I&P models are much more sensitive to incorrect assumptions about $\delta^{13}C$ values than about $^{14}C_s$.

The increase or decrease in age calculated by the H&P and I&P models are of the same magnitude but have opposite directions. As such, when $\delta^{13}C_g$ is underestimated, the H&P model will calculate a higher groundwater age, while the I&P model will calculate a lower age.

6.2. Spatial distribution of the age of groundwater storage and discharge

6.2.1. Longitudinal Distribution of Age for Groundwater Discharging Through the Riverbed

There is a strong west to east (upstream to downstream) trend of increasing groundwater age among the samples analyzed for this study. Downstream of the 20 km sampling area, the MTT of discharging groundwater increases by 106 yr per km of distance along the channel on average (Figure 19, Table 26); the average seepage rate also increases eastward (Figure 20). Samples from the 40 and 99 km sampling area constituted 13 and 62% of all groundwater flux measured across the five sampling respectively, and combined they contributed 75% of all groundwater seepage across the study site, demonstrating that very old groundwater is the primary contributor to streamflow generation at the sites we sampled.

Table 26. Mean transit times, seepage fractions, and geodesic distance east of the study zero point near the headwaters, for each of the 5 sampling areas. Distance was measured using ArcGIS Pro V.2.4.2.

Sample Area	MTT (yr)	fraction of total q	Distance west of 0 point (km)
6 km	174	0.02	5.4
13 km	84	0.06	8.2
20 km	52	0.17	10.6
40 km	1,944	0.13	20.8
99 km	5,029	0.62	53.7
Total	3,386	1.00	--

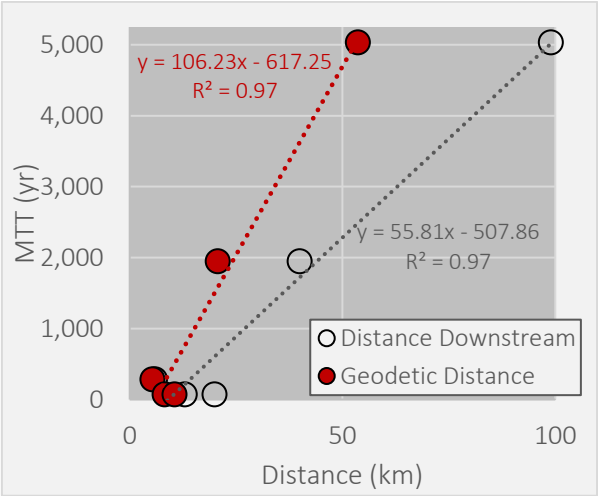

Figure 19. Variation in MTT with distance downstream (measured along the channel) or geodetic distance east of the zero point (Figure 2). MTT at the 6, 13, and 20 km sampling areas was based in part on data analysis at the University of Utah (Solomon and Humphrey, personal communication, November 16, 2020). Geodetic distance was measured using ArcGIS Pro V.2.4.2.

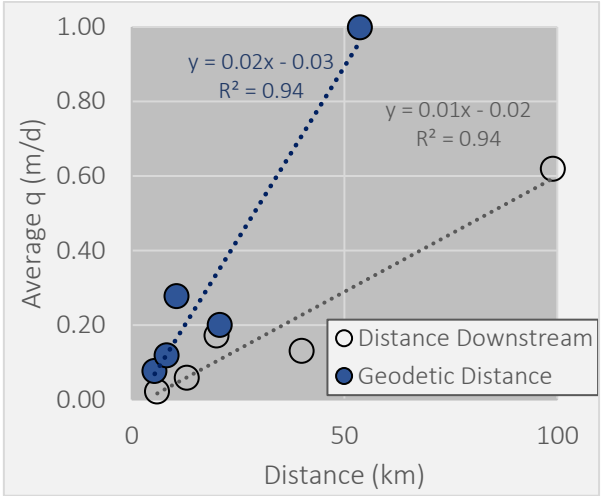

Figure 20. Variation in average q with distance downstream (measured along the channel) and geodetic distance east of the zero point (Humphrey et al. 2020). Distance was measured using ArcGIS Pro V.2.4.2.

At the 40 km sampling area none of the streambed groundwater points were young enough to be dated using $^{3}H/^{3}He$ methods as determined by our collaborators at the university of Utah. No young groundwater was identified at the 99 km sampling area or the nearby SEN well nest, suggesting that the groundwater collected at these points recharged far from the sampling area. Young groundwater may discharge in/near the 99 km sampling area at locations other than the 20 riverbed sampling points, such as closer to the riverbanks or in nearby tributary streams or gullies, but that was not observed or sampled.

Geomorphic evidence that shallow flowpaths discharge before reaching the riverbed comes in the form of "theater headed gullies" which are present throughout the Sand Hills, particularly in areas where the slope of the land surface is steepest (Guhman 1990; Guhman and Pederson 1992). Brice (1966) measured the rate at which the gullies retreated up the hillslope. These geomorphic perturbations can cause groundwater to discharge at gully knickpoints (breaks in land surface slope within gully channels) (Dunne 1990). This can generate a feedback loop of increased erosion driven by groundwater discharge and increased capture of flowpaths as the gully knickpoint migrates upslope, in turn capturing shallow groundwater flowpaths (Dunne 1990). In describing the process of groundwater capture and groundwater driven erosion of gullies, Dunne (1990, p. 14) states:

> "If seepage erosion occurs, it perturbs the [groundwater outflow] boundary, and again increases the flow convergence, increasing the probability of further seepage erosion. As the head of the embayment retreats into the land surface or hillslope, this flow convergence will increase, setting up a positive feedback loop that affects the growth of a new valley."

Guhman (1990) measured gullies draining into the Dismal River, another groundwater dominated river in the Sand Hills located 25 km south of the Middle Loupe River; the Dismal River flows into the Middle Loupe River east of the study area. In her characterization of the gullies surrounding the Dismal River, Guhman found that "1. Groundwater discharge is eroding sediments along the Dismal River. 2. Sapping

by groundwater is both initiating and enlarging gullies. 3). Sapping involves both contact and boiling springs, sometimes in the same gully." Guhman's work suggests that discharge of shallow (and therefore relatively young) groundwater into gullies could be an important process in the Sand Hills, potentially accounting for the lack of young groundwater samples beneath the main riverbed at the 40 and 99 km sampling areas. The absence of young groundwater at the 40 and 99 km transects may be at least partly a product of gully formation in the steep valley slopes that border the Middle Loup River. At least one running spring near the 40 km sampling area was located by collaborators in this study, though $^{14}C_{DIC}$ samples were not collected.

The trend of increasing age with downstream distance suggests that a larger fraction of deep groundwater flowpaths discharge downstream of the 20 km sampling area. It also fits the conceptual model set out by Modica et al. (1997) for gaining streams in unconfined aquifers, which predicted that baseflow and the mean age of groundwater discharge would increase with distance downgradient from the regional groundwater divide. They predicted that the age of groundwater discharging through the streambed would be more uniform near the headwaters, would increase with distance downstream, and that older water would discharge at the center of the stream. The range in groundwater age across a sampling transect was more uniform at the 6, 13, and 20 km sampling areas than it was at the 40 and 99 km sampling areas, as groundwater discharging closer to the stream's headwaters was much younger than at the 40 and 99 km sampling areas.

6.2.1. Groundwater flowpath length and potential recharge zones

Older samples (which tend to discharger farther from the headwaters of the study stream) may have traveled much greater distances through the aquifer than younger samples. Aquifer properties can be used in tandem with ages derived from isotopic tracers to make a rough estimate of groundwater flowpath length, and thus the location of potential recharge area, based on Darcy's equation (McGuire and McDonnell 2006):

$$\Delta x = (Age)\left(\frac{K}{n_e}\right)\left(\frac{dh}{dx}\right) \quad (10)$$

Where K is the average horizontal hydraulic conductivity, n_e is effective porosity, dx is a distance along a flowpath, and dh is the change in head over the distance dx. Applying the age of each riverbed sample (Table 25) to equation 10, I determined a range of potential flowpath distances for the samples from 40 and 99 km, assuming groundwater flow is driven by the hydrologic gradient (dh/dx) between the center of the water table mound in the western Sand Hills (Figure 21) and the 99 km sampling area. Approximate values of Δx were calculated using the average horizontal conductivity data for the High Plains Aquifer presented in Houston et al. (2013) (K = 4.10 km/yr), effective porosity of fine to medium sand presented in Fetter (2018) (n_e = 0.3), and deriving Δh and Δx from water the water table contours of Summerside et al. (2001) (Δh = 0.29 km, Δx = 116 km, J = 0.00250) (Summerside et al. 2001). Average flowpath distances plus or minus one standard deviation for the 40 and 99 km sampling areas were 68 ± 25 and 174 ± 71 km, respectively (Figure 21). The minimum and maximum estimated flowpath lengths to the 40 km sampling area were 21 and 93 km respectively; corresponding estimates for the 99 km sampling area were 60 and 279 km. The potential recharge areas shown in Figure 21 were calculated as geodetic radial distances from the 40 and 99 km sampling areas using the "Multiple Ring Buffer" tool in the "Analysis" toolbox in ArcGIS Pro V.2.9.1. The rings were then clipped such that upgradient portions of the constructed polygons remained. The 40 km polygon is defined by distances 43 – 93 km west of transect 40550 between 147°31'55" and 213°53'02", and the 99 km polygon is defined by distances 103

to 245 km west of transect 99090 between 153°27'50" and 202°53'56". Potential recharge areas were intentionally constructed to be broad to accommodate variability in water table configuration over time.

Potential recharge areas for the 40 km and 99 km sampling areas bound an area in the western Sand Hills with a particularly low head gradient at roughly 102°10' to 102°30' west longitude (Figure 21), which has been cited in previous studies as representing the western boundary of the groundwatershed (Chen et al. 2003; Chen and Chen 2004). Flowpath distances derived from Equation 10 imply that groundwater discharging in the present at 99 km may have recharged west of the area of low gradient, with maximum potential flowpath distances up to 279 km from the 99 km sampling area (Figure 21). While it is possible that groundwater discharging at the 99 km sampling area recharged to the west of the low gradient water table mound in the western Sand Hills, it's also possible these flowpaths could be shorter if they penetrated deeper into the aquifer where groundwater velocity may be slower (where the values of K and dh/dx used in Equation 10 might overestimate specific discharge). Deep flowpath penetration seems possible, as discussed in Section 6.2.1 below.

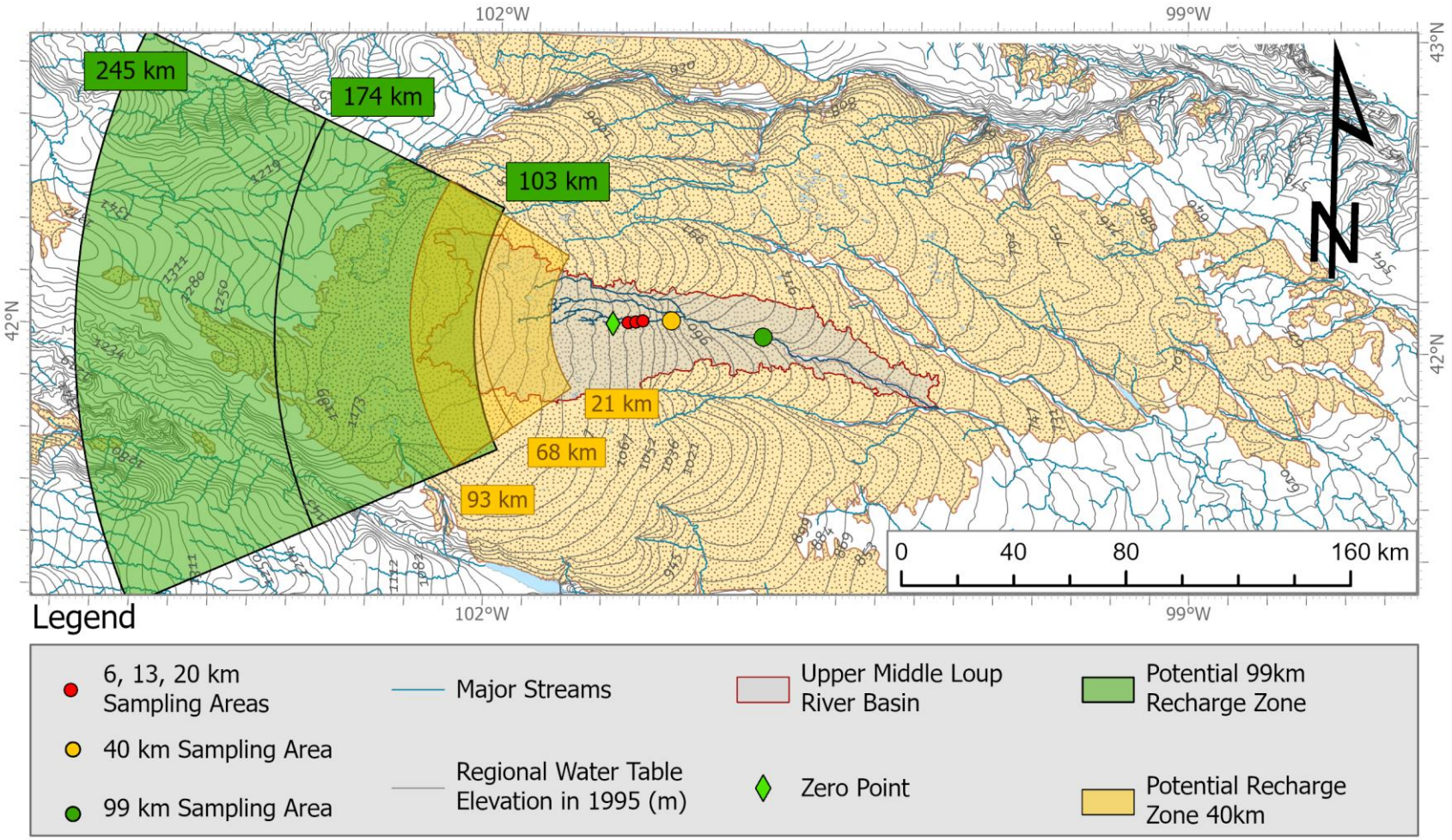

Figure 21. Potential recharge areas for samples collected at the 40 and 99 km sampling areas. The yellow and green polygons show the average upgradient flowpath length, plus or minus one standard deviation, implied by the ages of samples collected at the 40 and 99 km sampling areas, as calculated with equation 10. Geodesic distances were calculated using the "Multiple Ring Buffer" Analysis tool in ArcGIS Pro 2.9.1. Hydrologic gradient was calculated using data from Summerside et. al. (2001), shown in the figure as gray contours representing the elevation of the water table in 1995.

6.2.3 Vertical gradients in age and $^{14}C_{DIC}$

Groundwater ages derived from well samples (Table 27) indicate that in the western half of the watershed, the aquifer is vertically stratified with relatively young groundwater (up to 28.8 m below the water table) overlying groundwater that recharged before 1950. As depth below the water table increases, so does groundwater age (Table 27 and Figure 22). The one exception to this is in well 9-GSL-94 where the sample from the deepest screen (28.8 m below the water table) appears to be younger than the sample above it (21.39 m below the water table) (Table 27).

McMahon et al. (2007, page 35) found similar conditions in the southern Sand Hills, concluding that "water in the aquifer was chemically and temporally stratified in the study area, with a relatively thin zone of recently recharged water (less than 50 years) near the water table overlying a thicker zone of older water". The apparent stratification of ages in the aquifer allowed me to test whether the distribution of ages below the water table behaved as predicted for a uniform unconfined aquifer. Transit times in an idealized unconfined aquifer with uniform recharge, thickness, and a non-sloping lower boundary are independent of horizontal location and vary as a function of porosity (θ), recharge rate (R), depth below the water table (z), and aquifer thickness (Z) (Solomon et al. 2006):

$$t = \frac{Z \cdot \theta}{R} \cdot \ln\left(\frac{Z}{Z - z}\right) \qquad (11)$$

Table 27. Well depth, elevation, and age data for groundwater samples from wells in this study. *Depth to the water table was not measured for this well (the drinking water well at GSL) at the time of sample collection. This value was estimated assuming that depth to the water table was equal to the static water level reported at the time of well installation.

Well ID	Elevation of Middle of Screen (m)	Depth of Middle of Screen Below Water Table (m)	$^{14}C_{DIC}$ (pmc)	17 Scenario Average Age (yr)
9-GSL-94-S	1066.14	1.07	104.7	< 65 yr
9-GSL-94-M1	1050.67	16.64	104.4	< 65 yr
9-GSL-94-M2	1046.01	21.39	83.7	421
9-GSL-94-D	1038.41	28.80	97.7	< 65 yr
01-GSL-2020-S	1051.47	3.66	99.4	< 65 yr
01-GSL-2020-M1	1050.06	4.97	106.2	< 65 yr
01-GSL-2020-M2	1047.27	7.81	108.6	< 65 yr
01-GSL-2020-D	937.47	116.02	46.6	3,617
01-SEN-2020-S	902.82	3.19	68.0	811
01-SEN-2020-M	890.84	16.31	55.8	2,767
01-SEN-2020-D	873.56	33.72	54.2	2,988
01-GSL-2003a	888.49	194*	21.1	10,362
01-GSL-2003b	888.49	194*	21.1	10,324

Equation 11 implies an exponential groundwater TTD, which may be at least approximately realistic for the study site (Fig. 16). Equation 11 was fit to the ages derived from well samples (Table 27) using a published recharge value for the Sand Hills (R = 0.073 m/yr, Szaliygi and Jozsa, 2012) and a least squares method implemented in Microsoft Excel using the Solver add-in which allowed the value of θ to vary between 0.00001 and 1, and Z to vary between 1 and 1000 m (black dashed curve in Figure 22). The resultant estimate of porosity was unrealistically high (θ = 0.99) though the optimized value of Z (196.8 m) seems potentially realistic. R was then allowed to vary along with θ and Z while fitting Equation 11 to the age results from the wells. θ was allowed to vary between 0.00001 and 0.9, R was allowed to vary

between 10^{-5} and 1 m/yr, and Z was allowed to vary between 194 m (the depth of the deepest well, 01-GSL-2003, below the water table) and 1000 m. The best fit gave θ = 0.3327, Z = 246.4 m, and R = 0.0123 m/yr (blue dashed line, Figure 22). This value for recharge is nearly 6 times lower than the value reported by Szaliygi and Jozsa (2012).

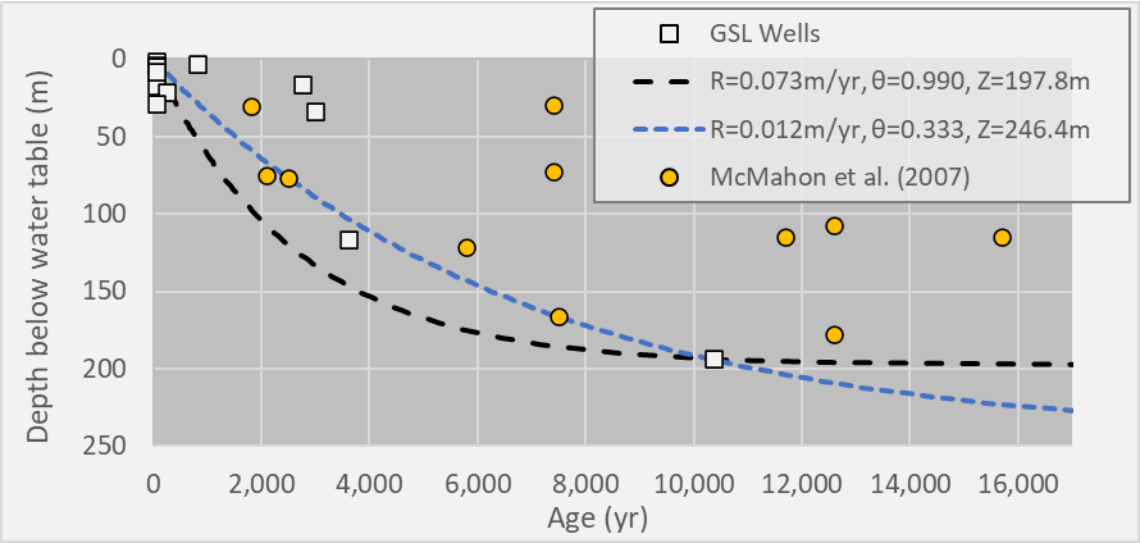

Figure 22. Groundwater age and depth for well samples from the study (white squares) and the associated best fit of equation 11 to these ages when recharge was fixed at 0.073 m/yr (Szilagyi et al. 2012) while θ and Z were allowed to vary (black dashed line). Also shown is Equation 11 when θ = 0.3327, Z = 246.4 m and R = 0.0123 m/yr (blue dashed line). Yellow circles are groundwater samples from McMahon et al. (2007).

It should be noted as well that θ and R cannot be estimated independently from either approach above, because they appear only as the ratio θ/R in Equation 11. In fitting Equation 11, a higher value for R would require a higher value for θ (Solomon et al. 2006).

When R was allowed to vary during fitting, the result (0.0123 m/yr) was 6x lower than the value of R found by Szaliygi and Jozsa (2012). This is similar to results in McMahon et al. (2007), who reported recharge estimates of 0.009 to 0.015 m/yr based on vertical age gradients in samples collected from two separate well nests in the Sand Hills approximately 90 km south of our study site, and found estimates of recharge were "2 to 6 times smaller than the recharge rates estimated for the Sand Hills on the basis of a regional ground-water flow model (Luckey and others, 1986)." One notable difference between the uniform aquifer and the aquifer underlying the study site is that the saturated thickness of the High Plains Aquifer decreases by about half from west to east across our study site (Hobza et al. 2011; Hobza et al. 2012) which may be one cause of discrepancy between our calculation and the idealized aquifer.

Another consequence of the vertical stratification of groundwater in our samples is that Equation 11 can be rearranged to estimate "z", which could be interpreted as the maximum depth of penetration below the water table for each groundwater sample collected in the 40 km and 99 km sampling areas (Figure 23). To do this I first calculated the fractional depth of penetration for each sample (Z/Z-z) assuming the parameter values for the blue curve in Figures 22 and 23, (Eq. 7 with θ = 0.3327, Z = 246.4 m, and R = 0.0123 m/yr) and then solved for z.

Hobza et al. (2012) reported the thickness of sediments comprising the High Plains Aquifer from boreholes in Thomas County. The average of the three depths closest to the 99 km sampling area is 240 m, which is quite similar to aquifer depth calculated using Equation 11. The estimated depth of penetration of the oldest sample from the 99 km sampling was 174 m, 71% of the modeled total aquifer thickness.

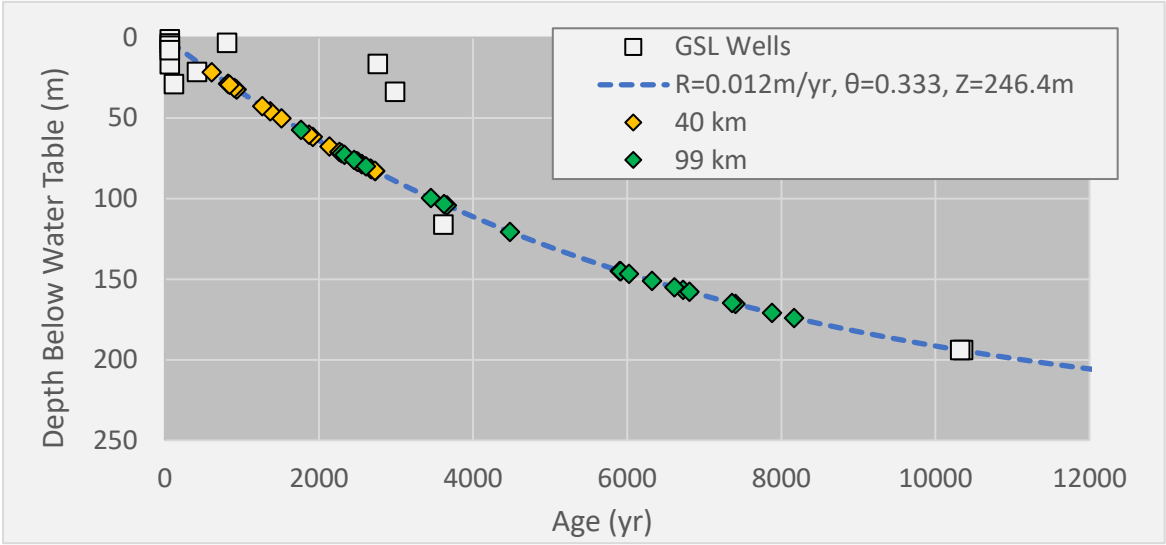

Figure 23. Estimated depth of penetration below the water table for groundwater samples from the 40 and 99 km sampling areas, based on the best fit of Equation 11 to the GSL well ages when θ = 0.3327, Z = 246.4 m and R = 0.0123 m/yr (blue dashed line). The youngest sample from the 40 and 99 km sampling areas (40600R20) is estimated to have a maximum penetration depth of just 22 m while the oldest of these samples (99090R33) is estimated to have a maximum penetration depth of 174 m. These depths correspond to 9 and 71% of the total aquifer thickness, respectively.

6.2.4. Variation of Groundwater Age and Seepage Across Sampling Transects

In baseflow driven streams, at any distance along the length of the channel, flowpaths of varying lengths, penetration depths, and transit times terminate by discharging into the streambed (Modica et al. 1997; Browne and Guldan 2005; Modica et al. 1998; Gilmore et al. 2016). Flowpaths originating closer to the stream channel tend to discharge closer to the banks of the stream, while those originating further from the bank tend to discharge into the center of the stream (Modica et al. 1998). A consequence of this organization is that, on average, groundwater age beneath a streambed tends to increase from the stream bank to the center of the channel.

Regarding the distribution of groundwater ages across the channel, the oldest age occurred at or within 1 m of the center for three of the four 40 km transects (Figure 24). The samples from the 99 km sampling area had a greater overall range in age, and the age distributions were skewed slightly such that the oldest samples discharged about 3 to 6.5 m to the right of the channel center, on the inside of the meander bend. This may also be due in part to the interplay of groundwater flow geometry and channel sinuosity. Balbarini et al. (2017) modeled the effects of channel sinuosity on the geometry of the flow-field beneath a gaining stream in Denmark, finding that the deepest flowpaths discharged not in the center of the channel but on the inside of the meander after flowing under the stream (Figure 25). The implication of this phenomenon is that the oldest groundwater discharges toward the inside of the meander.

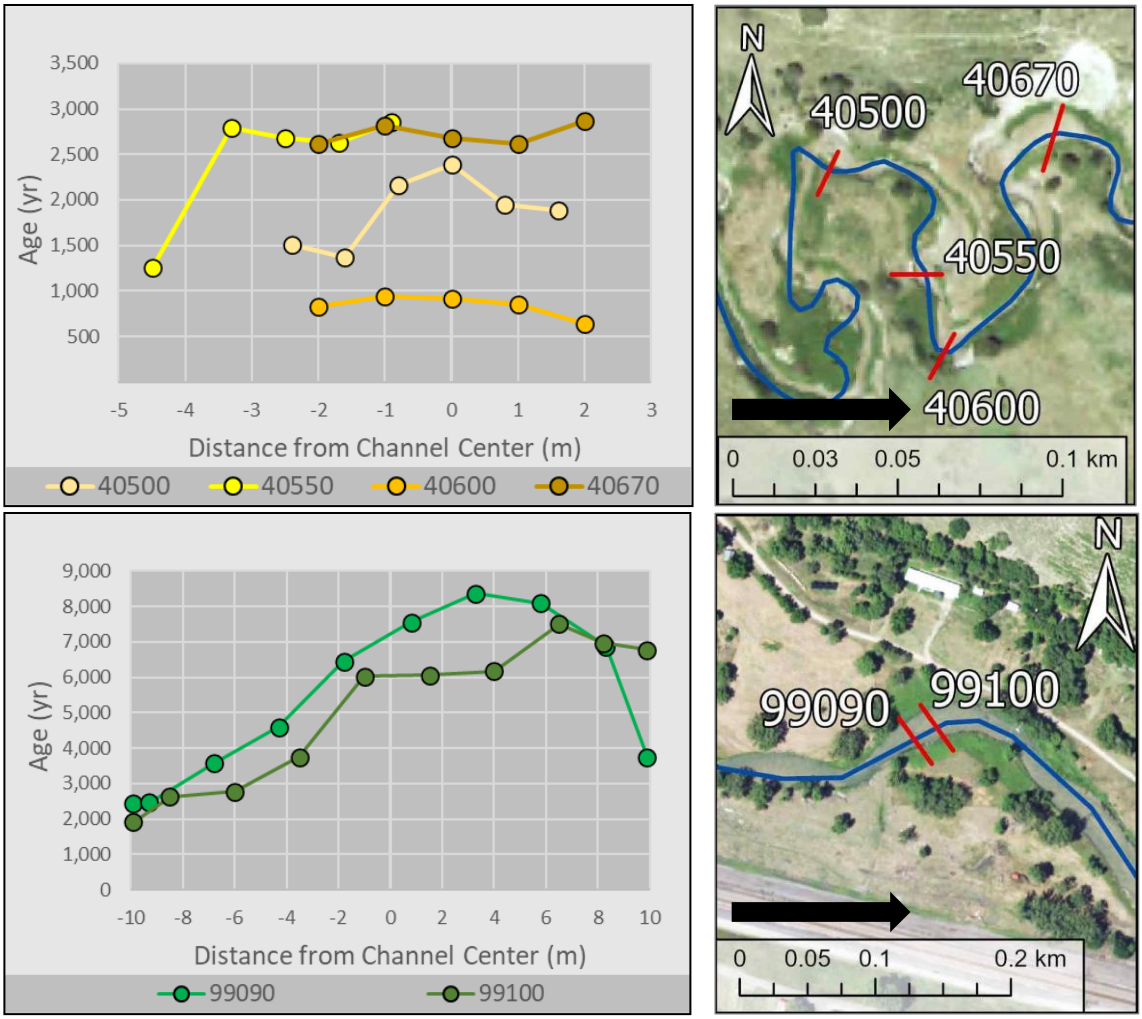

Figure 24. Variation in age of groundwater across riverbed transects (left panels) and transect position in relation to meanders (right panels) from the 40 km (top) and 99 km (bottom) sampling areas. While both transects from the 99 km sampling area show that the oldest groundwater discharged to the right of channel center (toward the inside of the meander), the trend is not as apparent for transects at the 40 km sampling area. Flow direction of the Middle Loup River is indicated by a black arrow in transect position maps.

The influence of meanders on the distribution of groundwater age across a channel may play a role but does not appear to be a dominant factor at the 40 km and 99 km sites, given that the shifting of oldest groundwater away from center seems strongest where the channel is straighter (99 km). The channel has larger tighter meanders at 40 km but the oldest groundwater discharge is more shifted away from center in the 99 km sampling area.

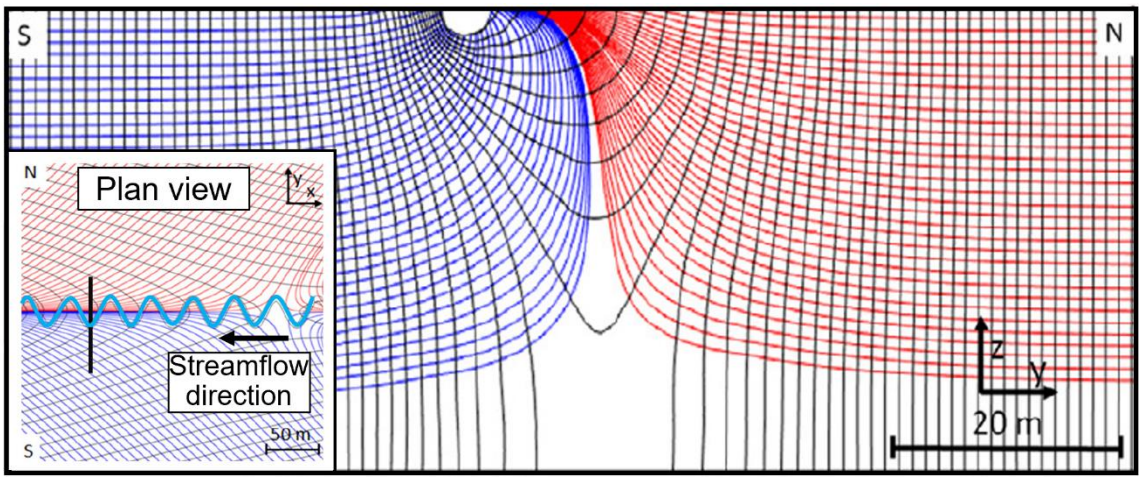

Figure 25. Effects of stream channel sinuosity on the geometry of the groundwater flow lines in a vertical cross-section beneath a uniformly sinuous gaining stream. The black line in the inset shows the line of the cross-section, and the stream channel is shown as a light blue sinusoid. Flow lines originating on the south side of the channel are shown in blue, while those originating from the north are shown in red. Thin black lines are groundwater equipotentials. Regional groundwater flow and streamflow are toward the west (left) in the inset plan view. Modified from Balbarini et al. (2017).

7. Conclusions

This study combined measurements of groundwater seepage flux and ^{14}C as a groundwater age-dating tracer at 100 points below the bed of the Middle Loup River to determine the mean transit time (3,386 yr) and transit time distribution of groundwater discharging to the river from the High Plains Aquifer. This work is the first to couple $^{14}C_{DIC}$ dating and groundwater flux measurements in a riverbed to quantify the TTD of groundwater discharge to a river. Groundwater discharging from the High Plains Aquifer into the middle Loup River was dominated by old groundwater, and the age of groundwater discharge increases with distance from the catchment's headwaters (Table 26).

In an "ensemble approach" to estimating groundwater age, the mean age from 17 accepted modeling scenarios was calculated for each groundwater sample. This mean groundwater age ranged from 611 to 2,733 yr at the 40 km sampling area, and 1,767 to 8,168 yr at the 99 km area (Table 25). The mean transit times (MTTs) at the 40 and 99 km sampling areas were 1,944 yr and 5,029 yr, respectively. Overall, the MTT of discharging groundwater increases eastward by 106 yr per km of geodetic (straight line) distance. Samples from the 40 and 99 km sampling areas contributed 75% of total groundwater discharge measured at the 5 groundwater sampling areas. Data from the cumulative TTD show that 66% of all discharging groundwater had ages greater than 2,000 yr and 29% of groundwater discharge was older 6,000 yr.

The relationship between the age of discharging groundwater and distance from the stream's headwaters suggest groundwater flowpath length and depth of flowpath penetration increase with distance from the headwaters of the stream network. Using published data on the effective porosity, hydraulic conductivity, and hydrologic gradient of the study area, flowpath distances implied by groundwater ages indicate recharge areas centered about 68 and 174 km west of the 40 and 99 km sampling areas, respectively.

The TTD based on $^{3}H/^{3}H$ ages for the younger groundwater (from the University of Utah) and ^{14}C ages for the older groundwater was better fit by an exponential model with a MTT of 3,696 yr (R^2 = 0.931) than a gamma distribution with a MTT of 5,158 yr (R^2 = 0.853) (Fig. 16). The MTT calculated directly from the data as the flow-weighted mean age was 3386 yr, similar to the value from fitting an exponential model to the cumulative TTD (Fig. 16).

The exponential shape of the TTD suggests that generalized lumped parameter models (such as the exponential model) may be suitable for modeling TTDs in large unconfined aquifers like the High Plains Aquifer. This study demonstrates that the TTD of a large aquifer can be estimated using field-based groundwater sampling and flux measurement at the point of discharge in a streambed or riverbed, even in the presence of very old groundwater. It also shows the importance of including tracers capable of dating groundwater up to tens of thousands of years old in field studies characterizing groundwater transit time distributions for aquifers.

Works Cited

Abrams, D., H. Haitjema, (2018). How Aquifer Characteristics of a Watershed Affect Transit Time Distributions of Groundwater: Groundwater, v. 56, no. 4, p. 517–520, doi: 10.1111/gwat.12788.

Amundson, R., Y. Wang, O. Chadwick, S. Trumbore, L. Mcfadden, E. Mcdonald, S. Wells, M. Deniro, (1994). Factors and processes governing the 14C content of carbonate in desert soils: Earth and Planetary Science Letters, v. 125, no. 1-4, p. 385–405, doi: 10.1016/0012-821x(94)90228-3.

Balbarini, N., W.M. Boon, E. Nicolajsen, J.M. Nordbotten, P.L. Bjerg, P.J Binning (2017). A 3-D numerical model of the influence of meanders on groundwater discharge to a gaining stream in an unconfined sandy aquifer: Journal of Hydrology, v. 552, p. 168–181, doi: 10.1016/j.jhydrol.2017.06.042..

Bennett, D.M., Fritz, S.C., Holz, J.C., Holz, A.A., and Zlotnik, V.A., (2007). Evaluating climatic and non-climatic influences on ion chemistry in natural and man-made lakes of Nebraska, USA: Hydrobiologia, v. 591, no. 1, p. 103–115, doi: 10.1007/s10750-007-0798-z.

Breecker, D.O., S. Bergel, M. Nadel, M. M. Tremblay, R. Osuna-Orozco, T.E. Larson, Z.D. Sharp (2015). Minor stable carbon isotope fractionation between respired carbon dioxide and bulk soil organic matter during laboratory incubation of topsoil. *Biogeochemistry* 123, 83–98. doi: 10.1007/s10533-014-0054-3.

Brice, J.C., (1964). Channel Patterns and Terraces of the Loup Rivers in Nebraska. In: U.S. Geological Survey Professional Paper 422-D. Washington, D.C. doi: 10.3133/PP422D. https://doi.org/10.3133/PP422D

Brice, J. C., (1966). Erosion and deposition in the loess-mantled Great Plains, Medicine Creek drainage basin, Nebraska: U.S. Geological Survey Professional Paper 352-H, p. 255-339. doi: 10.3133/PP352H

Browne, B.A., N.M. Guldan (2005). Understanding Long-Term Baseflow Water Quality Trends Using a Synoptic Survey of the Ground Water–Surface Water Interface, Central Wisconsin. *J. Environ. Qual*., 34: 825-835. doi: 10.2134/jeq2004.0134.

Cartwright, I., (2010). Using groundwater geochemistry and environmental isotopes to assess the correction of ^{14}C ages in a silicate-dominated aquifer system*, Journal of Hydrology, 382*(1), 174-187, doi: https://doi.org/10.1016/j.jhydrol.2009.12.032.

Cartwright, I., M. Currell, D. Cendón, K. Meredith (2020). A review of the use of radiocarbon to estimate groundwater residence times in semi-arid and arid areas. *Journal of Hydrology, 580*, 124247. doi: 10.1016/j.jhydrol.2019.124247.

Cerling, T. E., D. K. Solomon, J. Quade, J. R. Bowman (1991). On the isotopic composition of carbon in soil carbon dioxide, *Geochimica et Cosmochimica* Acta, 55(11), 3403-3405, doi: 10.1016/0016-7037(91)90498-T.

Cerling, T., J. Quade, Y. Wang (1989). Carbon isotopes in soils and palaeosols as ecology and palaeoecology indicators*. Nature* 341, 138–139. doi: 10.1038/341138a0.

Chen, X., X Chen (2004). Simulating the effects of reduced precipitation on ground water and streamflow in the Nebraska sand hills. *Journal of The American Water Resources Association, 40*, 419-430. doi: https://doi.org/10.1111/j.1752-1688.2004.tb01040.x

Chen, X., Q. Hu (2004). Groundwater influences on soil moisture and surface evaporation. *Journal of Hydrology, 297*, 285-300. doi: 10.1016/j.jhydrol.2004.04.019.

Chen, Y., Polach, H., (1986). Validity of 14C Ages of Carbonates in Sediments: Radiocarbon, v. 28, no. 2A, p. 464–472, doi: 10.1017/s0033822200007608.

Cherry M, T. Gilmore, A. Mittelstet, D. Gastmans, V. Santos, J.B. Gates (2020). Recharge seasonality based on stable isotopes: Nongrowing season bias altered by irrigation in Nebraska. Hydrological Processes. 2020;34:1575–1586. https://doi.org/10.1002/hyp.13683.

Clark, I.D., P. Fritz (1997). Environmental Isotopes in Hydrogeology. CRC Press.

Craig, H. (1953). The geochemistry of the stable carbon isotopes*, Geochimica et Cosmochimica Acta, 3*(2), 53-92, doi: 10.1016/0016-7037(53)90001-5.

Davidson, G. (1995). The stable isotopic composition and measurement of carbon in soil CO2. *Geochimica et Cosmochimica Acta, 59*, 2485-2489. doi: 10.1016/0016-7037(95)00143-3.

Deutz, P., I. P. Montañez, H. C. Monger, J. Morrison (2001). Morphology and isotope heterogeneity of Late Quaternary pedogenic carbonates: Implications for paleosol carbonates as paleoenvironmental proxies *Palaeogeography, Palaeoclimatology, Palaeoecology,166*(3), 293-317, doi: https://doi.org/10.1016/S0031-0182(00)00214-5.

Deutz P., I. P. Montañez, H.C. Monger (2002). Morphology and Stable and Radiogenic Isotope Composition of Pedogenic Carbonates in Late Quaternary Relict Soils, New Mexico, U.S.A.: An Integrated Record of Pedogenic Overprinting. *Journal of Sedimentary Research*; 72 (6): 809–822. doi: https://doi.org/10.1306/040102720809.

Dunne, T. (1990). Hydrology, mechanics, and geomorphic implications of erosion by subsurface flow. Groundwater Geomorphology; The Role of Subsurface Water in Earth-Surface Processes and Landforms, C. G. Higgins, D.R. Coates. doi: 10.1130/SPE252-P1

Fetter, C.W. (2018). Applied Hydrogeology: Fourth Edition. N.p.: Waveland Press, 2018.Fetter, C.W. (2001). Applied Hydrogeology. 4th Edition, Prentice Hall, Upper Saddle River, 2, 8. ISBN: 9781478637448

Fontes, J.-Ch. (1983). Dating of groundwater. Guidebook on Nuclear Techniques in Hydrology, 1983. IAEA, Vienna.

Fontes, J.-Ch. (1992). Chemical and isotopic constraints on ^{14}C dating of groundwater. In: Taylor, R.E., Long, A., Kra, R.S. (Eds.), Radiocarbon dating After Four Decades: An Interdisciplinary Perspective. Springer-Verlag, New York, pp. 242–261.

Fontes, J.-Ch., J. Garnier (1979). Determination of the initial ^{14}C activity of the total dissolved carbon: A review of the existing models and a new approach, *Water Resources Research*, 15(2), 399-413, doi: 10.1029/WR015i002p00399.

Fox, D.L., P.L. Koch (2003). Tertiary history of C4 biomass in the Great Plains, USA. *Geology*, 31, 809-812. doi: 10.1130/G19580.1.

Fox, D.L., P.L. Koch (2004). Carbon and oxygen isotopic variability in Neogene paleosol carbonates: constraints on the evolution of the C4-grasslands of the Great Plains, USA, *Palaeogeography, Palaeoclimatology, Palaeoecology*, 207(3), 305-329, doi: 10.1016/j.palaeo.2003.09.030.

Gardner, R. L., R. Diffendal, D.F. Williams (1992). Stable isotope composition of calcareous paleosols and ground-water cements from the Ogallala Group (Neogene), western Nebraska, *Contributions to Geology*, University of Wyoming, v. 29, no. 2. p. 97-109. 3 figs.

Gardner, P. M., Nelson, N. C., Heilweil, V. M., Solder, J. E., & Solomon, D. K. (2020). Rethinking a groundwater flow system using a multiple-tracer geochemical approach: A case study in Moab-Spanish Valley, Utah. *Journal of Hydrology*, *590*, 125512. doi: 10.1016/j.jhydrol.2020.125512

Geyh, MA. (2000). An overview of ^{14}C analysis in the study of groundwater. *Radiocarbon* 42(1):99–114. doi: 10.1017/s0033822200053078.

Gilmore, T.E., V. Zlotnik, M. Johnson (2019). Recognition of Regional Water Table Patterns for Estimating Recharge Rates in Shallow Aquifers. *Groundwater*, 57: 443 454. doi: 10.1111/gwat.12808.

Gilmore, T. E., D. P. Genereux, D. K. Solomon, J. E. Solder (2016). Groundwater transit time distribution and mean from streambed sampling in an agricultural coastal plain watershed, North Carolina, USA, *Water Resources Research*, 52(3), 2025–2044, doi: 10.1002/2015WR017600.

Gospodinova, K., A.P. Mcnichol, A. Gagnon, S.R. Shah Walter (2016). Rapid extraction of dissolved inorganic carbon from seawater and groundwater samples for radiocarbon dating. *Limnology and Oceanography: Methods* 14, 24–30. doi: 10.1002/lom3.10066.

Gosselin, D.C., S. Sibray, J. Ayers (1994). Geochemistry of K-rich alkaline lakes, Western Sandhills, Nebraska, USA: Geochimica et Cosmochimica Acta, v. 58, no. 5, p. 1403–1418, doi: 10.1016/0016-7037(94)90545-2.

Gosselin, D.C., (1997). Major-ion chemistry of compositionally diverse lakes, Western Nebraska, U.S.A.: implications for paleoclimatic interpretations: Journal of Paleolimnology, v. 17, no. 1, p. 33–49, doi: 10.1023/a:1007908909148.

Gosselin, D.C., S. Drda, F.E. Harvey, J. Goeke (1999). Hydrologic Setting of Two Interdunal Valleys in the Central Sand Hills of Nebraska*: Groundwater*, v. 37, no. 6, p. 924–933, doi: 10.1111/j.1745-6584.1999.tb01192.x.

Gosselin, D., S. Venkataramana, F.E. Harvey, J. Goeke (2006). "Hydrological Effects and Groundwater Fluctuations in Interdunal Environments in the Nebraska Sandhills". *Great Plains Research: A Journal of Natural and Social Sciences.* Paper 799. http://digitalcommons.unl.edu/greatplainsresearch/799.

Guhman, A.I., 1990, The role of groundwater sapping in gully formation along the Dismal River, Hooker and Thomas counties, Nebraska [M.S. thesis]: Lincoln, University of Nebraska, 61 p.

Guhman, A.I., & D.T. Pederson (1992). Boiling sand springs, Dismal River, Nebraska: Agents for formation of vertical cylindrical structures and geomorphic change. *Geology, 20*, 8-10. doi: 10.1130/0091-7613(1992)020<0008:BSSDRN>2.3.CO;2.

Haitjema, H.M., 1995, On the residence time distribution in idealized groundwatersheds: Journal of Hydrology, v. 172, no. 1-4, p. 127–146, doi: 10.1016/0022-1694(95)02732-5.

Hanson, P., N. Edwards, C. Garten (2000). Separating root and soil microbial contributions to soil respiration: A review of methods and observations. *Biogeochemistry* 48**,** 115–146. doi: 10.1023/A:1006244819642.

Han, L.F., L.N. Plummer, P. Aggarwal (2012). A graphical method to evaluate predominant geochemical processes occurring in groundwater systems for radiocarbon dating. *Chemical Geology.* 318–319, 88–112. doi: 10.1016/j.chemgeo.2012.05.004.

Han, L., L. N. Plummer (2013). Revision of Fontes & Garnier's model for the initial ^{14}C content of dissolved inorganic carbon used in groundwater dating, Chemical Geology, 351, 105-114, doi: 10.1016/j.chemgeo.2013.05.011.

Han, L.F., L.N. Plummer (2016). A review of single-sample-based models and other approaches for radiocarbon dating of dissolved inorganic carbon in groundwater, *Earth-Science Reviews*, Volume 152, 2016,Pages 119-142, ISSN 0012-8252, doi: 10.1016/j.earscirev.2015.11.004.

Han, L.F., L.I., Wassenaar (2021). Principles and uncertainties of ^{14}C age estimations for groundwater transport and resource evaluation, Isotopes in Environmental and Health Studies, 57:2, 111-141, DOI: 10.1080/10256016.2020.1857378

Harvey, F.E., J.B. Swinehart, T.M. Kurtz (2007). Ground water sustenance of Nebraska's unique sand hills peatland fen ecosystems. *Ground Water* 45:218–234. doi: 10.1111/j.1745-6584.2006.00278.x.

Hobza, C.M., P.A. Bedrosian, B.R. Bloss (2012). Hydrostratigraphic interpretation of test-hole and surface geophysical data, Elkhorn and Loup River Basins, Nebraska, 2008 to 2011: U.S. Geological Survey Open-File Report 2012–1227, 95 p. doi: 10.3133/ofr20121227.

Hobza, C.M., A.R. Schepers (2018). Groundwater discharge characteristics for selected streams within the Loup River Basin, Nebraska, 2014–16: U.S. Geological Survey Scientific Investigations Report 2018–5093, 50 p., doi: 10.3133/sir20185093.

Humphrey, E., D. K. Solomon, T. E. Gilmore, A. R. Mittelstet, V. A. Zlotnik, D. P. Genereux, C. R. Jensen, (2020). Using empirical transit time distributions to forecast stream water tracer concentration. In *AGU Fall Meeting Abstracts* (Vol. 2020, pp. H138-0013). https://agu.confex.com/agu/fm20/meetingapp. cgi/Paper/666576

Jacobs, K.C., Fritz, S.C., and Swinehart, J.B., 2007, Lacustrine evidence for moisture changes in the Nebraska Sand Hills during Marine Isotope Stage 3: Quaternary Research, v. 67, no. 2, p. 246–254, doi: 10.1016/j.yqres.2006.12.001.

Jensen, C.R. (2020). Estimating Groundwater Age in the Nebraska Sand Hills from SF_6 in Stream Water. [M.S. thesis]: North Carolina State University, 86 p. URI: https://www.lib.ncsu.edu/resolver/1840.20/38296.

Jost, W. (1960) *Diffusion in Solids, Liquids, and Gases***.** 3d ed. Academic Press.

Ingerson, E., F.J. Pearson Jr. (1964). Estimation of age and rate of motion of groundwater by the 14C method. *Recent Researches in the Fields of Hydrosphere, Atmosphere and Nuclear Chemistry*, pp. 263–283.

Kelly, E. F., R. G. Amundson, B. D. Marino, M. J. Deniro (1991). Stable Carbon Isotopic Composition of Carbonate in Holocene Grassland Soils, *Soil Sci. Soc. Am. J*., 55(6), 1651-1658, doi: 10.2136/sssaj1991.03615995005500060025x.

Kennedy, C. D., D. P. Genereux (2007). ^{14}C Groundwater Age and the Importance of Chemical Fluxes Across Aquifer Boundaries in Confined Cretaceous Aquifers of North Carolina, USA. *Radiocarbon, 49*(3), 1181-1203. doi: 10.1017/S0033822200043101.

Kennedy, C. D., D. P. Genereux, D. R. Corbett, H. Mitasova (2009). Relationships among groundwater age, denitrification, and the coupled groundwater and nitrogen fluxes through a streambed, Water Resour. Res., 45, W09402, doi: 10.1029/2008WR007400.

Kirchner, J.W., X. Feng, C Neal, C., (2000). Fractal stream chemistry and its implications for contaminant transport in catchments: Nature, v. 403, no. 6769, p. 524–527, doi: 10.1038/35000537.

Layzell, A.L., R.D. Mandel (2020). Late Quaternary landscape evolution and bioclimatic change in the central Great Plains, USA: GSA Bulletin, doi: 10.1130/B35462.1.

Lipps WC, Baxter TE, Braun-Howland E. (2018a). Standard Methods Committee of the American Public Health Association, American Water Works Association, and Water Environment Federation, 3111 metals by flame atomic absorption spectrometry In: Standard Methods For the Examination of Water and WastewaterWashington DC: APHA Press. doi: 10.2105/SMWW.2882.043

Lipps WC, Baxter TE, Braun-Howland E. (2018b). Standard Methods Committee of the American Public Health Association, American Water Works Association, and Water Environment Federation. 2320 alkalinity In: Standard Methods For the Examination of Water and Wastewater. Washington DC: APHA Press. doi: 10.2105/SMWW.2882.023

Loope, D.B., J. Swinehart (2000). Thinking Like a Dune Field: Geologic History in the Nebraska Sand Hills. Great Plains Research: A Journal of Natural and Social Sciences. 486. https://digitalcommons.unl.edu/greatplainsresearch/486.

Mason, J.A., J. B. Swinehart, D. B. Loope (2020). The Nebraska Sand Hills. In: Lancaster N., Hesp P. (eds) Inland Dunes of North America. Dunes of the World. Springer, Cham. doi: 10.1007/978-3-030-40498-7_5.

Maloszewski, P., Zuber, A. (1996). Lumped parameter models for the interpretation of environmental tracer data. In: Manual on Mathematical Models in Isotope Hydrogeology. IAEA (International Atomic Energy Agency), Vienna, pp. 9-58.

May, D.W. (1992). Late Holocene valley-bottom aggradation and erosion in the South Loup River Valley, Nebraska. *Physical Geography* 13, 115e132. doi: 10.1080/02723646.1992.10642448.

May, D.W. (2003). Properties of a 5500-year old flood-plain in the Loup River Basin, Nebraska *Geomorphology*, 56, pp. 243-254. https://doi.org/10.1016/S0169-555X(03)00154-5.

May, D. W. S. R. Holen (2014). Early Holocene alluvial stratigraphy, chronology, and Paleoindian/Early Archaic geoarchaeology in the Loup River Basin, Nebraska, U.S.A*., Quaternary International, 342*, 73-90, doi: https://doi.org/10.1016/j.quaint.2013.12.034.

May, D.W., J.B. Swinehart, D. Loope, V. Souders (1995). Late Quaternary fluvial and eolian sediments: Loup River Basin and the Nebraska Sand Hills. In: Diffendal Jr, R.F., Flowerday, C.A. (Eds.), Geologic Field Trips in Nebraska and Adjacent Parts of Kansas and South Dakota: Parts of the 29th Annual Meetings of the North-Central and South-Central Sections, Geological Society of America.

Mazor, E., R. Nativ (1992). Hydraulic calculation of groundwater flow velocity and age: examination of the basic premises. Journal of Hydrology 138, 211–222.. doi:10.1016/0022-1694(92)90165-r

Mccallum, J.L., S. Dogramaci, P.G. Cook, E. Banks, Purtschert, R., Irvine, M., Simmons, C.T., and Burk, L., 2018, Stochastic correction of carbon-14 activities: A Bayesian approach with argon-39 validation: Journal of Hydrology, v. 566, p. 396–405, doi: 10.1016/j.jhydrol.2018.08.047.

McGuire, K. J., & McDonnell, J. J. (2006). A review and evaluation of catchment transit time modeling. *Journal of Hydrology*, *330*(3-4), 543-563. doi: 10.1016/j.jhydrol.2006.04.020

McMahon, P.B., J.K. Böhlke, C.P. Carney (2007). Vertical gradients in water chemistry and age in the northern High Plains aquifer, Nebraska, 2003: U.S. Geological Survey Scientific Investigations Report 2006–5294, 58 p. doi: 10.3133/sir20065294.

McMahon, P.B., L.N. Plummer, J.K. Böhlke, S.D. Shapiro, S.R. Hinkle (2011). A comparison of recharge rates in aquifers of the United States based on groundwater-age data. *Hydrogeology Journal* **19,** 779 . https://doi.org/10.1007/s10040-011-0722-5

Miao, X.D., J. A. Mason, W. C. Johnson (2007a). High-resolution proxy record of Holocene climate from a loess section in Southwestern Nebraska, USA. *Palaeogeography, Palaeoclimatology, Palaeoecology* 245: 368–381. doi: 10.1016/j.palaeo.2006.09.004.

Miao, X.D., J. A. Mason, J. B. Swinehart, D. B. Loope, P. R. Hanson, R. J. Goble, X. Liu (2007b). A 10,000 year record of dune activity, dust storms, and severe drought in the central Great Plains. *Geology* 35:119–122. doi: 10.1130/G23133A.1.

Modica, E., Reilly, T.E. and Pollock, D.W. (1997). Patterns and Age Distribution of Ground-Water Flow to Streams. Groundwater, 35: 523-537. https://doi.org/10.1111/j.1745-6584.1997.tb00113.x

Modica, E., H.T. Buxton, L.N. Plummer (1998). Evaluating the source and residence times of groundwater seepage to streams, New Jersey Coastal Plain. *Water Resources Research, 34*, 2797-2810. doi: 10.1029/98WR02472.

Mook, W.G. (1972). On the reconstruction of the initial ^{14}C content of groundwater from the chemical and isotopic composition. *Proceedings of Eighth International Conference on Radiocarbon Dating, Royal Society of New Zealand*, Wellington. 1, pp. 342–352.

Mook, W.G. (1976). The dissolution-exchange model for dating groundwater with ^{14}C. Interpretation of Environmental Isotope and Hydrochemical Data in Groundwater Hydrology 1976. IAEA, Vienna, pp. 213–225.

Mook, W. G. (1980). Chapter 2 – Carbon-14 in Hydrogeological Studies, in *The Terrestrial Environment, A*, edited by P. FRITZ and J. Ch FONTES, pp. 49-74, Elsevier, Amsterdam. doi: https://doi.org/10.1016/B978-0-444-41780-0.50008-0.

Mook, W., G.J. van der Plicht (1999). Reporting ^{14}C Activities and Concentrations, *Radiocarbon*, 41(3), 227-239, doi: 10.1017/S0033822200057106.

Morel, F., J. G. Hering (1993). *Principles and Applications of Aquatic Chemistry*, New York : Wiley, 1993], New York.

Muhs, D. R. (2017). Evaluation of simple geochemical indicators of aeolian sand provenance: Late Quaternary dune fields of North America revisited, *Quaternary Science Reviews*, 171, 260-296, doi: 10.1016/j.quascirev.2017.07.007.

Nicholson, B.J., J.B. Swinehart (2005). Evidence of Holocene climate change in a Nebraska Sandhills wetland. *Great Plains Research* 15:45–67.

Noseck, U., K. Rozanski, M. Dulinski, V. Havlová, O. Sracek, T. Brasser, M. Hercik,G. Buckau (2009). Carbon chemistry and groundwater dynamics at natural analogue site Ruprechtov, Czech Republic: Insights from environmental isotopes: Applied Geochemistry, v. 24, no. 9, p. 1765–1776, doi: 10.1016/j.apgeochem.2009.05.007.

Olsson I.U. (1970). The use of oxalic acid as a standard. In: Olsson IU, editor. *Radiocarbon Variations and Absolute Chronology*. Nobel Symposium, 12th Proceedings. New York: John Wiley and Sons. p 17.

Parkhurst, D.L., S.R. Charlton (2008). NetpathXL—An Excel® interface to the program NETPATH: U.S. Geological Survey Techniques and Methods 6-A26, doi: 10.3133/tm6A26.

Pearson Jr., F.J., M.S. Bedinger, B.F. Jones (1972). Carbon-14 ages of water from the Arkansas Hot Springs. Proceedings of Eighth International Conference on Radiocarbon Dating. Royal Society of New Zealand, Wellington, pp. 330–341.

Pearson Jr., F.J., B.B. Hanshaw Jr. (1970). Sources of dissolved carbonate species in groundwater and their effects on carbon-14 dating. Isotope Hydrology 1970. IAEA, Vienna, pp. 271–286.

Pearson Jr., F.J., W.W. Swarzenki (1974). ^{14}C evidence for the origin of arid region groundwater, Northeastern Province, Kenya. Isotope Techniques in Groundwater Hydrology 1974. IAEA, Vienna, pp. 95–108.

Pearson Jr., F.J., D.E. White (1967). Carbon-14 ages and flow rates of water in Carrizo Sand, Atascosa County, Texas. Water Resour. Res. 3, 251–261.

Pfaff, J. D. (1993). Method 300.0 Determination of inorganic anions by ion chromatography. *US Environmental Protection Agency, Office of Research and Development, Environmental Monitoring Systems Laboratory*, *28*.

Plummer, L.N., L. Bexfield, S. Anderholm, W. Sanford, E. Busenberg, (2004). Hydrochemical tracers in the middle Rio Grande Basin, USA: 1. Conceptualization of groundwater flow: Hydrogeology Journal, v. 12, no. 4, doi: 10.1007/s10040-004-0324-6.

Plummer, L.N., J.F. Busby, R.W. Lee, and B.B. Hanshaw (1990). Geochemical modeling of the Madison aquifer in parts of Montana, Wyoming, and South Dakota: Water Resources Research, v. 26, p. 1981-2014. doi: https://doi.org/10.1029/WR026i009p01981.

Plummer, L. N., E. Busenberg (1982). The solubilities of calcite, aragonite and vaterite in CO2-H2O solutions between 0 and 90°C, and an evaluation of the aqueous model for the system CaCO3-CO2-H2O*, Geochim. Cosmochim. Acta, 46*(6), 1011-1040, doi: https://doi.org/10.1016/0016-7037(82)90056-4.

Plummer, L.N., Parkhurst, D.L., and Thorstenson, B.C. (1983). Development of reaction models for groundwater systems: Geochimica et Cosmochimica Acta, v. 47, p. 665-685.

Plummer, L.N., Prestemon E.C., D.L. Parkhurst (1994). An interactive code (NETPATH) for modeling net geochemical reactions along a flow path, version 2.0. US Geological Survey, *Water Resources Investigations Report* 94-4169. 130 p. doi: 10.3133/wri944169.

Plummer, L.N., P.D. Glynn (2013). Radiocarbon dating in groundwater systems: Chapter 4. In: INTERNATIONAL ATOMIC ENERGY AGENCY, Isotope Methods for Dating Old Groundwater, IAEA, Vienna (2013). URI: https://pubs.er.usgs.gov/publication/70046479.

Salem, O., J.H. Visser, M. Dray, R. Gonfiantini (1980). Groundwater flow patterns in the western Lybian Arab Jamahiriaya. Arid-Zone Hydrology: Investigations with Isotope Techniques 1980. IAEA, Vienna, pp. 165–179.

Schacht, W.H., J.D. Volesky, B. Bauer, A.J. Smart, E.M. Mousel (2000). Plant community patterns on upland prairie in the eastern Nebraska Sandhills. The Prairie Naturalist, 32 (2000), pp. 43-58. https://digitalcommons.unl.edu/agronomyfacpub/339?utm_source=digitalcommons.unl.edu%2Fagronomyfacpub%2F339&utm_medium=PDF&utm_campaign=PDFCoverPages.

Shah Walter, S.R., A.R. Gagnon, M.L. Roberts, A.P. Mcnichol, M.C.L. Gaylord, E. Klein (2015). Ultra-Small Graphitization Reactors for Ultra-Microscale 14C Analysis at the National Ocean Sciences Accelerator Mass Spectrometry (NOSAMS) Facility. *Radiocarbon* 57, 109–122. doi: 10.2458/azu_rc.57.18118.

Solder, J., B.C. Jurgens (2020). Evaluation of soil zone processes and a novel radiocarbon correction approach for groundwater with mixed sources. *Journal of Hydrology, 588*, 124766. doi: 10.1016/j.jhydrol.2020.124766.

Solomon, D.K., E. Humphrey, T.E. Gilmore, D.P. Genereux, V. Zlotnik (2020). An Automated Seepage Meter for Streams and Lakes. Water Resources Research 56, e2019WR026983. doi: 10.1029/2019wr026983.

Sophocleous, M. (2010). Review: groundwater management practices, challenges, and innovations in the High Plains aquifer, USA—lessons and recommended actions. *Hydrogeology Journal* 18**,** 559–575. doi: 10.1007/s10040-009-0540-1.

Steuter, A. A., B. Jasch, J. Ihnen, L. L. Tieszen (1990). Woodland/Grassland Boundary Changes in the Middle Niobrara Valley of Nebraska Identified by ^{13}C Values of Soil Organic Matter, *The American Midland Naturalist*, 124(2), 301-308, doi: 10.2307/2426179.

Stokes, S., J.B. Swinehart (1997). Middle- and late-Holocene dune reactivation in the Nebraska Sand Hills, USA. *The Holocene,* 7:263–272. doi: 10.1177/095968369700700302.

Summerside, S., M. Ponte, V.H. Dreeszen, S.L. Hartung, M.J. Khisty, J. Szilagyi (2001). Update and Revision of Regional 1x2 Water-Table Configuration Maps for the State of Nebraska, 9. Lincoln, Nebraska: Conservation and Survey Division – Institute of Agriculture and Natural Resources, University of Nebraska, Lincoln.

Szilagyi, J.J. Jozsa (2013). MODIS-Aided Statewide Net Groundwater-Recharge Estimation in Nebraska. *Groundwater*, 51: 735-744. doi: 10.1111/j.1745-6584.2012.01019.x

Tamers, M. A. (1967). Radiocarbon ages of groundwater in an arid zone unconfined aquifer, in *Isotope Techniques in the Hydrologic Cycle*, pp. 143-152, American Geophysical Union, Washington, D. C.

Tamers, M.A. (1975). Validity of radiocarbon dates on ground water*: Geophysical Surveys*, v. 2, no. 2, p. 217–239, doi: 10.1007/bf01447909.

Tecsa, V, J. A. Mason, W. C. Johnson (2020). Latest Pleistocene to Holocene loess in the central Great Plains: Optically stimulated luminescence dating and multi-proxy analysis of the enders loess section (Nebraska, USA). *Quaternary Science Reviews* 229:106130. doi: 10.1016/j.quascirev.2019.106130.

Winter, T.C. (1986), Effect of ground-water recharge on configuration of the water table beneath sand dunes and on seepage in lakes in the sandhills of Nebraska, U.S.A.: Journal of Hydrology, v. 86, no. 3-4, p. 221–237, doi: 10.1016/0022-1694(86)90166-6.

Winter, T.C., Rosenberry, D.O., and Labaugh, J.W. (2003). Where Does the Ground Water in Small Watersheds Come From?: Groundwater, v. 41, no. 7, p. 989–1000, doi: 10.1111/j.1745-6584.2003.tb02440.x.

Zlotnik, V.A., J.B. Ong, J.D. Lenters, J. Schmieder, S.C. Fritz (2012). Quantification of salt dust pathways from a groundwater-fed lake: Implications for solute budgets and dust emission rates: Journal of Geophysical Research, v. 117, no. F2, p. n/a–n/a, doi: 10.1029/2011jf002107.